



Università degli Studi di Trento  
Scuola di Dottorato in Fisica  
XXV Ciclo

# **Silicon nanocrystals downshifting for photovoltaic applications.**

PhD Candidate: **Fabrizio Sgrignuoli**

Supervisor: **Prof. Lorenzo Pavesi**

*Anno Accademico 2011/2012*

*To the memory of my grandmothers...*

*“Things on a very small scale (like electrons) behave like nothing that you have any direct experience about. They do not behave like waves, they do not behave like particles, they do not behave like clouds, or billiard balls, or weights on springs, or like anything that you have ever seen.”*

**Richard Feynman**



---

# Contents

List of Symbols	v
Introduction	vii
<b>1 Third Generation Photovoltaics: state of the art.</b>	<b>1</b>
1.1 Limits of Photovoltaic Devices . . . . .	1
1.2 Light-matter interaction at the nanometer scale. . . . .	5
1.3 Multiple Exciton Generation: MEG. . . . .	8
1.3.1 MEG in Si-QDs. . . . .	12
1.4 Solar Spectrum Modification. . . . .	16
1.4.1 Down and Up Conversion . . . . .	18
1.4.2 Luminescence Downshifting . . . . .	20
1.5 Material under investigation: bulk and nanostructured silicon. . . . .	22
1.5.1 Si-NCs as LDS material. . . . .	25
1.6 Conclusions. . . . .	26
<b>2 Silicon Nanocrystals for downshifting applications.</b>	<b>29</b>
2.1 Preliminary study on the LDS effect based on Si-NCs . . . . .	30
2.1.1 Photoluminescence downshifted solar cell . . . . .	30
2.1.2 Results, discussion, and future perspectives. . . . .	31
2.2 LDS effect and optical properties . . . . .	37
2.2.1 Transfer matrix based simulations: optical losses optimization . . . . .	37
2.2.2 Luminescent quantum yield . . . . .	41
2.2.3 Optimization of the double layer stack . . . . .	49
2.3 Lima Project . . . . .	57
2.3.1 Final integrated IBC device. . . . .	58

---

2.3.2	Optimization . . . . .	60
2.3.3	Results of integrated devices with Si-QDs as active layer . . .	63
2.4	Conclusions . . . . .	70
<b>3</b>	<b>Detection of the LDS effect in Si-NCs</b>	<b>73</b>
3.1	Method Description . . . . .	74
3.1.1	Si-NCs On Quartz substrate . . . . .	77
3.1.2	Colloidal Si-NCs in Glycerol solution . . . . .	80
3.2	Experimental Results . . . . .	83
3.2.1	SRO on Quartz: Experimental Results . . . . .	83
3.2.2	Colloidal Si-NCs: Experimental Results . . . . .	86
3.3	Conclusions . . . . .	89
<b>4</b>	<b>LDOS Modification: directionality of the emitted light</b>	<b>91</b>
4.1	Classical Oscillating Dipole . . . . .	92
4.2	Spontaneous Emission . . . . .	95
4.2.1	Spontaneous Emission: Dyadic Green's functions . . . . .	96
4.3	LDOS modification . . . . .	99
4.3.1	Radiation pattern of interfacial vertical dipole . . . . .	99
4.4	Quantum dots emission: validity of the dipole approximation. . . . .	106
4.4.1	Si-NCs as oscillating electric dipoles. . . . .	109
4.4.2	Simulated Structures . . . . .	110
4.4.3	Simulation Results. . . . .	112
4.5	Conclusions . . . . .	117
	<b>Conclusions and future perspectives</b>	<b>119</b>
	<b>Bibliography</b>	<b>121</b>
	<b>Acknowledgements</b>	<b>136</b>

---

## List of Symbols

---

<b>PV</b>	Photovoltaic
<b>REF</b> or <b>ref</b>	Reference solar cell
<b>PDS</b>	Photoluminescence <b>D</b> own-shifted Solar cell
<b>IBC</b>	Interdigitated <b>B</b> ack <b>C</b> ontact silicon solar cell
<b>ARC</b>	<b>A</b> nti <b>R</b> eflection <b>C</b> oating
<b>FSF</b>	<b>F</b> ront <b>S</b> urface <b>F</b> ield
<b>BSF</b>	<b>B</b> ack <b>S</b> urface <b>F</b> ield
<b>IQE</b>	<b>I</b> nternal <b>Q</b> uantum <b>E</b> fficiency
<b>PR</b>	<b>P</b> hotoresponsivity
<i>SR</i>	<b>S</b> pectral <b>R</b> esponsivity
$J_{sc}$	<b>S</b> hort <b>C</b> ircuit current density
$V_{oc}$	<b>O</b> pen <b>C</b> ircuit voltage
<b>FF</b>	<b>F</b> ill <b>F</b> actor
<b>eta</b> or $\eta$	<b>E</b> fficiency

---

<b>UP</b>	<b>U</b> p conversion
<b>DC</b>	<b>D</b> own <b>C</b> onversion
<b>MEG</b>	<b>M</b> ultiple <b>E</b> xciton <b>G</b> eneration
<b>SSQC</b>	<b>S</b> pace <b>S</b> eparated <b>Q</b> uantum <b>C</b> utting
<b>CDCT</b>	<b>C</b> oulomb <b>D</b> riving <b>C</b> harge <b>T</b> ransfer
<b>LDS</b>	<b>L</b> uminescence <b>D</b> ownshifting effect

---

<b>PECVD</b>	<b>P</b> lasma <b>E</b> nanced <b>C</b> hemical <b>V</b> apour <b>D</b> eposition
<b>SRO</b>	<b>S</b> ilicon <b>R</b> ich <b>O</b> xide
<b>SRO NA</b>	<b>S</b> ilicon <b>R</b> ich <b>O</b> xide <b>N</b> ot <b>A</b> nnealed

---

<b>QDs</b>	<b>Quantum Dots</b>
<b>Si-QDs</b>	<b>Silicon Quantum Dots</b>
<b>Si-NCs</b>	<b>Silicon Nanocrystals</b>
<b>Si-Nps</b>	<b>Silicon Nanoparticles</b>
<b>QY</b>	<b>Quantum Yield</b>
<b>LDOS</b>	<b>Local Density of Optical States</b>
<b>PL</b>	<b>Photoluminescence</b>
<b>PLE</b>	<b>Photoluminescence Excitation</b>
<b>PL QY</b>	<b>Photoluminescence Quantum Yield</b>
<b>TA</b>	<b>Transient Absorption technique</b>

---

<b>RIML</b>	<b>Refractive Index Matching Liquid</b>
<b>WPF</b>	<b>Wave Pass Filter</b>
<b>SWPF</b>	<b>Short Wave Pass Filter</b>
<b>LWPF</b>	<b>Long Wave Pass Filter</b>

---

<b>PMT</b>	<b>Photomultiplier Tube</b>
<b>VASE</b>	<b>Variable Angle Spectroscopic Ellipsometer</b>
<b>Ar<sup>+</sup></b>	<b>Argon ion laser</b>
<b>Nd:YVO<sub>4</sub></b>	<b>Neodymium-doped Yttrium Orthovanade laser</b>

---

<b>FBK</b>	<b>Fondazione Bruno Kessler (Trento Italy)</b>
<b>AP&amp;P</b>	<b>Advanced Photonics &amp; Photovoltaics group (FBK-Trento)</b>
<b>ISC</b>	<b>Institute Solar Energy Research Center (Kostanz Germany)</b>
<b>NTC-UPVLC</b>	<b>Nanophotonics Technology Center Universidad Politécnica de Valencia</b>

---

# Introduction

Photovoltaic, the conversion of sunlight to electrical power, is dominated by single-junction devices, often made of silicon. Approximately, 85% of the PV market is based on crystalline silicon, including both large grain multicrystalline (multi cSi) and mono-crystalline (mono cSi) materials [1]. These solar modules based on silicon wafer have been called “first generation” photovoltaic technologies. The timeline of the energy conversion efficiency of these solar devices is reported in Fig.1 (blue lines). A second class of solar cells “2<sup>nd</sup> generation” attempts to reduce costs by using thin film semiconductors like amorphous silicon (a-Si), CdTe, Cu(In,Ga)Se<sub>2</sub> with about ~14% of the market share [1] and cell efficiency in the range 10%-20% depending on the system (green lines in Fig.1). Nowadays, the dominance of single-junction devices is challenged by the emergence of a new generation of photovoltaic cells, for example, based on nanocrystalline materials. Indeed, the problem of materials availability together with the too large cost of most of the photovoltaic technologies led to the so-called third generation photovoltaics. The aim of this new research field is to keep the ratio costs/Watt as low as possible and, at the same time, to increase the performance of solar devices. A series of different concepts and physical phenomena, based on the exploitation of light-matter interaction at the nanometer length-scale, are investigated to reach this purpose.

The main topics of this thesis are the characterization, the study and the development of interdigitated back contact silicon solar cells with silicon quantum dots (Si-QDs) as active material. These devices are developed within the european project LIMA (improve photovoltaic efficiency by applying novel effect at the limits of light to matter interaction) [3]. The use of Si-QDs as active layer produces a modification of the incident sunlight radiation due to the luminescence downshifting effect: high energy photons are absorbed while low energy photons are emitted. Before going into the details about this specific physical effect, it is necessary to

motivate the choice of silicon as preferred material and the reason to use it as active element in the form of nanoparticles for photovoltaic applications.

Bulk silicon is a semiconductor material of the group IV, with a good electrical, mechanical, and thermal stability. Over 90% of the Earth's crust is composed of silicate minerals, making silicon the second most abundant element after oxygen [4]. The actual photovoltaic market is ruled by silicon solar cell. It has an energy band gap of 1.12 eV at 300 K, which is optimal not only for standard single p-n junction cells, but also for the bottom layer in a 2-junction or even 3-junction tandem stack. A solar cell entirely based on silicon is advantageous in term of potential for large scale manufacturing and in long term availability of its constituents. Moreover, considering the cheap material manufacturability and the rise of very-large-scale-integration (VLSI), silicon plays a predominant role also in the microelectronics industry. Nowadays, silicon based technology is present in nearly every electronic product in the world. However, bulk silicon is a poor emitter due to its indirect

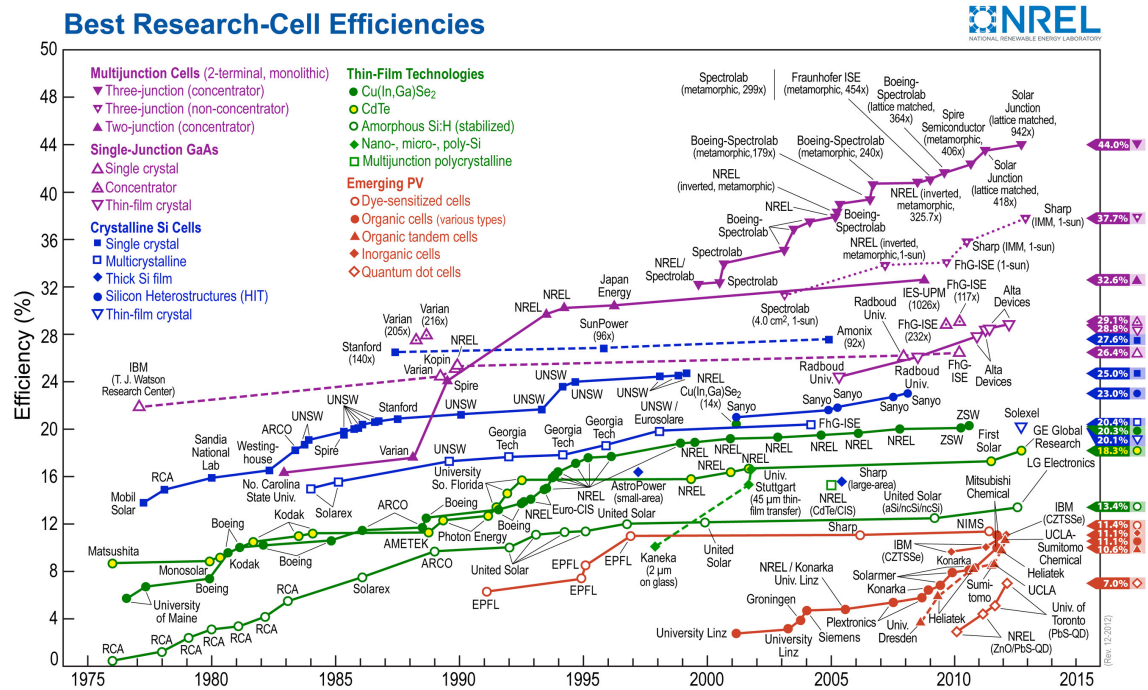


**Figure 1:** Reported timeline of solar cell energy conversion efficiency (from National Renewable Energy Laboratory (NREL) [2])

band gap. The probability for a radiative transition is very low, *i.e.* the photon emission produced by the radiative recombination of an electron-hole pair is a low probability process.

The discovery of visible emission from nanocrystalline [5] and porous silicon [6–8] in the early 1990s, opened a new scenario: the problems associated with the silicon band structure could be overcome in nanoscale crystallites, which are hosted in a widegap dielectric matrix. Electronic states become localized within silicon quantum dots (Si-QDs) resulting in a reduction of the electron mobility with respect to the bulk Si. Moreover, the momentum distribution spreads due to Heisenberg uncertainty principle. As a consequence, the momentum conservation relaxes, *i.e.* the optical transition rate increases. Therefore, quantum confined silicon, in the form of Si-QDs of diameter 5 nm or less, shows very different properties with respect to the bulk material. The reduction of the dimensions leads to the transformation of the band structure from a continuous to a discrete set of energy levels, producing new physical phenomena in the framework of light-matter interaction:

- the resonant interaction between photon and Si-QD can be tuned by a size change, *i.e.* controlling the particle size it is possible to shift its energy bandgap to the optimum energy gap ( $\sim 1.6$  eV) of a single junction solar cell;
- the relaxation of excited carrier, generated by photon absorption, is slowed down with respect to bulk silicon due to the widening of the distance between the energy states;
- after the absorption of one incident photon with energy greater than twice the Si-QDs energy gap, an electron-hole pair, called exciton, is created with an excess energy. This energy can be used to generate other excitons instead of having transformed in heat;
- radiative emissions originated from band-to-band recombination of quantum confined exciton is observed, *i.e.* Si-QDs display strong photoluminescence signal in the visible-red part of the spectrum.

All these new perspectives can be used to improve the performances of photovoltaic devices, reducing the typical losses, as heat, that characterize silicon standard solar cells.

The work presented in this thesis is inserted in this context: we investigated the properties of Si-QDs to improve solar cell performances. The silicon nanoparticles used in this thesis were produced by plasma enhanced chemical vapor deposition (PECVD) of a silicon rich oxide layer (SRO). After a high annealing treatment, the silicon nanoparticles precipitate in the SRO layer. The luminescence downshifting (LDS) effect was considered as the building block of our research activity. The LDS layer is used to transform one high-energy photon, for which the internal quantum efficiency (IQE)<sup>1</sup> is low, to a lower energy-photon, for which IQE is high, thereby increasing the short circuit current and, then, the solar cell efficiency.

In Chapter 1, an overview on the state of the art of third generation photovoltaics is presented. Different concepts, as multiple excitons generation, and solar spectrum modification, will be discussed as possible solutions to the energy conversion problem. In subsection 1.4.2 the concept of LDS effect is presented and discussed. In particular, the guidelines of our research will be defined. In addition to the potential efficiency enhancement, the introduction of a LDS layer, formed by silicon nanoparticles dispersed in a silicon dioxide matrix, can create additional interactions with the light resulting in extra loss mechanism. The main physical loss processes that can take place are:

- increased optical losses due to the introduction of an additional interface
- losses through the top or the edges of the new layer, as the emitted light could not be directed efficiently towards the silicon solar cell

Chapter 2 examines the problems related to the integration of a Si-QDs layer during the fabrication of photovoltaic devices. In section 2.1 a preliminary study based on front contact silicon solar cells characterized by different active layers is presented. This preliminary study revealed bad performance due to increased optical losses introduced by these new layers. As a consequence, an optimization code was developed. This optimization model is based on the transfer matrix method in combination with a phenomenological approach describing the Si-QDs photoluminescence. The results of this model are used within the european project LIMA in order to produce an optimal interdigitated back contact (IBC) solar cell including

---

<sup>1</sup>A cell parameter that expresses the efficiency with which photons generate carriers which produce a current.

Si-QDs as active material. Experimental studies, as well as optical and electrical simulations are presented to examine and to understand the obtained results. Moreover, an experimental determination of the quantum yield of Si-QDs, based on photoluminescence decay time measurements, is discussed.

Most of these results are presented also in:

- Z. Yuan, G. Pucker, A. Marconi, F. Sgrignuoli, A. Anopchenko, Y. Jestin, L. Ferrario, P. Bellutti, L. Pavesi, “ Silicon nanocrystals as a photoluminescence down shifter for solar cells”, *Solar Energy Materials & Solar Cells*, **95**, 4 (2011).
- F. Sgrignuoli, G. Paternoster, A. Marconi, P. Ingenhoven, A. Anopchenko, G. Pucker, L. Pavesi, “Modeling of silicon nanocrystals based down-shifter for enhanced silicon solar cell performance”, *Journal of Applied Physics*, **111**, 3 (2012).
- P. Ingenhoven, A. Anopchenko, A. Tengattini, D. Gandolfi, F. Sgrignuoli, G. Pucker, Y. Jestin, L. Pavesi, R. Balboni, “Quantum effects in silicon for photovoltaic applications”, *Physica Status Solidi (a)*, (2013).
- F. Sgrignuoli, Y. Jestin, E. Moser, P. Ingenhoven, G. Pucker, L. Pavesi, “ Silicon Nanocrystals for Downshifting Applications: A Preliminary Study”, *27th European Photovoltaic Solar Energy Conference and Exhibition*, on press (DOI: 10.4229/27thEUPVSEC2012-1BV.8.9) (2013).

Part of the results presented in this chapter were obtained thanks to the collaboration with different people. In the section 2.1 the front contact silicon solar cells, produced at the AP&P by Dr. G. Pucker and Dr. Y. Jestin, were measured by Dr. Z. Yuan, Dr. A. Anopchenko, and Dr. A. Marconi. In the subsection 2.2.2 the photoluminescence decay time experiments were carried out with the collaboration of Dr. A. Marconi and Dr. P. Ingenhoven while the samples were produced at the AP&P center. The results presented in section 2.3, on the fabrication and the electrical-optical characterization of IBC including Si-QDs, were obtained thanks to efforts of all the LIMA partners. The J-V measurements have been achieved at the ISC and NTC-UPVLC center. In particular, my contribution was focused on the modeling and the data analysis of the presented results.

In Chapter 3, an alternative method to apply a down-shifter layer on IBC solar cells is proposed. The aim of this study is to separate the silicon nanocrystals pro-

duction from the device manufacturing. The SRO layer is not deposited directly on the silicon solar cell, as in chapter 2, but on a quartz substrate. This active layer is used as cell cover glass resembling the situation of a PV module where a glass cover is applied to protect it from environmental influences. Different configurations are presented and analyzed changing the liquid in the cover/IBC spacing layer to “activate” the optical properties of the cover. Moreover, also colloidal Si-NCs dispersed in glycerol solution was used as “active” liquid to produce a possible improvement of the IBC performance.

In this study, the SRO layer were fabricated by Dr. Y.Jestin and Dr. G.Pucker at the AP&P center while the colloidal Si-NCs in glycerol solution were produced by Dr. E.Froner at the University of Trento. The presented experiments, as well as the simulations, were the topic of my research activity.

Chapter 4 proposes a simulation study based on the modification of the local optical density of states (LDOS). The aim of this analysis is to understand and to explain the experimental results of chapter 2 and 3. In particular, the possibility to control the spontaneous emission process, by placing emitters near a suitable environment, is described. The spontaneous emission is treated using the dipole approximation and the Dyadic Green’s function formalism. These concepts are exploited to create a connection between the classical and the quantum mechanics framework: LDOS is connected with the power radiated by an oscillating electric dipole to analyze its modification due to environment. After some considerations on the validity of the dipole approximation in the case of silicon nanoparticles, an array of one hundred electric dipoles is used to simulate the incoherent Si-QDs emission. This modeling is applied to different multilayered structures to explain the results of chapter 2 and 3 in term of Purcell’s effect.

Part of the work presented in Chapter 2, 3, and 4 is the content of the article

- F.Sgrignuoli, P. Inghoven, G.Pucker, E.Froner, V. D. Mihailetschi, G.Sánchez, L.Pavesi, “.”, *in preparation*

As conclusions, some future perspective and possibilities for this line of research are discussed.

---

# Chapter 1

## Third Generation Photovoltaics: state of the art.

In this first chapter, I will present the state of the art of Third generation photovoltaics.

At first, I will introduce the main loss mechanisms of a standard photovoltaic device underlining the necessity of novel concepts that guarantee a better exploitation of the incident sunlight radiation. Particularly appealing is the possibility of employing nano-structured semiconductors. Indeed, these innovative materials permit to take advantage of the quantum properties that characterize the light-matter interaction at nanometer scale. Different concepts, such as multiple exciton generation and solar spectrum modification, will be discussed as possible solutions to the energy conversion problem. Then, I will present the materials under study to understand the role of quantum mechanical effects that characterize the optical properties of silicon nanoparticles. In the last section of this chapter, I will describe the heart of my research activity represented by the luminescent downshifting effect and its possible application in the photovoltaic scenario.

### 1.1 Limits of Photovoltaic Devices

Conventional single-junction solar cells, such as those based on crystalline silicon (c-Si), routinely attain a high energy conversion efficiency of  $\sim 22\%$ , albeit with significant manufacturing cost associated with material purification, high temperature

processing steps, and strict parameters control. Nowadays, the record in the energy conversion efficiency for a c-Si solar cell is  $(25.0 \pm 0.5)\%$  under standard AM1.5G illumination [9].

As it is well known, the maximum thermodynamic efficiency for the conversion of solar irradiance into electrical free energy in the radiative limit<sup>1</sup> (assuming detailed balance, and thermal equilibrium between electrons and phonons) was calculated by Shockley Queisser in 1961 [10]. For a semiconductor with a bandgap of 1.1 eV, close to that of silicon, it results to be about 30%. This limit represents an ideal upper bound on the efficiency conversion. One of the major problems that limit the solar cell performances is the large range of wavelengths over which the energy conversion efficiency has to take place. Indeed, photons with energy below the semiconductor bandgap ( $E_G$ ) are not absorbed. Photon absorption coincides with the interband transition of an electron from the valence to the conduction band, and the simultaneous formation of a hole in the valence band. The binding energy of the electron-hole pairs is too low to produce excitons at room temperature. For example, the exciton binding energy in the bulk silicon is  $\sim 15$  meV. Photons with energy above  $E_G$  create charge carriers (electrons and holes) with a total excess kinetic energy equal to the difference between the photon energy and the semiconductor bandgap. This excess energy creates an effective temperature for the ensemble of photogenerated carriers that can be much higher than the lattice temperature; such carriers are called “hot” electrons and “hot” holes and their temperature, upon the photon absorption, can be as high as 3000 K [11]. The total excess energy in bulk semiconductors is shared to accommodate momentum conservation, such that the carriers with the lighter effective mass (typically electron) receive most of this energy [12]. Thus:

$$\Delta E_e = (h\nu - E_G)[1 + m_e^*/m_h^*]^{-1} \quad (1.1)$$

$$\Delta E_h = (h\nu - E_G) - \Delta E_e \quad (1.2)$$

where  $\Delta E_e$  ( $\Delta E_h$ ) is the energy difference between the conduction (valence) band and the initial energy of the photogenerated electron (hole) (see Fig.1.1 a). In conventional photovoltaic devices, these “hot” carriers quickly cool, within  $\sim 1$  ps [13], before all of their energy can be captured. In more details, “hot” charge carriers interact with the crystal lattice, primarily through LO-phonon emission,

---

<sup>1</sup>All the recombination mechanisms are radiative.

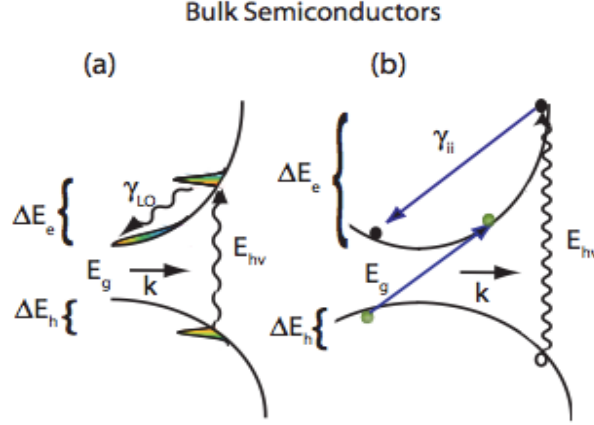


**Figure 1.1:** a) Photo-excited carrier dynamics in bulk semiconductors. An electron and hole population is formed with excess kinetic energy after the absorption of a high energetic photon. The electrons/holes thermalize and cool to form a fermi-Dirac distribution at the band gap on the timescale  $\sim 1$  ps. b) Electrons/holes with excess energy greater than  $E_G$  can generate additional carriers at the bandgap due to the impact ionization. The impact ionization in bulk semiconductors must satisfy both the energy and momentum conservation (from [14]).

**Table 1.1:** Various solar energy losses in single junction silicon (1.1eV energy bandgap) solar cell under AM1.5G illumination [14]. Photo-electron energy conversion is the Shockley Queisser limit.

Photo-electron energy conversion	32.9%
Unabsorbed energy losses	18.7%
Heat loss	46.8%
Other losses	1.6%

losing energy to the crystal lattice in the form of heat until the carrier distribution temperature matches the lattice temperature. As shown in Table1.1, heat loss is mainly responsible for lower efficiency in silicon solar cells.

Unabsorbed energy losses can be partially recovered by using the concept of tandem solar cells. These devices are characterized by different semiconductor materials of increasing bandgap that are placed on top of each others. In this way, spectrum splitting and photon selectivity are automatically achieved by the stacking arrangement [15]. Tandem solar cells show very high efficiency, but the huge cost of the growth techniques and of the used compounds mean that these devices are usually designed for use in niche market such as those for optical concentrator

systems operating at a few hundred suns.

In 1982 thermodynamic calculations [16] demonstrated that the same high conversion efficiency of a tandem stack of different bandgaps, can be obtained by utilizing the excess energy of the “hot” photogenerated carriers before their cooling to the lattice temperature. These devices, called “*hot carriers solar cell*” [12, 17, 18], can extract the excess energy following two methods:

- removing the “hot” carriers before the cooling obtaining a higher energy electron and thus getting a higher voltage output [17, 19]. To make this, the rate cooling of “hot” electrons must be lower than the rate of the carrier separation, transport, and collection at contacts.
- using the excess kinetic energy to produce additional electron-hole pairs resulting in a higher photo-current output. In bulk semiconductors, this mechanism is called impact ionization (I.I.), as shown in Fig.1.1 (b).

However, this last mechanism cannot contribute to an improved power conversion efficiency in present solar cells. Indeed, I.I. requires the conservation of both energy and momentum, like all scattering processes occurring in bulk semiconductors. These conservation requirements increase the photon energy threshold of the impact ionization above the simple  $2E_G$  [20]. Additionally, the rate of I.I. must compete with the rate of the energy relaxation by phonon emission through electron-phonon scattering. It has been shown that the rate of I.I. becomes competitive with phonon scattering rates only when the kinetic energy of the electron is many multiples of  $E_G$ : for silicon 3.6-4.4 times  $E_G$  [19].

An effective harvesting of UV and IR photons is a necessary condition to improve the efficiency of solar cells reducing the cost per watt of electricity produced. For photovoltaic applications, it is therefore very important to develop a scheme that allows the use of the excess energy that would otherwise be wasted in heat. Several methods have been proposed to address spectral losses, and all these concepts concentrate on a better exploitation of the incident solar spectrum. Simply to enumerate a few, we can list:

- multiple exciton generation,
- down and up converter,

- luminescence downshifting.

In the literature, cells which implement these concepts are referred as Third or Next Generation photovoltaic cells [21]. The study of semiconductor nanocrystals represents a building block of these new concepts. Indeed, nanomaterials provide unique opportunities to optimize a number of physical, chemical, electrical, and optical properties of interest for photovoltaic devices. The challenge is to integrate these nanostructure properties and enhance the performances, reliability, and yield of the photovoltaic devices.

## 1.2 Light-matter interaction at the nanometer scale.

The dualism wave-particle, expressed by the relation<sup>2</sup>  $\lambda_{Br} = h/p$  and formulated in 1924 by Louis de Broglie [22], could be considered as the “heart” of nanotechnologies. Indeed, this principle is the answer to the question: when are the wave properties or the particle properties dominate for an atom? Let us use the analogy with optics. The wave nature of light becomes apparent at wavelengths comparable to the characteristic dimensions of obstacles<sup>3</sup> ( $L$ ), *i.e.*  $\lambda \sim L$ . If  $\lambda \ll L$ , the wave properties become negligible and we can use geometrical optics (rectilinear propagation of rays) to study physical phenomena. If we transpose these concepts to particle waves, *i.e.* to de Broglie waves, then the wave properties of particles will be more apparent if their dimensions are smaller than, or comparable to,  $\lambda_{Br}$ . If the particle dimensions are much larger than  $\lambda_{Br}$ , then the wave properties are weakly pronounced and they can be neglected.

Electron waves can propagate in any directions in a crystalline material. The situation radically changes when an electron is confined within a structure in which one of the directions of propagation is limited and it is comparable to the electron de Broglie wavelength. In this case the electron cannot propagate in this specific direction and it can be described as a standing wave. This leads to the existence of a non-zero discrete value of the energy, *i.e.* the electron energy is no longer continuous but instead its spectrum consists of a set of separate energy levels. The propagation of an electron wave in nanosize structures and its interactions with the boundary

---

<sup>2</sup>This principle connects to every momentum  $p$  a wavelength  $\lambda_{Br}$ .  $h$  is Plank’s constant.

<sup>3</sup>Interference and diffraction are examples of this phenomena.

surfaces produce effects of energy quantizations, interferences of incident and reflected waves, and tunneling through potential barriers. The degree of confinement leads to the classification of nanostructures in

- quantum well: confined in one dimension
- quantum wire: confined in two dimensions
- quantum dot: confined in three dimensions

In the following, we will treat only zero-dimension semiconductors, *i.e.* quantum dots (QDs).

It is obvious that as the particles become smaller and smaller, the laws of quantum mechanics become dominant in their interaction with light. In this situation, if the incident photon energy hits the energy difference of discrete internal (electronic) energy levels, scattering and absorption processes can be described as resonant interactions. Due to the resonant character, the light-matter interaction can often be approximated by treating the quantum system as an effective two-level system, considering only those two levels whose difference in energy is close to the interacting photon energy  $\hbar\omega_0$ . This description of nanoparticles as two-level systems is treated in more details in Chapter 4. When this resonant interactions take place, an electron (hole) is promoted to the conduction (valence) band. However, due to the restricted size of the system, the attractive Coulomb interaction, between the formed carriers, is efficient resulting in the formation of a bound state called excitons [23].

The excitons in semiconductors are described by a hydrogen-like Hamiltonian [24]

$$\hat{H} = -\frac{\hbar^2}{2m_h} \nabla_h^2 - \frac{\hbar^2}{2m_e} \nabla_e^2 - \frac{e^2}{\epsilon|r_e - r_h|} \quad (1.3)$$

where  $m_e$  and  $m_h$  are the effective masses of the electron and the hole, respectively, while  $\epsilon$  is the dielectric constant of the material. The subscript  $e$  and  $h$  refers to electron and hole. Once the size of the nanocrystal approaches the limit of the Bohr radius of an exciton ( $\sim 5\text{nm}$  for silicon [25]), the states of the exciton shift to higher energy as the confinement energy increases. Indeed, due to the Heisenberg uncertainty principle, the momentum, and so the energy, increases if the position becomes well defined. In the limit of small particle<sup>4</sup> the strongly screened Coulomb

---

<sup>4</sup>Particle dimension smaller than the Bohr exciton radius.

interaction between the hole and electron can be neglected<sup>5</sup>. As a consequence, both electron and hole can be described by the “*particle-in-the-box-model*”, which leads to discrete energy levels inversely proportional to the box-length<sup>6</sup> ( $a$ ):

$$\Delta E_n = \frac{\pi^2 \hbar^2}{m^* a^2} (n_1^2 + n_2^2 + n_3^2) = 3 \frac{\pi^2 \hbar^2}{m^* a^2} n^2 \quad \text{for } n_1 = n_2 = n_3 = n \quad (1.4)$$

where 3 is the confinement factor, *i.e.* the excitons are confined in all directions. Therefore, the electron-hole pair experiences increasingly strong confinement effects which significantly alter the allowed energy levels resulting in a size-dependent and increasingly discrete electronic structures (see Fig1.2).

The influence of quantum confinement on the optical properties of semiconductor nanocrystals has been intensively investigated in recent years [23, 25]. The main

<sup>5</sup>The last term in (1.3).

<sup>6</sup>In the approximation of infinitely high potential barriers.

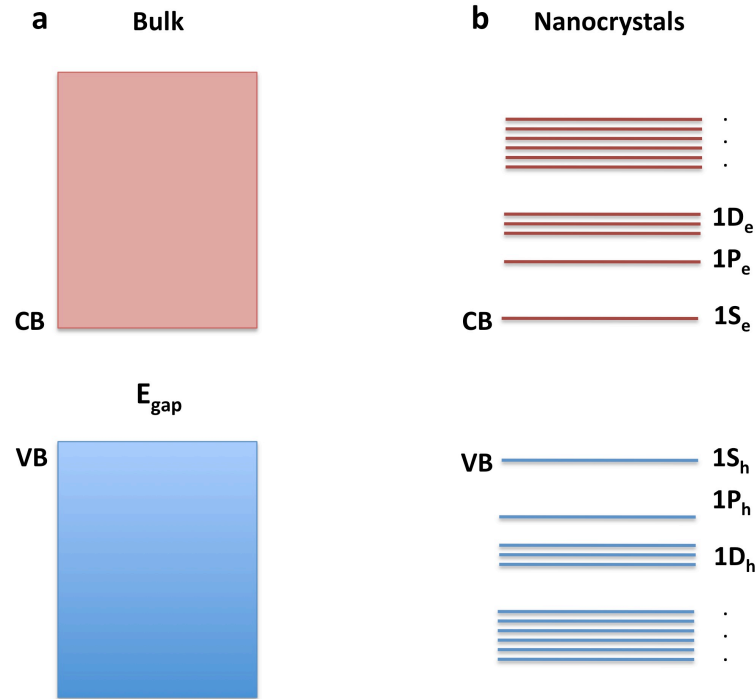


**Figure 1.2:** a) In bulk semiconductors the valence bands (VB) and the conduction bands (CB) form a continuum of electronic states separated by an energy gap  $E_g$ . b) In nanocrystals the quantum confinement effect generates a discrete energy spectrum in the conduction and valence bands.

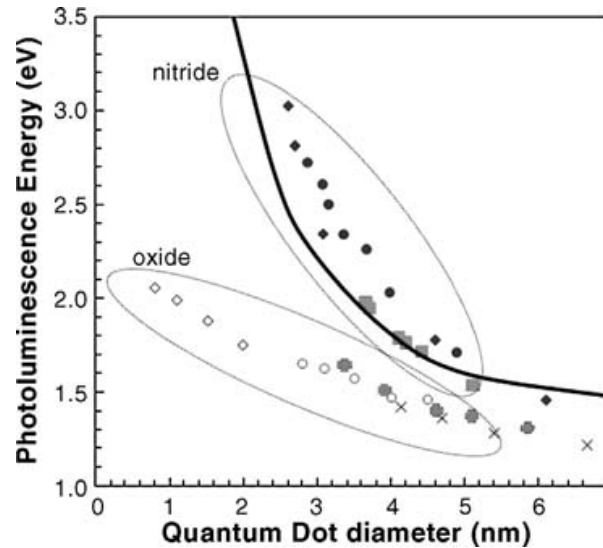


**Figure 1.3:** Measured luminescence bands from various authors' data for silicon quantum dots embedded in a silicon dioxide and nitride matrix as a function of the dot size [5, 26–31]. The continuum black line refers to the calculation of the energy shift using the equation (1.4) for spherical shape (from [25]).

manifestation of quantum size effect is a high-energy shift of the luminescence band and an enhancement of the spontaneous emission rate. This shift is easily explained using the equation (1.4): decreasing the particle size, the emission peak increases, as illustrated in Fig.1.3.

### 1.3 Multiple Exciton Generation: MEG.

Multiple exciton generation (MEG) is a carrier relaxation process characterized by the generation of multiple electron-hole pairs (multiple excitons) after the absorption of one single high energetic photon. Quantum confinement effects opens new perspectives on the study of the production of multiple electron-hole pairs with respect to bulk semiconductors, in which this effect is called impact ionization, as explained in section 1.1.

Because of the quantum confinement of electrons and holes in QDs, large intra-band energy gaps, equivalent to several phonon energy, suggest the possibility that carrier cooling rates may slow down due to the decreased efficiency of multi-phonon scattering events with respect to bulk semiconductors [14]. In more details, a consid-

eration based on the energy conservation predicts that, in QDs, a strongly reduced energy relaxation rate cannot be avoided within the intrinsic phonon scattering mechanism [32–35], unless the electron level spacing equals the LO-phonon energy, or is smaller than a few meV in favor of the LA-phonon scattering [36]: an electron on an excited level cannot relax to the fundamental one by inelastic phonon scattering unless the energy level separation is exactly equal to the phonon energy, which is likely to yield slow relaxation effects. The expected inhibition of this electronic relaxation is called phonon bottleneck<sup>7</sup> [12, 18, 36].

In the literature there are a lot of publications that explore “hot”-electron cooling/ relaxation dynamics and the issue of a phonon bottleneck in QDs. The results are controversial, and it is quite remarkable that there are so many reports that both support (for example [40–43]) and contradict (for example [44, 45]) the prediction of slowed “hot”-electron cooling and the existence of a phonon bottleneck in QDs. Following Nozik’s interpretation, one element of confusion is that the reported results are not indicative of a phonon bottleneck because the relaxation times are not excessively long and PL is observed<sup>8</sup>. However, some of these publications report relatively long “hot”-electron relaxation times, tens of ps, compared with what is observed in bulk semiconductors. Therefore, it is accepted that slowed relaxation/cooling of carriers occurs in QDs if the relaxation/cooling times are greater than 10 ps (about an order of magnitude greater than for bulk semiconductors) [12, 18, 19].

In addition to the phonon bottleneck effect, spatial confinement results in a strong carrier-carrier interactions within nanocrystals. Observations of photoluminescence (PL) blinking (intermittent PL as a function of time) detected in single QD [46], have been explained by an Auger process whereby if two electron-holes pairs are photogenerated, one pair recombines and transfers its recombination energy to one of the remaining charge carriers, ionizing it [46, 47]. Therefore, the exciton-exciton annihilation ejects an electron out of QD core, resulting in a charged nanocrystals for which the emission is quenched. After some time, the ionized elec-

---

<sup>7</sup>Not to be confused with “hot” phonon bottleneck [37–39], which refers to non-equilibrium LO phonon populations. LO phonons cannot equilibrate fast enough with the crystal bath and so they can be reabsorbed by the electron plasma to keep it hot [12, 18].

<sup>8</sup>Theory predicts infinite relaxation lifetime of excited carriers for the extreme, limiting condition of a phonon bottleneck; thus, the carrier lifetime would be determined by nonradiative processes and PL would be absent [12, 18].

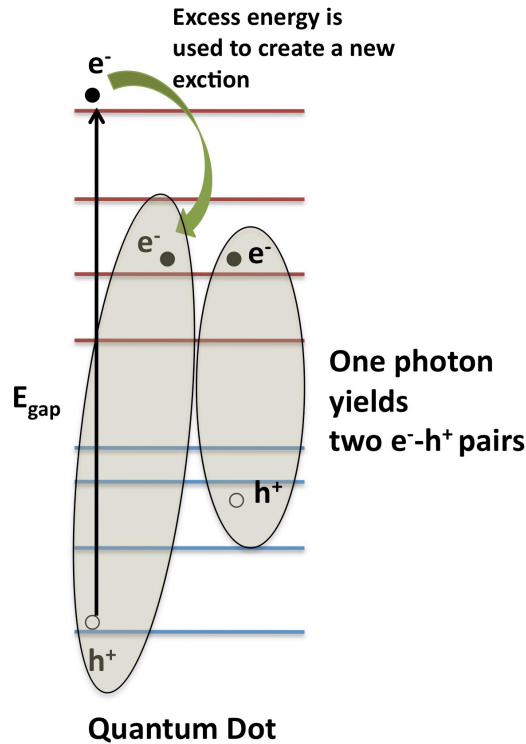


**Figure 1.4:** Multiple excitons generation (MEG) in QDs. After the absorption of a high energetic photon, an “hot” exciton is created. Due to discrete nature of the QD energy spectrum, the excess energy can be used to create another (or more) electron-hole pair (pairs).

tron can return to the QD core, and the PL is turned on again [47]. Because this Auger process can occur in QDs, the inverse Auger process of MEG, whereby one high energy electron-hole pair can generate two electron-hole pairs, can also occur in QDs (see Fig.1.4).

Conversion efficiency in photovoltaic devices can increase because the excess kinetic energy of electrons and holes, produced by absorption of photons with energies above the bandgap, can create additional excitons. The time scale for the MEG process ( $\tau_{MEG}$ ) has been estimated to be  $\tau_{MEG} < 100$  fs [43]. This time scale, identified by the green arrow in Fig.1.4, is much faster than the “hot” exciton cooling rate produced by electron-phonon interactions: MEG can therefore become efficient. Furthermore, crystal momentum is not a good quantum number for QDs [19]; thus the threshold photon energy for MEG can approach values as low as twice the threshold energy for absorption (the absolute minimum to satisfy

energy conservation) [18].

MEG has been detected monitoring the signature of multiexciton generation using femtosecond transient (pump-probe) absorption (TA) spectroscopy [18,19]. This technique observes the change in transmission of a weak probe beam in response to an intense photo excitation event. Following photon absorption by a semiconductor nanocrystal, the resulting electronic excitation consist of a conduction-band electron and a valence-band hole confined within nanoparticle. This produces two measurable effects in the absorption coefficient depending on the probe. In one type of transient absorption experiment, the probe pulse detects the interband dynamics ( $|1S_e, 1S_h \rangle$ , see Fig.1.2) resulting in a partial bleach of absorption [14], whereas in a second experiment, the probe pulse is in the mid-IR and reveals the intra-band transition (for example  $|1P_e, 1S_e \rangle$ , see Fig.1.2) of the newly created excitons. Therefore, two ultrafast femtosecond laser pulses are used. The first laser beam is used to excite the electrons and the other one probes the excited states.

The first observation of exciton multiplication for PbSe nanocrystals reported an energy threshold for the efficient formation of two excitons per photon at  $3E_{gap}$  [48]. However, in [43], the authors reported an energy threshold of  $2E_{gap}$  for the same nanosize system. Fig.1.5 reports the TA results performed on PbSe QDs [14]. Performing a data fit of these data, the authors reported a quantum yield<sup>9</sup> (QY)  $\sim 300\%$  [43]. Moreover, MEG was observed also for other semiconductors QDs (for more details, see, for example [49–51]).

As pointed out in section 1.1, one of the most important challenges is the possibility to extract “hot” carriers before their recombination to the band edges. Recently [13], this possibility was demonstrated for PbSe QDs. Using time-resolved optical second harmonic generation, “hot”-electron transfer from PbSe nanocrystals to a titanium dioxide electron acceptor was observed on an ultrafast time scale ( $< 50$  fs). These results indicate that “hot”-electron transfer from semiconductor nanocrystals to an electron acceptor is possible provided that the “hot” electrons and holes possess sufficiently long life times and that the interfaces are properly controlled to enable ultrafast charge transfer.

---

<sup>9</sup>Ratio of the emitted and absorbed photons.

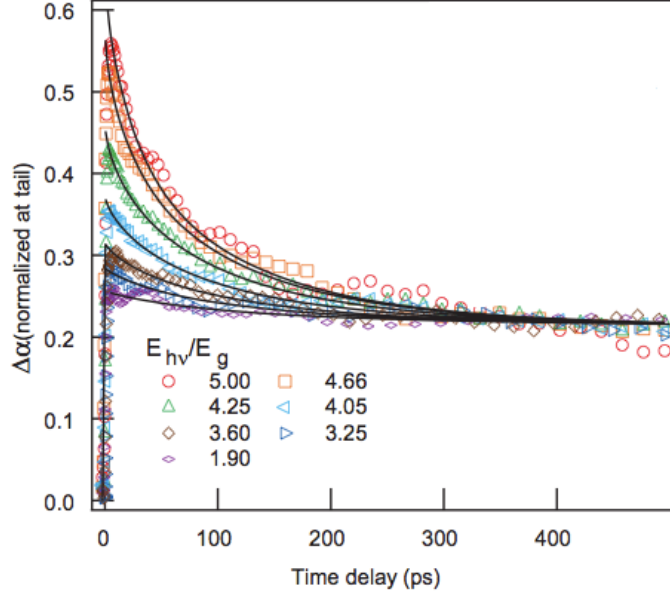


**Figure 1.5:** Exciton population decay dynamics obtained by probing intraband transitions in the mid-IR at  $5.0 \mu\text{m}$  for a sample of  $5.7 \text{ nm}$  diameter PbSe QDs (from [14]).

### 1.3.1 MEG in Si-QDs.

Silicon (Si) is widely used for solar cell fabrication. It has a band gap of  $1.12 \text{ eV}$  at  $300 \text{ K}$ , which is optimal not only for standard single p-n junction cell, but also for the bottom cell in a 2-junction or even 3-junction tandem stack. Therefore a solar cell entirely based on Si is advantageous in terms of potential for large scale manufacturing and for the long term availability of its constituents. In other words, Si is the most common material for solar cell.

Recent works have shown that colloidal Si-QDs, produced via flowing silane gas through a high energy plasma [52], also produce MEG with increased efficiency with respect to the impact ionization (I.I.) in bulk Si [53]. The threshold energy for this MEG process is  $(2.4 \pm 0.1)E_{gap}$  and the QY of excitons produced per absorbed photon reaches  $(2.6 \pm 0.2)$  at  $3.4E_{gap}$ . In contrast, for bulk silicon the threshold for I.I. is  $\sim 3.5E_{gap}$  and the QY rises to  $\sim 1.4$  at  $4.5E_{gap}$  [19, 54]. This difference between MEG and I.I. demonstrates the advantage in the use of nanometer sized semiconductors. The results presented in [53], are obtained using indirect ultrafast techniques, as explained in the previous section.

Other studies on Si-QDs, based on different experimental techniques [41, 55] with

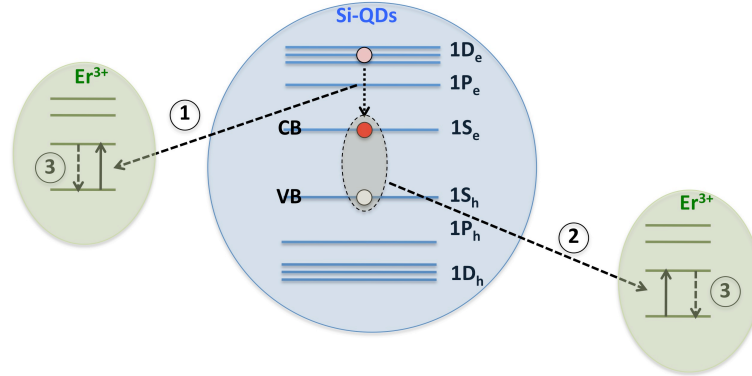


**Figure 1.6:** After the absorption of one incident photon with energy greater than  $\sim 2.6\text{eV}$ , an exciton, with excess energy, is created; 1) the energy released by the intraband Auger recombination excites one  $\text{Er}^{3+}$  ion; 2) excitation of a second  $\text{Er}^{3+}$  ion due to the band to band recombination of the quantum confined exciton; 3) Erbium emission. In this scheme one absorbed photon produces two emitted photons from the two  $\text{Er}^{3+}$  acceptors.

respect to TA, revealed important characteristics related to the dynamics of multiple generation of electron-hole pairs. Space-separated quantum cutting (SSQC) is a process in which the excess energy can be transmitted outside the photo-excited system. In order to demonstrate this energy transfer channel, Timmerman *et al.* [55] performed two different experiments using Si-QDs embedded in a silicon dioxide matrix ( $\text{SiO}_2$ ) produced by sputtering on a quartz substrate. In the pilot experiment,  $\text{Er}^{3+}$  ions, located outside the Si-QDs, are employed as receptors using their characteristic photoluminescence (PL) to detect the phenomena. A clear enhancement of the QY for energies above  $\sim 2.6\text{ eV}$  (480nm) was observed. This enhancement was related to the excess energy of the “hot” carrier that is large enough to allow an intraband relaxation Auger process with simultaneous erbium excitation. As a result, two  $\text{Er}^{3+}$  ions can be excited per single photon absorbed by Si-QDs (see Fig.1.6). In the second experiment, the authors used the same strategy applied to a sample with only Si-QDs. Also in this situation, an improvement of the QY was detected for an energy threshold of the incident photon larger than  $2E_{QD} \approx 3\text{eV}$  ( $E_{QD}$  is the Si-QD bandgap). This result demonstrates that the Si-QDs themselves can play a receiver-role : a second nanocrystals can be excited by its neighboring that contains a “hot” electron-hole pair (see Fig.1.7).

In order to analyze in more details the different mechanisms related to the MEG

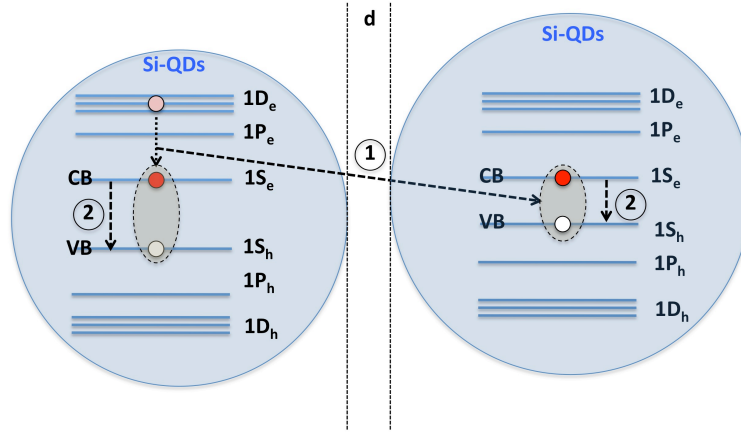


**Figure 1.7:** After the absorption of one incident photon with energy greater than  $\approx 3eV$ , twice the Si-QDs energy gap, an exciton, with excess energy, is created; 1) the energy released by the intraband Auger process excites a neighboring Si-QDs; 2) photoluminescence emission generated from interband recombination of the quantum confined exciton in both Si-QDs.  $d$  represents the particle-separation.

emission, excitation wavelength measurements of photoluminescence quantum yield (PL QY) for Si-QDs were performed [41]. Si-QDs were fabricated using different approaches: co-sputtering of silicon and SiO<sub>2</sub> on a quartz substrate and porous silicon grains suspended in ultraviolet-grade ethanol made by electrochemical etching of crystalline silicon. These nanocrystals display unexpected behavior indicating that a new physical mechanism is begin activated upon excitation with higher-energy photons: the initially low constant value of QY for lower-photon energies is followed by a step-like increase for higher-photon energies [41]. This step-like behavior of PL QY as a function of photon energy can be explained as a phenomena of carriers multiplication. Each time the excess energy of an excitation photon overcomes the threshold of a multiple of the bandgap energy, one more electron-hole pair can be generated increasing the free carrier population. In this way the PL signal, generated by interband recombination of quantum confined excitons [25] (see Fig.1.7), increases, and so also the QY. The step-like behavior of QY can then been seen as the most characteristic fingerprint of this process. Differently from the other reports on MEG based on TA technique [12, 18, 19, 43, 53], in this study MEG is observed by the enhancement of radiative recombinations. Because the Auger recombination inside Si-QDs is approximatively six orders of magnitude

faster than radiative decay, the excitons can be efficiently separated into different nanocrystals [41]. Therefore, it is expected that the separation between QDs plays a predominate role.

Recently a fully *ab initio* scheme has been proposed to clarify the role of silicon nanoparticle interaction in the carrier multiplication dynamic [40]. In this study, three different carrier multiplication processes have been identified, when the Si-QDs interaction is turned on:

- One-site<sup>10</sup> MEG (see Fig.1.4).

- Two-site mechanism:<sup>11</sup>

1. Space Separated Quantum Cutting (SSQC): high-energy carrier can decay to a lower energy state and transfer its energy to a nearby Si-QDs where an new exciton is promoted. This effect can be responsible for the generation of multiple excitons distributed in the different Si-QDs after the absorption of one high-energy photon. SSQC is illustrated in Fig.1.7

<sup>10</sup>One-site means that this mechanism takes place on single nanocrystals.

<sup>11</sup>Carrier-multiplication-dynamic that involves two neighboring Si-QDs.

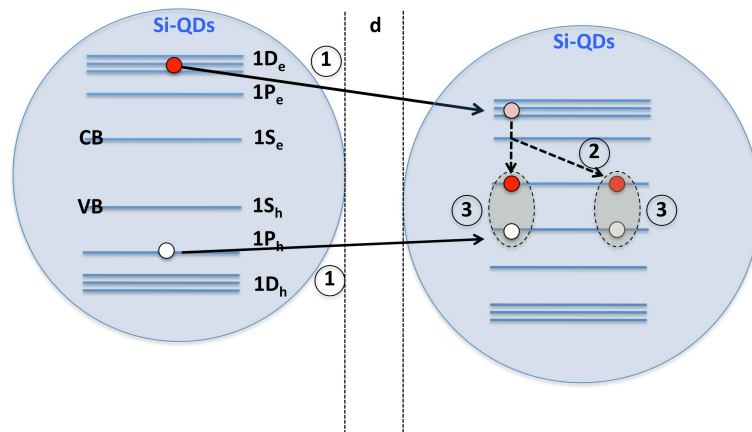


**Figure 1.8:** 1) Non radiative scattering processes can move one or more carriers from one Si-QD to another; 2) The excess energy produced by the Auger intraband transition generates a new electron-hole pair; 3) photoluminescence due to the interband recombination of quantum confined excitons.

2. Coulomb Driving Charge Transfer (CDCT): non-radiative scattering processes can move one or more carriers from one Si-QD to another, producing a charge transfer with the generation of an extra electron-hole pair (see Fig.1.8)

Moreover, the crucial role of nanocrystal-nanocrystal separations was examined studying wave-function delocalization: two separated interacting nanocrystals can be depicted as a unique quantum confined structure where quantum states can spread among both nanostructures. The results and the dynamics of the carrier multiplication, including the nanocrystals-nanocrystal interaction, presented in [40] are compatible with the experimental observation of SSQC [41, 55], demonstrating the real possibility in the use of Si-QDs to improve the performances of a standard photovoltaic device.

Although the MEG is demonstrated in different nanostructures and it is detected using different experimental techniques, there are no experimental results yet that demonstrate improved performances in solar cell characterized by MEG processes. Following Gupta's analysis [56], one of the big problems concerning the exploitation of this mechanism in real devices, is the pumped power used to detect MEG. These experimental conditions have nothing to do with the required conditions for solar cell applications. However, the research efforts are concentrated in the study of novel designs that can harvest the demonstrated advantages of the carrier-multiplication-dynamic [18, 57].

## 1.4 Solar Spectrum Modification.

Modification of the incident solar spectrum by means of the down/up conversion or luminescence downshifting represents a relatively easy and cost-effective way to enhance the energy conversion efficiency of single junction cells [58]. Down-converters or shifters are located on top of a solar cell as they are designed to modify the spectrum such that UV photons are converted to red photons leading to a more red-rich spectrum that is used more efficiently by the solar cell. Up-converters modify the spectrum of photons that are not absorbed by solar device to effectively shift the infra-red (IR) part of the transmitted spectrum to the near-infra-red (NIR) or visible part, as a back reflector. Fig.1.9 displays a schematic drawing of a solar device characterized by these mechanisms. Modifying the incoming spectrum can

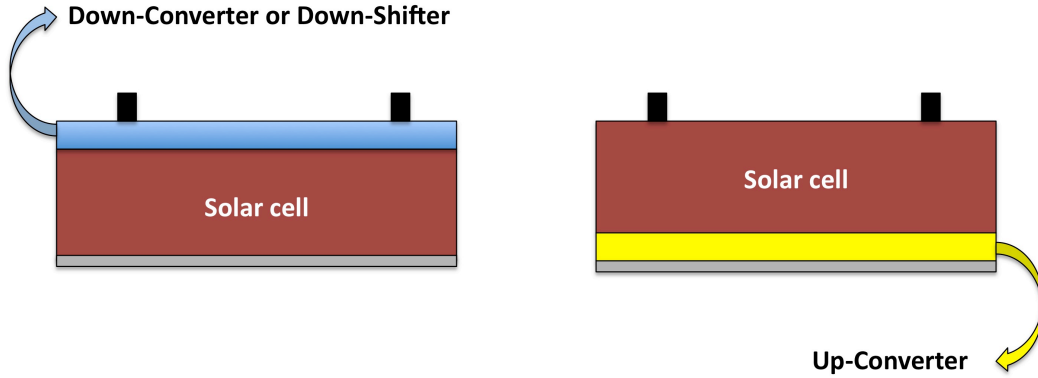


**Figure 1.9:** Schematic drawing of a solar cell with a down converter (or down shifter) layer on top (left) and an up-converter layer on the bottom (right).

be realized by incorporating “active” layers above (for down-conversion and luminescent down-shifting) or below (for up-conversion) existing solar cells made with established high-efficiency processes. No modification is needed, as in the case with the impurity photovoltaic device, and with the intermediate band solar cell [59]. Neither a complicated structure such as that used for tandem solar cells is necessary.

All these mechanisms influence the solar cell performances only optically. Fig.1.10 shows the parts of the solar spectrum affected by these new concepts. The red line displays the simulated Internal Quantum Efficiency (IQE) of a commercial silicon solar cell. IQE represents the efficiency with which photons that are not reflected or transmitted out of the cell can generate collectable carriers. As explained in section 1.1, conventional solar devices do not use efficiently high energy photons ( $Eh\nu > 2E_{gap}$ ) and photons with energy lower than the energy bandgap ( $Eh\nu < E_{gap}$ ). IQE reflects this situation: low-blue and low-IR IQE indicate the inability to use, respectively, high energy photons due to heat losses and photons with energy lower than  $E_{gap}$  due to unabsorbed energy losses. The basic idea of the solar spectrum modification is to shift the parts of the incident radiation that are not used efficiently by the solar cells into the energy range where IQE shows its flat maximum value <sup>12</sup> resulting in an enhancement of light-generated-carrier effectively used by solar devices.

<sup>12</sup>Between 600nm-900nm for a silicon solar cell.

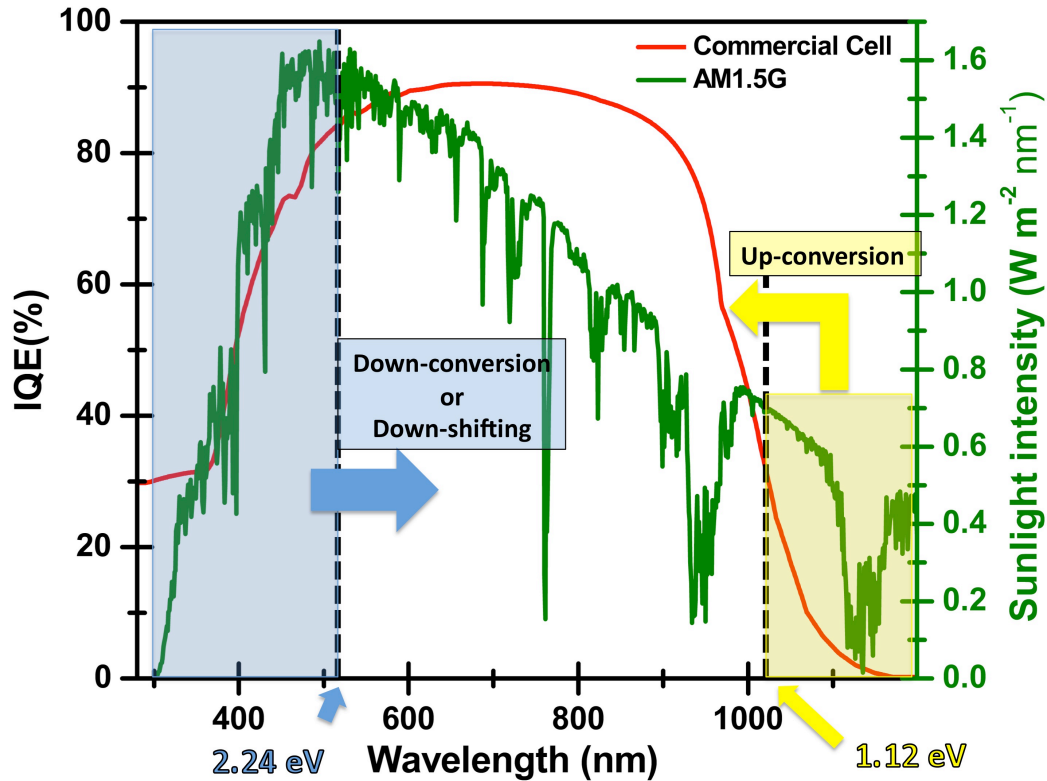


**Figure 1.10:** Parts of solar spectrum (green line) affected by Down-conversion/Down-shifting (blue box), and Up-conversion (yellow box).  $2.24 \text{ eV}$  ( $2E_{\text{gap}}^{\text{silicon}}$ ) and  $1.12 \text{ eV}$  ( $E_{\text{gap}}^{\text{silicon}}$ ) are the lower and upper bounds for the activation of Down-conversion/Down-shifting and Up-conversion for a silicon solar cell, respectively. The red line displays the simulated Internal Quantum Efficiency (IQE) of a commercial silicon solar cell, performed using the Silvaco software tool [60] (for more details see subsection 2.2.3).

### 1.4.1 Down and Up Conversion

Down-conversion (DC) is a process in which a high energy photon is split into two low energy photons (Fig.1.11). Consequently, the number of “hot” carriers decreases and the available energy lost by carrier thermalizations is diminished. DC was theoretically suggested first by Dexter in the 1950s [61,62] and shown experimentally 20 years later using lanthanide ion praseodymium  $Pr^{3+}$  in an yttrium fluoride  $YF_3$  host [63,64].

The DC effect can produce theoretically an energy conversion efficiency of  $\sim 36.5\%$  [65] for non concentrated sunlight when applied in a single junction solar cell. In

the literature, DC is a different way with which we can call SSQC. Indeed, as explained in details in subsection 1.3.1, SSQC is a process in which one absorbed photon produces two emitted photons. Recently [66] it has been proposed a study on the electrical and optical characteristics of a silicon solar cell coated with SiO<sub>2</sub> compared with a silicon solar cell characterized by an anti reflection silicon rich oxide (SRO) coating layer containing silicon nanoparticles. An improvement of the spectral response, short-circuit current, and open circuit voltage was observed in the solar cell containing SRO with respect to a reference cell covered with 495 nm of SiO<sub>2</sub>. These enhancements were explained as manifestation of the DC effect (for further details [66]). However, it is important to note that 495 nm is not the optimal thickness ( $d^{opt}$ ) for an anti-reflection coating composed by SiO<sub>2</sub> ( $d_{SiO_2}^{opt} \sim 105\text{nm}$ ). Nevertheless, it can be argued that performances of the the reference solar cell are not the optimal ones producing an overestimation of the effect.

Up-conversion (UC) is a non-linear optical process in which at least two low energy photons (near infrared region) are converted into a high energy photon (visible region) [67,68] (Fig.1.12). UC materials are most suitable for solar cells having large bandgaps. This mechanism usually combines an active ion, of which the energy level scheme is employed for absorption, and a host material in which the active ion is embedded.

The application of an up-converter can potentially lead to a maximum conversion efficiency of  $\sim 37\%$  employed on the back of silicon solar cells [69].

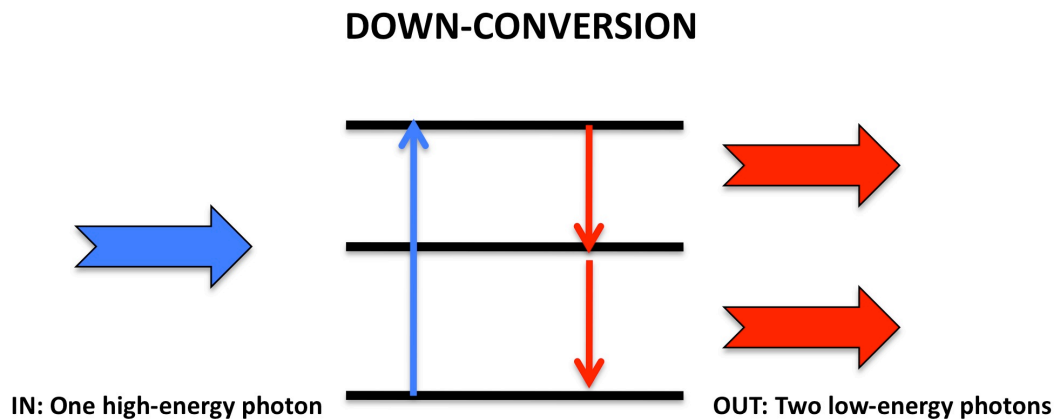


**Figure 1.11:** Down-Conversion effect: one-high energy photon is absorbed and two low-energy photons are produced.

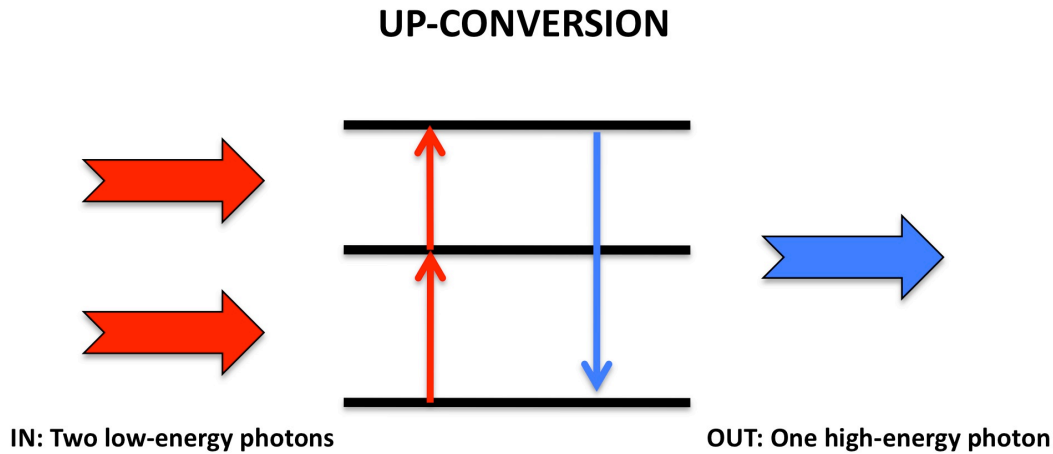


**Figure 1.12:** Up-Conversion effect: two low-energy photons are absorbed and one high-energy photon is generated.

For further details on the materials applied on different types of solar cells for down and up conversion, see [70, 71]

### 1.4.2 Luminescence Downshifting

The luminescent downshifting (LDS) effect is similar to the down-conversion. However, only one photon is emitted and part of the excess energy is lost due to non-radiative relaxation processes (see Fig.1.13). Therefore, the quantum yield is lower than unity. LDS can be employed to overcome poor blue response of solar cells [72] due to non-effective front surface passivation. A LDS layer is used to transform high-energy photon, for which the cell IQE is low, to a lower energy-photon, for which the cell IQE is high, thereby increasing the short-circuit current and the cell efficiency. This effect can theoretically enhance the overall conversion efficiency by  $\sim 10\%$  [73].

In order to benefit from LDS effect, the following conditions should hold in a silicon solar cell (see Fig.1.10):

- excitation at wavelength shorter than 450 nm,
- emission between 450 nm and 1100 nm,

- low absorption in the region of the spectrum that will not shifted, since these wavelengths must be transmitted to the underlying solar cell.

However, in addition to the potential efficiency enhancement, the introduction of a LDS layer in a PV module can also create additional interactions with the light resulting in extra loss mechanisms. These additional losses can originate from two sources: the host material and the luminescence “centers”. The main physical loss processes that can take place are

1. parasitic absorption from the host material,
2. re-absorption from the luminescent “centers” due to partial overlapping of its absorption and emission bands,
3. increased reflection due to the introduction of an additional interface,
4. losses through top and side planes of the layer, as the emitted light could not be directed efficiently towards the solar cell.

Therefore, a suitable active material must be selected considering all these phenomena.

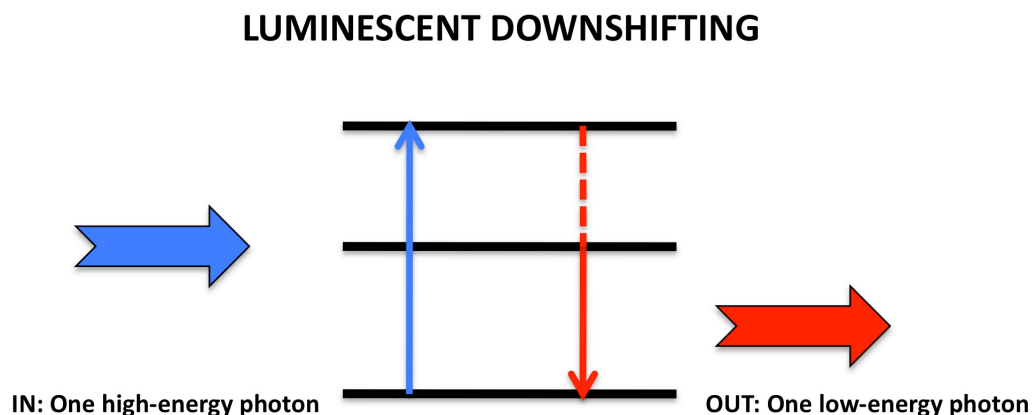


**Figure 1.13:** LDS effect: one high-energy photon is absorbed and one low energy photon is emitted. Part of the excess energy is lost due to non-radiative relaxation processes.

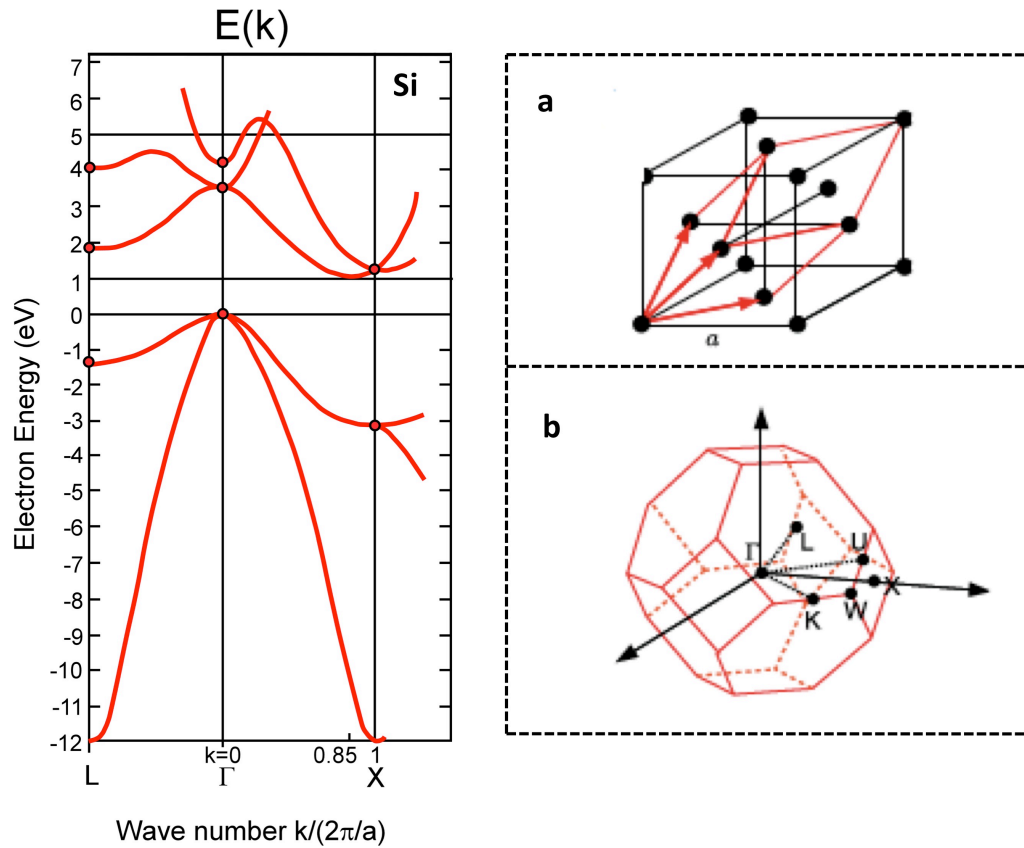


**Figure 1.14:** Electronic band structure of bulk Si. A schematic of the face centered lattice (fcc) fundamental cell (a) and first-Brillouin zone (b) is illustrated.

## 1.5 Material under investigation: bulk and nano-structured silicon.

Silicon (Si) is the electronic material per excellence. Integration and economy of scale are the two keys ingredients for the silicon technological success. However, silicon has bad light emitting properties.

Si is an indirect band gap material, thus the probability for a radiative transition is very low. The indirect radiative interband transitions in bulk Si are strongly suppressed because an emitted photon cannot satisfy the momentum conservation law for transitions from conduction-band minima ( $X$ -points) to the top of the valence band ( $\Gamma$ -point), as illustrated in Fig.1.14. The photon wave vector is about three orders of magnitude lower than that required for the transition between  $X$ - $\Gamma$

points. This difference in  $\mathbf{k}$ -space is  $\Delta k = 0.86 \times 2\pi/a$ , where  $a$  is the lattice constant of silicon, equal to  $5.43 \text{ \AA}$  [74]. The electron-hole radiative recombination in bulk Si is forbidden, unless additional mechanisms take place in the recombination processes allowing the momentum conservation. The most probable way to have a radiative indirect transition is via phonon absorption or emission. However, the electron-phonon interaction is weak: phonon assistance is a low-probability process. Indeed, the probability associated with this process is of the order of  $10^{-4}$ ,  $10^{-3} \text{ s}^{-1}$ , which is more than five order of magnitude lower than the direct radiative recombination ( $\Gamma - \Gamma$  transition) rate in III-V semiconductor materials ( $\sim 10^{-9} \text{ s}^{-1}$ ) [74]. This peculiarity makes non-radiative processes, such as Shockley-Read-Hall (SHR) recombination Auger and Free Carrier Absorption, much more efficient in reducing the excitons population, quenching the light emission in Si. Moreover, the large electron mobility ( $\sim 2 \times 10^3 \text{ cm}^2 \text{ V}^{-1} \text{ s}^{-1}$  [75]) makes the non-radiative recombinations a non-negligible effect which contributes in quenching the radiative recombination.

The discovery of visible emission from nanocrystalline [5] and porous silicon [6–8] in the early 1990s, opened a new scenario in which the problems associated with the silicon band structure might be overcome in nanoscale crystallites hosted in a widegap dielectric matrix. Electronic states become localized within silicon

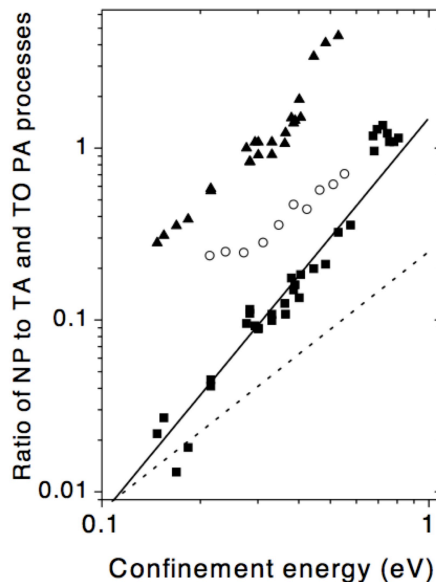


**Figure 1.15:** Breakdown of  $\mathbf{k}$ -conservation rule for different Si-NCs sizes and samples (from [76]).

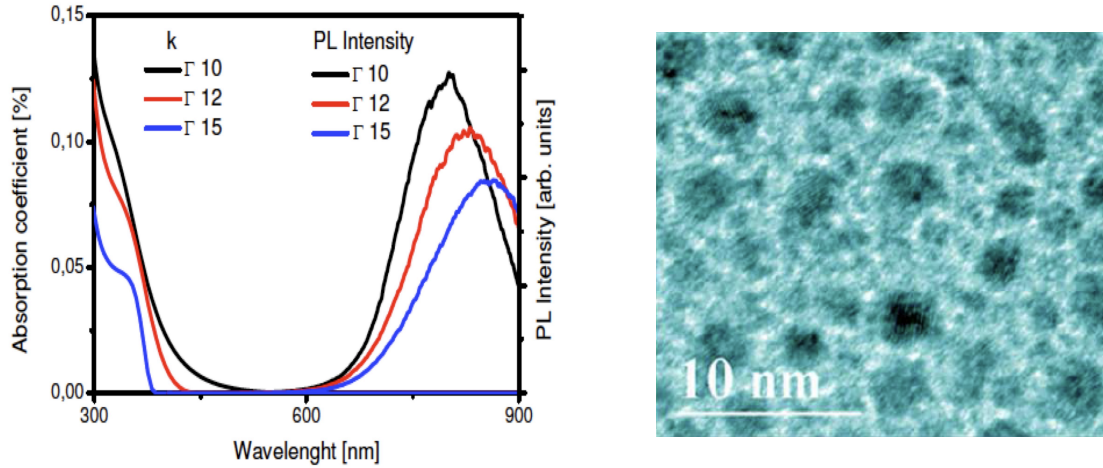


**Figure 1.16:** Left-side: absorption coefficient and photoluminescence spectra of different layers containing Si-NCs produced by our partners in Fondazione Bruno Kessler (FBK) using different  $\Gamma$  concentrations (from [77]). Right-side: HRTEM image of tiny Si-NCs in  $\text{SiO}_2$  matrix. Si-NCs appear as dark structure and the (111) lattice plans are clearly seen. Their dimensions shown in the image is between 2 and 5 nm (from [77]).

nanocrystals (Si-NCs) resulting in a reduction of the electron mobility with respect to the bulk Si. Moreover, the momentum distribution spreads due to Heisenberg uncertainty principle relaxing the  $\mathbf{k}$ -conservation rule with a consequently increase of the optical transition rate. Fig.1.15 illustrates a study in which the transition rate of no-phonon (NP) direct transition rates is compared with phonon-assisted (PA) optical transitions for different samples as a function of the quantum confinement energy (see equation (1.4)). White open circles show a progressive breakdown of the selection rule with the size particle reduction for Si-NCs embedded in  $\text{SiO}_2$  [76]. Thus, the momentum conservation law is not violated, which yields a nonzero probability of the  $X$ - $\Gamma$  radiative recombination even in the absence of phonons in Si-NCs.

Indeed, efficient visible photoluminescence from Si-NCs was experimentally demonstrated (e.g. [78]) and attributed to the interband transition between confined electron and hole states inside the nanocrystal [79, 80] and/or between interface states [81–83]. Further characteristics on the emission from Si-NCs are analyzed in section 4.4.

### 1.5.1 Si-NCs as LDS material.

As explained in subsection 1.4.2, the materials used as LDS layer must satisfy specific requirements in order to maximize the benefits from their application.

Our choice was to use Si-NCs embedded in a SiO<sub>2</sub> matrix. The most common fabrication technique is based on the deposition of a non-stoichiometric Silicon-Rich-Silicon-Oxide<sup>13</sup> (SRO). A subsequent annealing step (temperature of 1000 - 1100 °C), separates the Si excess from the Silicon oxide, forming individual, usually spherical, crystalline domains. Fig.1.16 (Left-side) illustrates the absorption coefficients and the PL spectra of Si-NCs obtained using this technique. In this type of measurements, due to the dimensions of the light spot and the large density of silicon QDs, a huge number of QDs is measured at the same time:  $\sim 10^{11}$  QDs in the photoluminescence and about  $\sim 10^{12}$  QDs in the ellipsometric measurements from which the absorption coefficients were obtained [77]. The absorption coefficient increases with increasing silicon content ( $\Gamma$ -value refers to the ratio of the gases SiH<sub>4</sub> and N<sub>2</sub>O used

<sup>13</sup>Silicon rich or excess silicon means that the film contains an excess of silicon with respect to the ratio 1:2 between Si and oxygen in stoichiometric silicon dioxide (SiO<sub>x</sub>).

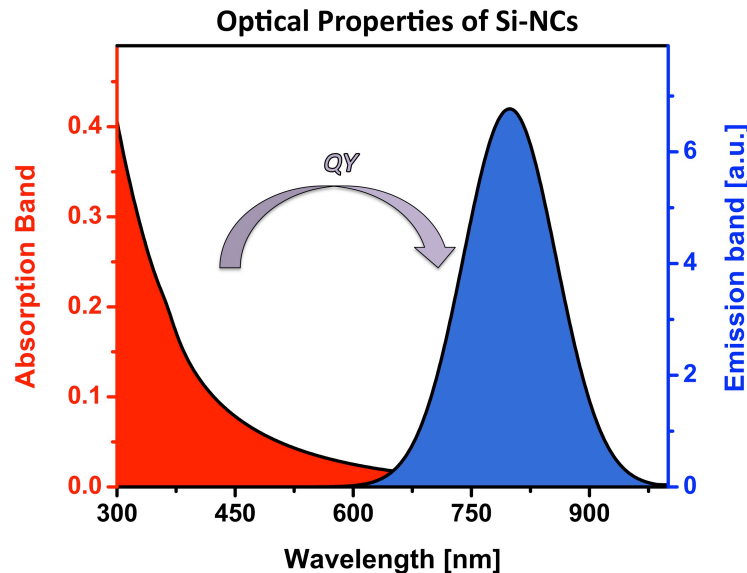


**Figure 1.17:** Absorption (red) and Emission (blue) band of our Si-NCs dispersed in SiO<sub>2</sub>. The violet arrow indicates the efficiency of the red-conversion of the blue-absorbed photons. For Si-NCs was reported a QY of  $\sim 60\%$  [84].

during the deposition of the films). The PL spectra, measured at room temperature, of these samples show a broad photoluminescence band in the visible near-infra-red region, which shifts from 800 nm to 850 nm for decreasing silicon content. A high resolution TEM image of tiny Si-NCs embedded in SiO<sub>2</sub> with dimensions of about 2-5 nm is shown in Fig.1.16 (Right-side).

First of all, the use of SiO<sub>2</sub> as host guarantees high transmittance, particularly in the region where the cell's response is high. At the same time, it provides an optimal environment for our emitters because it creates a strong confinement potential for carriers inside Si-NCs [85]. Fig.1.17 shows a large Stokes shift between absorption and emission band which yields a reduction of the losses due to the re-absorption of the emitted light. Moreover, in the literature was reported a high QY for Si-NCs: ~60% [84] and, additionally, their emission wavelength can be easily tailored by a size change.

The other requirements, discussed in subsection 1.4.2, will be analyzed in Chapters 2 and 4 showing that Si-NCs are good candidate as LDS material.

## 1.6 Conclusions.

In this chapter, it was presented an overview of the state of the art on Third generation photovoltaic technology. In particular, we motivated the use of nanostructured materials in the photovoltaic scenario. New phenomena generated by light-matter interaction at nanometers scale are analyzed. Concepts as impact ionization, multiple exciton generation, space-separated quantum cutting, and solar spectrum modification are presented, and their possible improvements of solar cell performances are discussed.

Our approach on luminescence downshifting effect (LDS), a concept based on the modification of the incident sunlight radiation, is introduced: our aim is to use silicon nanoparticles dispersed in a silicon dioxide matrix in order to improve the performances of a standard silicon solar cell exploiting the photoluminescence properties of our active material. This choice shows good potentiality as a candidate for LDS material:

- high absorption band below 450 nm,
- good emission in the range 750 nm-850 nm,

- good separation between the absorption and emission band (reduction of the re-absorption losses).

The other properties of Si-NCs as LDS material and the results on their implementation on silicon solar cells will be debated in the next chapters.



---

## Chapter 2

# Silicon Nanocrystals for downshifting applications.

The actual photovoltaic market is dominated by silicon solar cells. However, to address future needs in electricity in the order of  $\sim 30$  TW, the cost of solar energy will have to be significantly lower and, at the same time, the efficiency will have to be increased with respect to actual values. With these requirements it is understandable that the interest in exploring the properties of silicon nanostructures in solar cells is enormously increased in the last years.

In this chapter, I will introduce the integration of a novel silicon quantum dots (Si-QDs) layer presenting a preliminary study based on different front contact silicon solar cells characterized by different silicon rich oxide thicknesses as active material [86]. The performances of these devices were compared with respect to a reference cell coated with only silicon dioxide. This analysis permitted us to figure out the main problems related to the aim of our research activity: the fabrication of a novel photovoltaic device based on Si-QDs.

First of all, in section 2.2, I will present the problem of optical losses produced by the mismatch between the refractive index of the used materials. A model of a luminescence downshifting (LDS) layer, consisting of Si-QDs embedded in a silicon dioxide matrix on a silicon solar cell, is presented [87]. This model is based on the transfer matrix method in combination with a phenomenological approach describing the photoluminescence behavior of our active emitters. The optimal thickness values to enhance the LDS effect were obtained by minimizing the reflection while maximizing the photon flux which arrives on the underlying solar cell due to the

Si-QDs absorption and emission. Moreover, an experimental determination of the quantum yield (QY), based on the method underlined in [84], will be presented in subsection 2.2.2 to validate our assumption of QY=10% in the simulations. The results of this optimization will be used within the European Project LIMA (Improve Photovoltaic efficiency by applying novel effects at the limits of light to matter interaction) in order to produce an optimal interdigitated back contact (IBC) silicon solar cell including Si-QDs.

At the end, I will show and discuss the results obtained in this european project. Here, I will describe the problems, and the adopted solutions, manly related to the high annealing step ( $\sim 1100$  °C) necessary for the silicon nanocrystal formations during the fabrication process of IBC solar devices in an industrial environment.

## 2.1 Preliminary study on the LDS effect based on Si-NCs

### 2.1.1 Photoluminescence downshifted solar cell

The starting point of our study on the LDS effect based on Si-NCs was the production of a photoluminescence downshifted (PDS) solar cell [86]. Fig.2.1 shows the cross section of the studied device. This solar cells was obtained using floating zone (FZ) silicon substrates ( $280 \mu\text{m}$ ,  $< 100 >$ , front side polished, resistivity  $0.3\text{-}0.7 \Omega \text{ cm}$ , p-type), the back-side was boron implanted resulting in a sheet resistance of  $10 \Omega/\text{square}$  measured at the end of the processing. The top-emitter was realized by phosphor diffusion (sheet resistance  $80 \Omega/\text{square}$ ). The silicon rich oxide (SRO) layer was deposited by plasma enhanced chemical vapor deposition technique (PECVD). The ratio of gas flows between  $\text{N}_2\text{O}$  and  $\text{SiH}_4$  during the deposition process was 15 (for more details on this parameter, see subsection 1.5.1). The activation of boron and phosphor together with the growth of Si-NCs was achieved by a thermal annealing at  $900$  °C for 30 min in  $\text{N}_2$  atmosphere. The SRO on top of the emitter was etched by reactive ion etching before metallization (aluminum (Al) deposited by DC-sputtering). The front metal is composed of fingers with two bus bars for current collection. The back-side of the cell is completely covered by Al. The size of the cell is  $4.25 \text{ mm} \times 4.25 \text{ mm}$ , with an active area of  $3.70 \text{ mm} \times 4.25 \text{ mm}$ .

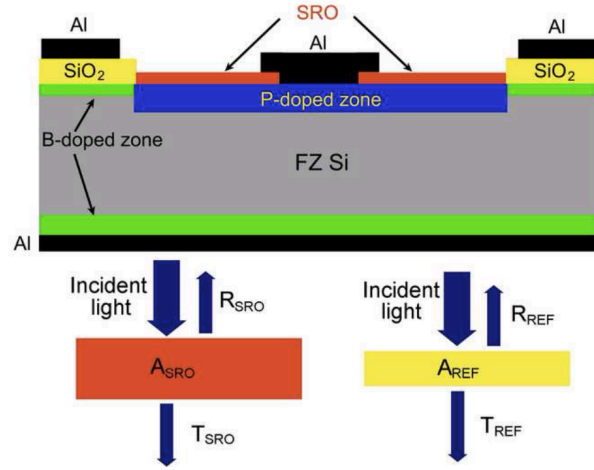


**Figure 2.1:** Top panel: schematic cross-section of the solar cell under study when covered by a silicon rich silicon oxide (SRO) layer (red). Bottom panel: the different optical functions for the SRO layer (left) or the SiO<sub>2</sub> layer (right) (from [86]).

In order to study the active role of Si-NCs, three devices have been produced at the Advanced Photonics & Photovoltaics group, Fondazione Bruno Kessler (Trento - Italy):

1. a cell with 105 nm thick SiO<sub>2</sub> layer<sup>1</sup>, which plays the role of the reference cell labelled REF
2. a cell with a thin (235 nm) SRO layer labeled PDS-1
3. a device with a thick (677 nm) SRO layer labelled PDS-2

### 2.1.2 Results, discussion, and future perspectives.

Control samples of SRO layers were deposited on Si wafers and characterized by X-ray photoelectron spectroscopy (XPS) to analyze the optical properties of the produced Si-NCs. The details about XPS analysis and techniques could be found in [88]. Optical properties of these control films were investigated with variable-angle ellipsometric and photoluminescence (PL) spectroscopy.

After the high temperature annealing, Si-NCs precipitate inside the SRO layer [25]. This was confirmed performing PL measurements (Fig.2.2a) . PL spectra were

<sup>1</sup>This thickness is the optimal one for a silicon dioxide anti reflection coating (ARC).

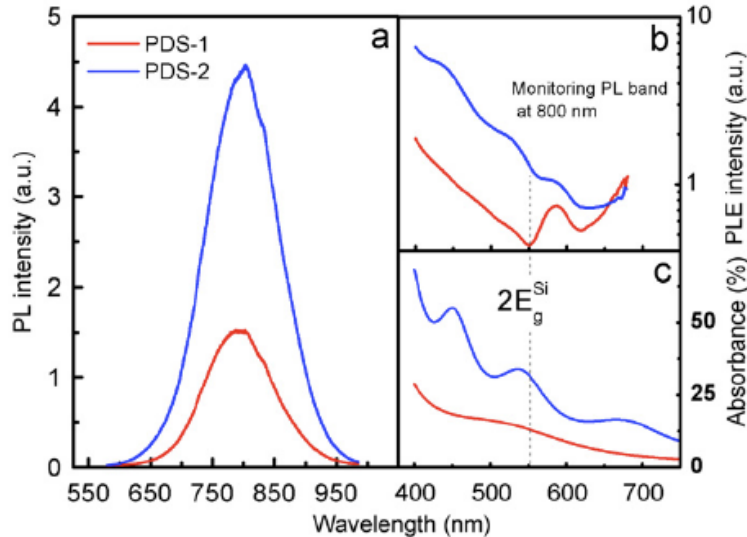


**Figure 2.2:** a) Photoluminescence spectra measured with an excitation wavelength of 532 nm; b) photoluminescence excitation performed used a Cary Eclipse Fluorescence set-up and the wavelength of incident light was scanned from 400 nm to 680 nm; c) absorbance spectra (from [86]).

measured at room temperature using the 532 nm line of a Diode-Pumped-Solid-State laser. The signals were collected using a GaAs photomultiplier tube (PMT). These spectra have been normalized to the spectral response of the detector. PDS-2 and PDS-1 shows emission bands peaked at 800 and 790 nm respectively. Due to the larger thickness, PDS-2 displays a stronger emission intensity than PDS-1. This difference is due to the larger optical density of PDS-2 than that of PDS-1, which means higher absorption as well as stronger emission.

Photoluminescence excitation (PLE) spectra, measured with a Cary Eclipse Fluorescence spectrometer, are reported in Fig.2.2b. The wavelength of incident light was scanned from 400 nm to 680 nm and the emission signal was collected at 800 nm, *i.e.* around the maximum values of PL spectra. These measurements display an exponential increases of Si-NCs light emission as the excitation photon wavelength decreases. Moreover, PLE experiments permit to measure the characteristic absorption of Si-NCs. Indeed, this parameter can be measured directly by transmission measurements, but these experiments may be affected by absorption that is essentially unrelated to the excitation of quantum confined excitons in Si-NCs. On the contrary, PLE experiments primarily show that the absorption properties

of a Si-NCs are mainly determined by the Si atoms contained in its volume and constituting it [89]. However, for excitation wavelengths smaller than 400 nm, the curve relative to the excitation cross section of Si-NCs starts departing from the absorption of bulk Si because in this energy range the effect of quantum confinement dominates. PL and PLE spectra demonstrate that our emitters absorb in the blue and emit in the red.

The reflectance spectra of the various cells were measured from 300 nm to 1700 nm at different angles using ellipsometry. The dielectric function was extrapolated by a standard least square regression analysis. We used a thin film modeling software (Scouts<sup>®</sup>), and the optical parameters measured by an ellipsometer, to fit these reflectance spectra. From the simulation and by using the definition of Fig.2.1 (bottom panel), we deduced the reflectance ( $R_{SRO}$ ,  $R_{REF}$ ), the absorbance ( $A_{SRO}$ ,  $A_{REF}$ ), and the transmittance ( $T_{SRO}$ ,  $T_{REF}$ ) of the SRO and SiO<sub>2</sub> layers for PDS-1, PDS-2, and REF cells.  $T_{SRO}$  and  $T_{REF}$  represent the fraction of the incident optical power, which actually reach the solar cells.

The absorbance spectra  $A_{SRO}$  are shown in Fig.2.2c. Interference patterns are observed due to internal reflections at the SRO interfaces (SRO/air and SRO/silicon). We can see that the absorbance of the thick SRO layer is larger than that of the thin SRO layer. Moreover, by comparing the PL and absorbance spectra, we note that the SRO layers absorb mostly high energy photons and emit low energy photons due to the characteristic energy shift of Si-NCs between absorption and emission band. This is important for downshifting application since it demonstrates the lack of re-absorption in Si-NCs, as discussed in subsection 1.5.1.

Photoresponsivity, or spectral response, is defined as the ration of the current generated by solar cell ( $i_{ph}$ ) to the power incident ( $P_0$ ):

$$PR(\lambda) = \frac{i_{ph}(\lambda)}{P_0(\lambda)} \quad (2.1)$$

This parameter is very important because it permits the extrapolation of the cell quantum efficiency. Fig.2.3 reports the wavelength dependence of the measured photoresponsivity (PR) of the three solar cells studied. The REF cell shows the largest photoresponse over the whole investigated wavelength range. This is due to the lower reflectance of the SiO<sub>2</sub> layer with respect to the PDS cells. On the other hand, PDS-1 and PDS-2 have PR spectra which reflect their optical transmission properties (see Fig.2.4).

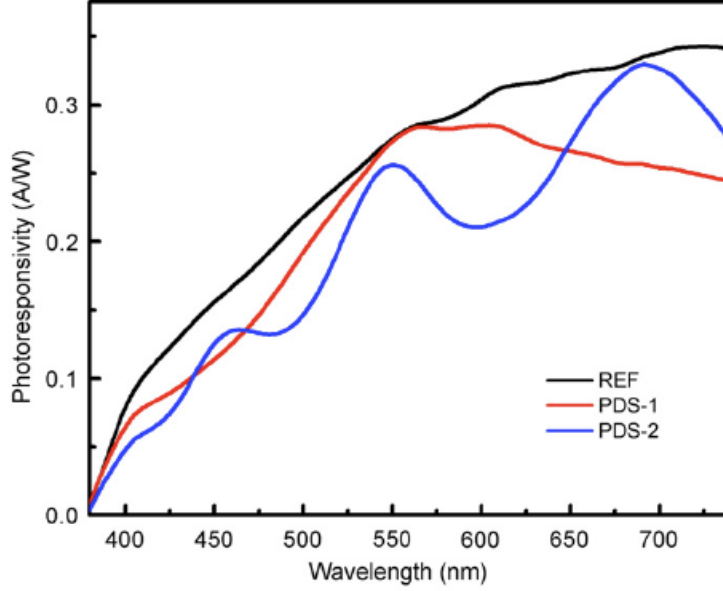


**Figure 2.3:** Photoresponsivities (PR) of the devices under study. The PR were measured by illuminating the cell with a monochromatized 1000 W Xe lamp and measuring the resulting photocurrent (from [86]).

In order to verify the role of the SRO as downshifting layer, we have separated the active contribution of the Si-NCs from their pure optical role, *i.e.* the role as anti-reflection-coating (ARC). To this aim, we identified with PR and  $PR_{REF}$  the measured photoresponsivity of the PDS and REF cell respectively. Then we defined the internal photoresponsivity as the normalization of the  $PR_{REF}$  with respect to the photons transmitted by the  $\text{SiO}_2$  ARC layer (Fig.2.1 bottom panel):

$$PR_{INT}(\lambda) = \frac{PR_{REF}(\lambda)}{T_{REF}(\lambda)} \quad (2.2)$$

This equation represents the photoresponse produced by only the silicon cell, without ARC contribution. In fact,

$$i_{ph}(\lambda) = PR_{INT}(\lambda) P_0(\lambda) T_{REF}(\lambda) \quad (2.3)$$

expresses the photocurrent produced in the silicon due to the photons transmitted by the  $\text{SiO}_2$  layer. Since the underlying silicon was the same for the REF as well as for the PDS cells, we could simulate the photoresponsivity produced by these cells

**Table 2.1:** Short-circuit current ( $I_{sc}$ ), open circuit voltage ( $V_{oc}$ ), filling factor (FF), and efficiency (eta) of the solar cell studied (from [86]).

Solar cell	$I_{sc}$ (mA)	$V_{oc}$ (V)	FF (%)	eta (%)
REF	4.38	0.61	80.6	15
PDS-1	2.97	0.57	80.2	9.5
PDS-2	3.01	0.57	80.6	9.9

when the SRO is not playing any active role, using the equation:

$$PR_{ARC} = PR_{INT} T_{SRO} = PR_{REF} \frac{T_{SRO}}{T_{REF}} \quad (2.4)$$

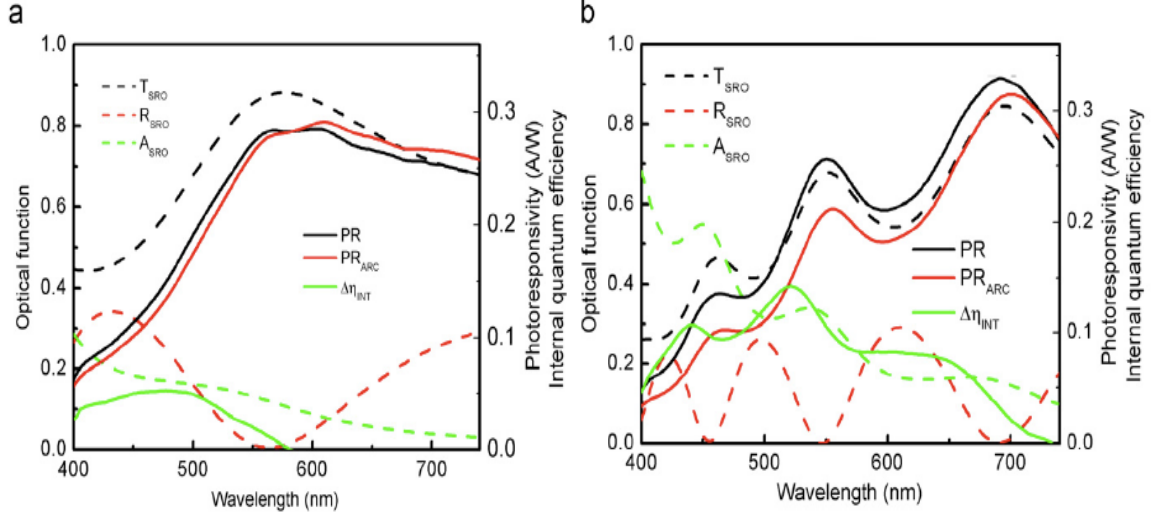
and, then, compare it with the measured PR that should be affected by the LDS effect. Indeed, if the SRO layer absorbs high energy photons and then emits low energy photons, an enhancement of the light-generated-carrier, and so of the photoresponsivity, is expected with respect to  $PR_{ARC}$ .

Fig.2.4 a and Fig.2.4 b show the results of this modeling for the PDS-1 and PDS-2, respectively. PR (black line) and  $PR_{ARC}$  (red line) differ mainly in the low wavelength region (400 nm - 600 nm), where SRO has a larger absorbance. In order to confirm our hypothesis on the role played by Si-NCs, we evaluated the difference in the internal quantum efficiency produced with (PR) and without ( $PR_{ARC}$ )

$$\Delta\eta_{INT}(\lambda) = \frac{hc}{q\lambda} \frac{PR(\lambda) - PR_{ARC}(\lambda)}{(1 - R_{SRO}(\lambda))} \quad (2.5)$$

where  $h$ ,  $c$ ,  $q$ ,  $\lambda$  are Planck's constant, speed of light in vacuum, the electric charge, and the wavelength, respectively.  $R_{SRO}$  represents the fraction of reflected photons by the SRO layer.  $\Delta\eta_{INT}$  is significantly larger for PDS-2 than for PDS-1. Integrating  $\Delta\eta_{INT}(\lambda)$  over the range of 380-740 nm, we found an enhancement of the IQE of 0.8% for PDS-1 and of 14% for PDS-2 due to the LDS effect. The large enhancement for PDS-2 is due to both a stronger absorption and emission from the thicker SRO layer.

Table.2.1 summarizes the performances of the three solar cells studied. These values were obtained by efficiency measurements performed using an ABET sun 2000 solar simulator class AAB following closely the procedure described in the international standard CEI IEC 60904-1. In order to calibrate our setup, irradiance measurements were performed using a packaged silicon reference 2 cm  $\times$  2 cm cell.



**Figure 2.4:** Optical function (transmittance, black dashed line, reflectance, red dashed line, absorbance, green dashed line), measured photoresponsivity (PR, black line), modeled photoresponsivity without emission from Si-NCs ( $PR_{ARC}$ , red line), and increment in the internal quantum efficiency ( $\Delta\eta_{INT}$ , green line) for PDS-1 (a) and PDS-2 (b) samples (from [86]).

The characteristic of this package cell under AM1.5G illumination are showed in Table.2.2. Moreover, the temperature of both PDS solar cells and reference cell was controlled to be  $(24\pm 1)$  °C during the measurements. IV curves were measured with a Semiconductor Source Measure Unit from Keithley Instruments Inc. using a 4 wire connection.

We found an energy conversion of 15%, 9.5%, 9.9% for REF, PDS-1, and PDS-2, respectively. The decreased energy conversion efficiency of the PDS devices is due to the increased reflectance, *i.e.* the thickness of the SRO layer must be optimized to find the best trade off between its optical and active properties. Indeed, the reference device is characterized by lower optical losses with respect to PDS cells: 10%, 21%, and 16% are the values of the integrated reflectance, over the range 350-1200 nm,

**Table 2.2:** Short-circuit current ( $I_{sc}$ ), open circuit voltage ( $V_{oc}$ ), filling factor (FF), and efficiency ( $\eta$ ) of the package cell, device code RR-61-O. This solar cell is produced at the Rabboud University Nijmegen (PV calibration facility).

	$I_{sc}$ (mA)	$V_{oc}$ (mV)	FF (%)	$\eta$ (%)
Calibrated Cell	83.4	598	77.5	9.7

evaluated for REF, PDS-1, and PDS-2, respectively.

## 2.2 LDS effect and optical properties

The study presented in the previous section demonstrates an enhancement of the PDS IQE with respect to the same cell without the active role of Si-NCs. However, the bad performances of these cells with respect to the reference, coated with only SiO<sub>2</sub>, have pointed out the necessity to optimize the SRO layer to reduce the optical losses and therefore increases the performances. In order to reach this aim, we developed an optical model based on transfer matrix of a luminescence downshifting (LDS) layer. To enhance the performances of a silicon solar cell, we propose using a SiO<sub>2</sub>/SRO double layer stack as anti-reflection-coating as well as LDS material.

### 2.2.1 Transfer matrix based simulations: optical losses optimization

The transfer matrix theory is a method to analyze the propagation of electromagnetic waves through a stratified (layered) medium [90–92]. Fig.2.5 illustrates a general multilayer stack and how an incident wave can propagate through it. We used this method to simulate the optical properties of a SiO<sub>2</sub>/SRO double layer stack to calculate its optimal thicknesses. The optimal values are then obtained by minimizing the reflection while maximizing the LDS effect, *i.e.* maximizing the photon flux which arrives on the underlying silicon due to the Si-NCs absorption and emission.

The reflectance, transmittance, and absorbance of a general multilayered thin dielectric film are calculated by the optical admittance,  $\mathcal{Y}$ , which is defined by

$$\mathcal{Y} = \frac{C}{B} \quad , \quad (2.6)$$

where  $B$  and  $C$  are the normalized electric and magnetic fields at the front surface, and are calculated by using the formula

$$\begin{aligned} \begin{bmatrix} E_0/E_m \\ H_0/E_m \end{bmatrix} &= \begin{bmatrix} B \\ C \end{bmatrix} = \\ &= \left\{ \prod_{r=1}^q \begin{bmatrix} \cos \delta_r & i \sin \delta_r / \eta_r \\ i \eta_r \sin \delta_r & \cos \delta_r \end{bmatrix} \right\} \begin{bmatrix} 1 \\ \eta_m \end{bmatrix} \end{aligned} \quad (2.7)$$

The suffix  $m$  denotes the substrate or emergent medium while

$$\delta_r = 2\pi N_r(\lambda) d_r \cos \theta_r / \lambda$$

is the optical effective thickness of the  $r$ -th layer, while  $N_r(\lambda) = n_r + ik_r$ .  $n_r$  and  $k_r$  are the real and the imaginary part of the refractive index respectively,  $d_r$  is the thickness, and  $\theta_r$  is the angle with which the photons enter the  $r$ -th layer (see Fig.2.5). The various angles  $\theta_r$  can be expressed as a function of the initial incidence angle using the generalized Snell's law [93].  $\eta_r$  is the optical admittance of the  $r$ -th layer and it is the only parameter that depends on the polarization as

$$\eta_r^{TE} = \mathcal{Y}_0 (n_r + ik_r) \cos \theta_r \quad , \quad (2.8)$$

$$\eta_r^{TM} = \mathcal{Y}_0 (n_r + ik_r) / \cos \theta_r \quad , \quad (2.9)$$

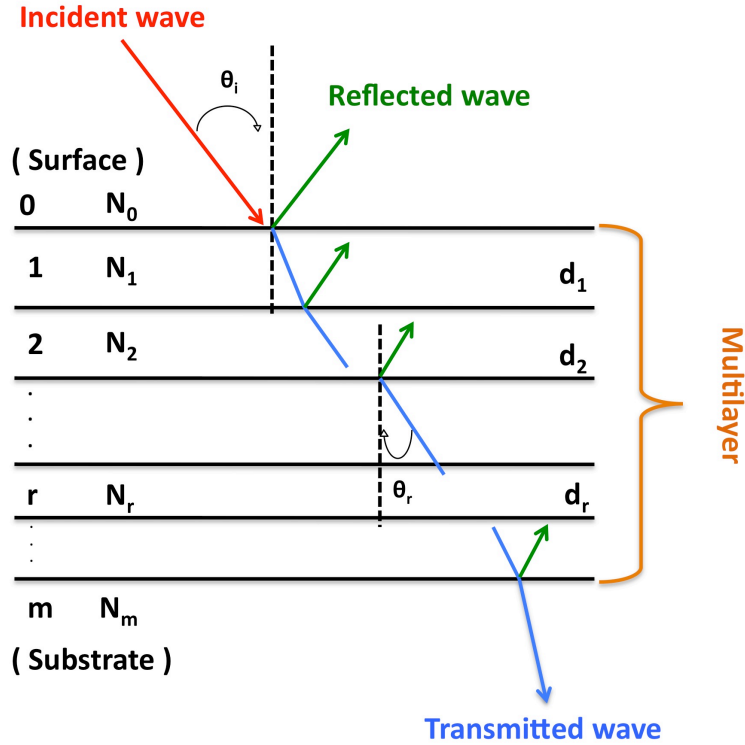


**Figure 2.5:** Propagation of an incident wave through a multilayer system.  $N_r$  and  $d_r$  are the refractive index and the thickness of the  $r$ -th layer.  $\theta_i$  and  $\theta_r$  represent the incident angle and the transmitted angle in the  $r$ -th layer. They are related by Snell's law.

where  $\mathcal{Y}_0 = \sqrt{\varepsilon_0/\mu_0}$  is the optical admittance of free space [90].  $\varepsilon_0$  and  $\mu_0$  indicate the vacuum permittivity and permeability, respectively. TE and TM stand for transverse electric and transverse magnetic polarized light. Equation (2.7) defines the characteristic matrix of a general structure and permits calculating its optical properties. The reflectance ( $R$ ), transmittance ( $T$ ), and absorbance ( $A$ ) are given by

$$R = \left( \frac{\eta_0 B - C}{\eta_0 B + C} \right) \left( \frac{\eta_0 B - C}{\eta_0 B + C} \right)^* , \quad (2.10)$$

$$T = \frac{4\eta_0 \operatorname{Re}(\eta_m)}{(\eta_0 B + C)(\eta_0 B + C)^*} , \quad (2.11)$$

$$A = \frac{4\eta_0 \operatorname{Re}(BC^* - \eta_m)}{(\eta_0 B + C)(\eta_0 B + C)^*} , \quad (2.12)$$

where  $\eta_0$  and  $\eta_m$  are the optical admittance of the incident material and of the substrate, respectively [90]. These equations take into account the multiple-reflections and the multiple-transmissions that occur at the interfaces of a general multilayer stack [90–92]. Moreover, this method considers absorption-media and also permits to evaluate  $R$ ,  $T$ , and  $A$  at different angles of incidence.

Since the LDS effect should increase the number of light-generated-carrier [94, 95], we used the short circuit current density ( $J_{sc}$ ) as optimization gauge.  $J_{sc}$  is calculated by the spectral responsivity ( $\mathcal{SR}$ ) and by the spectral irradiance of AM1.5G standard sunlight ( $\mathfrak{S}$ ) [96, 97], as follows

$$J_{sc} = \frac{I_{sc}}{\mathcal{A}} = \int_{\lambda_{in}}^{\lambda_{fin}} d\lambda \mathcal{SR}(\lambda) \mathfrak{S}(\lambda) , \quad (2.13)$$

where  $\mathcal{A}$  represents the area of the device while  $\mathcal{SR}$  is defined as

$$\begin{aligned} \mathcal{SR}(\lambda) &= \frac{q\lambda}{hc} EQE(\lambda) \\ &= \frac{q\lambda}{hc} IQE(\lambda)T_{si}(\lambda) , \end{aligned} \quad (2.14)$$

where  $q$  is the charge,  $h$  Planck's constant,  $c$  the speed of light in vacuum,  $EQE$  and  $IQE$  are the external and the internal quantum efficiency of the solar cell respectively, and  $T_{si}(\lambda)$  expresses the transmission coefficient of the double layer stack deposited on the “active” solar cells.  $T_{si}(\lambda)$  is the fraction of photons flux which reaches the active part of the cells. In presence of the LDS layer, the photon

flux arriving at the silicon is modified by Si-NCs absorption and emission. Therefore, equation (2.14) has to be modified to take the Si-NCs role into account as

$$\mathcal{SR}(\lambda) = \frac{q\lambda}{hc} [\mathcal{T}(\lambda) + \mathcal{T}_{PL}(\lambda)] \quad . \quad (2.15)$$

The first term

$$\mathcal{T}(\lambda) = T_{si}^{n.i.}(\lambda) IQE(\lambda) \quad , \quad (2.16)$$

describes the part of the normal incidence radiation (*n.i.*) that is not absorbed by the active material and, then, transformed in red shifted photons. This fraction of light is transmitted directly into the active silicon layer and generates photocurrent.

The second term

$$\begin{aligned} \mathcal{T}_{PL}(\lambda) = & QY \alpha(\lambda) \times \\ & \int_0^\pi \frac{d\phi}{\pi} \int_{\lambda_{in}}^{\lambda_{fin}} d\lambda' L(\lambda') T_{si}^{unp}(\lambda'; \phi) IQE(\lambda') \quad , \end{aligned} \quad (2.17)$$

expresses the Si-NCs emission. In more details:

- $QY$  is the luminescence quantum yield, or luminescence conversion efficiency. It represents the fraction of absorbed light that is emitted from Si-NCs. We can evaluate it by using the formula

$$QY = \frac{\Gamma_{LDOS}}{\Gamma_{nonLDOS} + \Gamma_{LDOS}} \quad ,$$

where  $\Gamma_{LDOS}$  and  $\Gamma_{nonLDOS}$  are the radiative and non radiative parts of the total decay rate of excitons in Si-NCs [84]. For further details on  $QY$  and its determination, see next section;

- $\alpha(\lambda)$  is the optical absorption of the active material calculated by equation (2.12). It depends strongly on the density of the active emitters and on the size of Si-NCs;
- $L(\lambda')$  is the experimental PL line-shape which is assumed to be a gaussian function:

$$L(\lambda') = \frac{e^{(\lambda' - \lambda_{peak})^2 / 2\sigma^2}}{\sigma\sqrt{2\pi}} \quad .$$

where  $\lambda_{peak} = 799$  nm is the PL peak wavelength while  $\sigma = 58$  nm is the PL linewidth.

- $T_{si}^{unp}(\lambda; \phi)$  describes the contribution to the transmitted light due to the isotropic and unpolarized photons emitted by Si-NCs and transmitted towards the active silicon layer:

$$T_{si}^{unp}(\lambda; \phi) = [\beta_{TE}T_{si}^{TE}(\lambda; \phi) + \beta_{TM}T_{si}^{TM}(\lambda; \phi)] \quad , \quad (2.18)$$

where  $T_{si}^{TE}(\lambda; \phi)$  and  $T_{si}^{TM}(\lambda; \phi)$  are the transmissions for a TE and TM polarization modes calculated using equations (2.8), (2.9), and (2.11) [90–92].  $\beta_{TE}$  and  $\beta_{TM}$  express the fraction of *TE* or *TM* polarized photons. We assumed unpolarized light, *i.e.*  $\beta_{TE} = \beta_{TM} = 0.5$ .

### 2.2.2 Luminescent quantum yield

In order to determine the luminescence quantum yield (QY), we studied changes in the photoluminescence decay rate of Si-NCs caused by the geometry of the sample. The idea of this experiment is the modification of the spontaneous emission rate of a dipole emitter due to the local density of optical states (LDOS)<sup>2</sup> [98–102]. In contrast to other methods commonly used to calculate the quantum yield through the ration of output to input power, this technique does not require the use of a reference sample or the estimation of excitation or collection efficiency [84]. The samples used consist of Si-NCs embedded in oxide layer of differing thicknesses on silicon substrate. The photoluminescence decay rate of Si-NCs varies with the modification of LDOS as the separation distance between the emitters and the silicon substrate is altered. The QY and the decay rates are found by comparing the magnitude of the decay rate modification to a calculation of LDOS. This approach allows an estimation of both the radiative and non-radiative decay components.

#### Method

Two samples have been fabricated by Dr.G. Pucker and Dr.Y. Jestin at the Advanced Photonics & Photovoltaics group, Fondazione Bruno Kessler (Trento - Italy). A photograph of these samples is shown in Fig.2.6. First, we deposited the maximum thickness of SiO<sub>2</sub> on silicon substrate, and, after an etching step, the different oxide layers are developed. Table2.3 reports the thickness values of the variable oxide layer measured with variable angle ellipsometry after the etching

---

<sup>2</sup>For further details see Chapter 4.

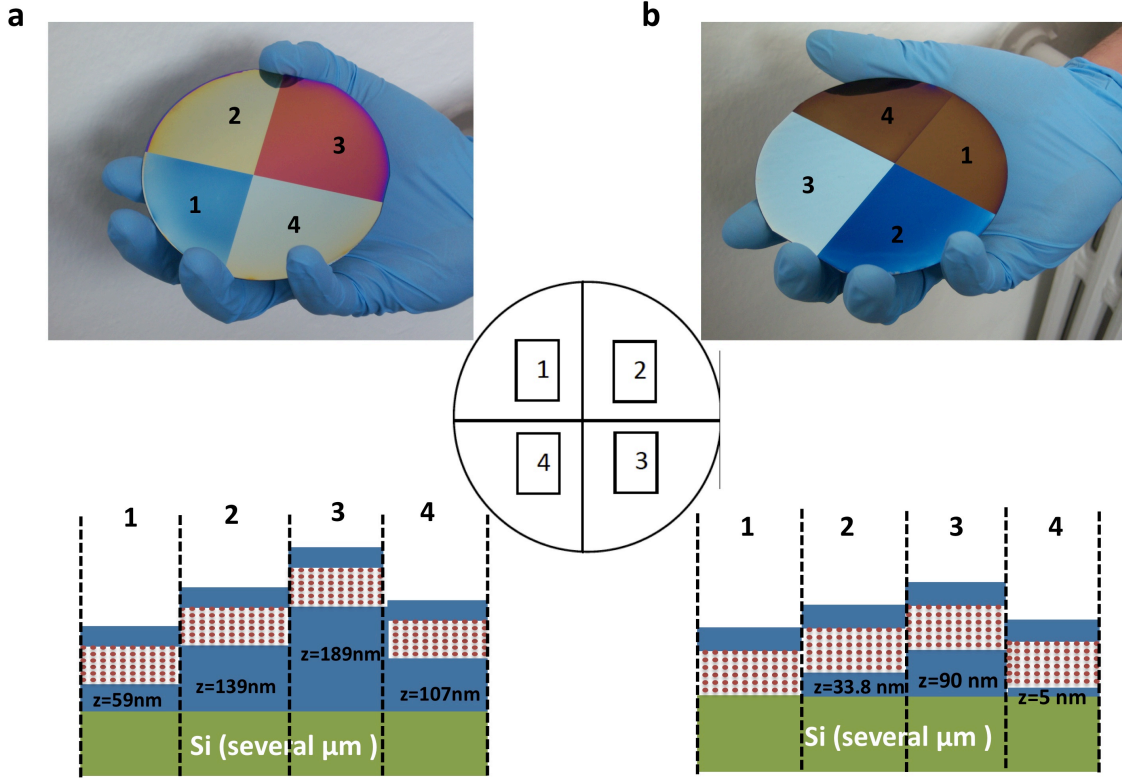


**Figure 2.6:** Top panel: photograph of the used samples. The different colours correspond to the oxide thickness variation that changes the environment of Si-NCs. Bottom panel: 2D cross-section of the devices (not in scale). Blue and green rectangles identify the SiO<sub>2</sub> layer and the silicon substrate (several  $\mu\text{m}$  thick) respectively. The cover oxide is 31 nm thick, while  $z$  gives the different oxide thicknesses after the etching step. The Si-NCs layer (61 nm thick) is represented by the red points. The numbers 1,2,3, and 4, identify the different environments.

**Table 2.3:** Oxide thickness measured with variable angle ellipsometry after the etching step.

Sample a				
Position	1	2	3	4
Oxide Thickness [nm]	$59\pm 2$	$139\pm 2$	$189\pm 2$	$107\pm 2$
Sample b				
Position	1	2	3	4
Oxide Thickness [nm]	$0\pm 2$	$33.8\pm 2$	$90\pm 2$	$5\pm 2$

step. We assumed an error of  $\pm 2$  nm in the data analysis due to the unevenness of the etching step. The active layers were produced by plasma enhanced chemical vapor deposition (PECVD). The ratio of gas flows between  $N_2O$  and  $SiH_4$  during the deposition process (deposition time 1 min) was 15. The two samples were annealed simultaneously in a tube furnace ( $1150$  °C ; 1 hour) in order to precipitate nanocrystals inside the silicon-rich-oxide layer. This activation process developed an SRO layer 61 nm thick covered by 31 nm of  $SiO_2$ .

PL spectra were measured at different positions along the sample at room temperature. The 355 nm line of a Nd:YVO<sub>4</sub> laser was used to excite the nanocrystals at normal incidence. To detect the PL signal, we used a monochromator and a visible GaAs photomultiplier tube (PMT). A photoluminescence map of data from both samples is shown in Fig.2.7. This plot shows a modulation of the PL emission as a function of the oxide thickness. This spectral variation can be attributed to interference effects at both excitation and emission wavelengths [103, 104]. In order to estimate the average dimensions of our emitters, we used the equation (1.4) assuming spherical shape. Results are shown in Fig.2.8 as a function of the oxide thickness. It is important to observe that the wavelength at which PL shows a peak is not influenced by interference effects but depends only on the particle dimension

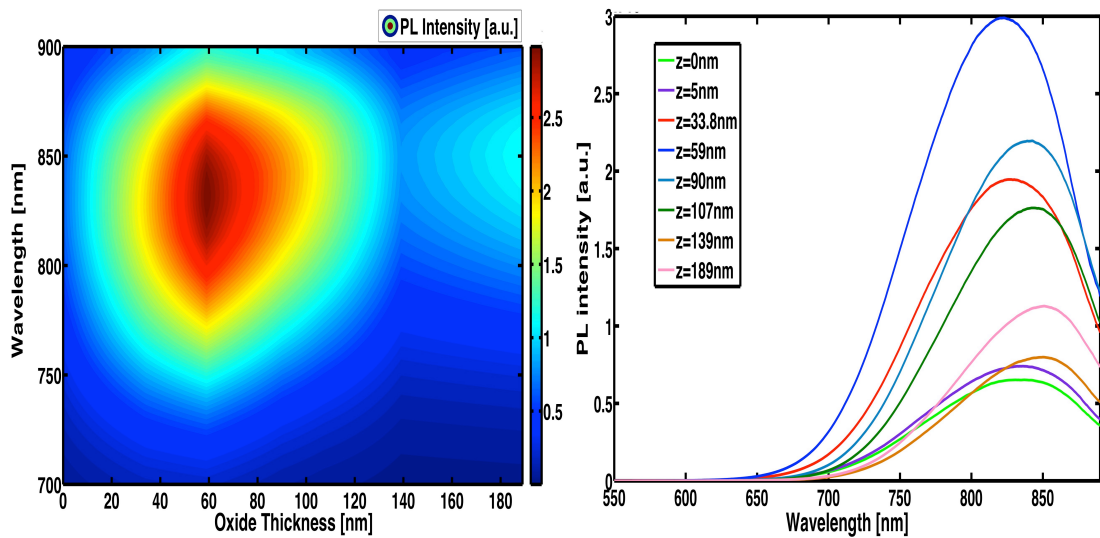


**Figure 2.7:** Right side: Experimental map of the variation in the emission intensity of Si-NCs as the oxide thickness below the nanocrystal ensemble changes. Left side: PL spectra intensity evaluated at the different positions along the both samples.

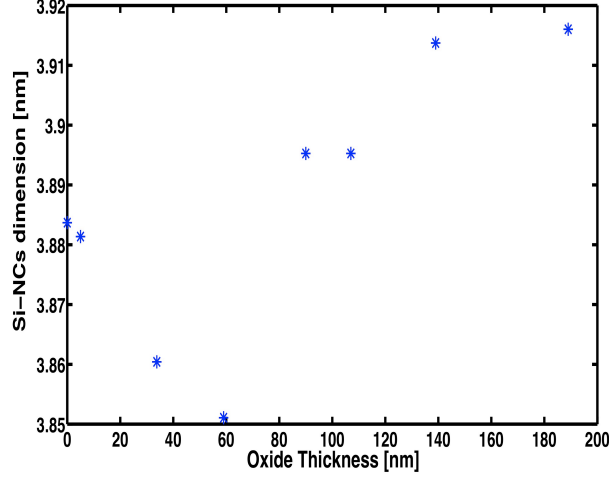


**Figure 2.8:** Average particle dimensions as a function of the oxide thickness evaluated using the equation (1.4) and assuming spherical shape.

due to the quantum confined effect. The size of our Si-NCs is around 3.9 nm, in agreement with other reported analysis (see Fig.1.3).

Time-resolved photoluminescence measurements were performed exciting the active emitters with two different sources: the 355 nm line of a Nd:YVO<sub>4</sub> laser and the 488 nm line of an Ar<sup>+</sup> laser. During the continuous wave PL measurements the laser beams passed through an attenuation filter to keep the power intensity constant at 90 mW. The PL decay time data were collected using a monochromator and a PMT. The thermoelectrically photomultiplier, with photon counting electronics, was used to collect time resolved data using a chopper to modulate the pump beams.

### Photoluminescence Decay Experiment

The decay of excitons in Si-NCs in a dense ensemble is commonly described by a stretched exponential or Kohlrausch decay of the form:

$$I(t) = I_0 e^{-(\Gamma_k t)^\beta} \quad (2.19)$$

where the photoluminescence intensity  $I(t)$  decays from an initial value  $I_0$ ,  $\Gamma_k = 1/\tau_k$  is the ensemble average  $1/e$  photoluminescence decay rate, and the dimensionless parameter  $\beta$  is an ideality factor that accounts for deviation from the single exponential decay curves ( $\beta = 1$ ) that would be expected for an isolated two-level

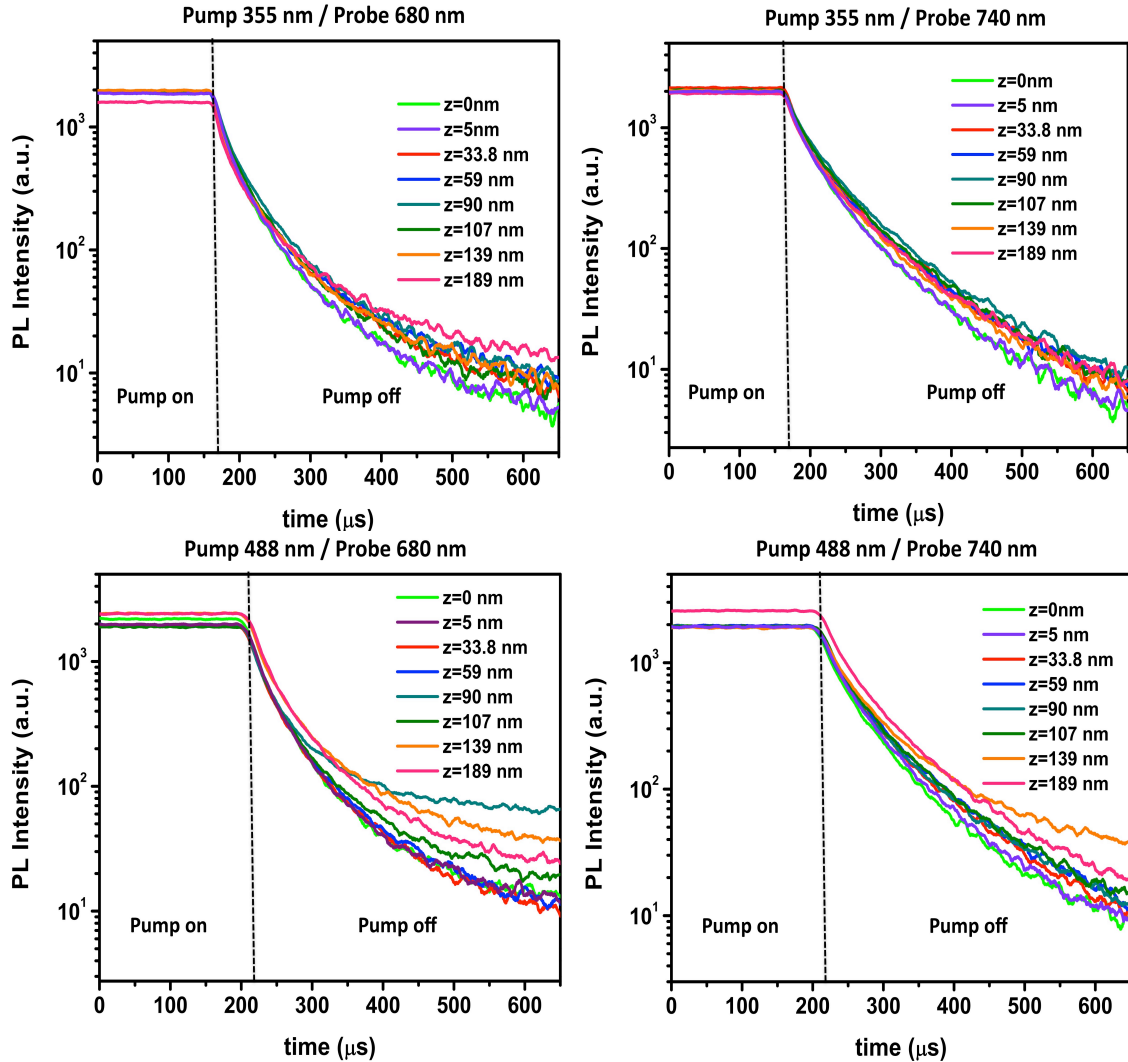


**Figure 2.9:** Time resolved photoluminescence measurements fitted using the equation (2.19). We used two different emission wavelengths (680 nm and 740 nm) changing the position of samples, *i.e.* changing the environments of the emitters. The excited populations of nanocrystals decay with a characteristic microsecond scale time.

optical system [105]. Therefore,  $\beta$  expresses the strength of the coupling between neighbouring Si-NCs.  $\beta$  is typically near 0.7 for dense ensemble [84]. All our data are well fitted using this value. This suggests that energy transfer between neighbouring nanocrystals contributes significantly to the observed decay rate produced by our samples.

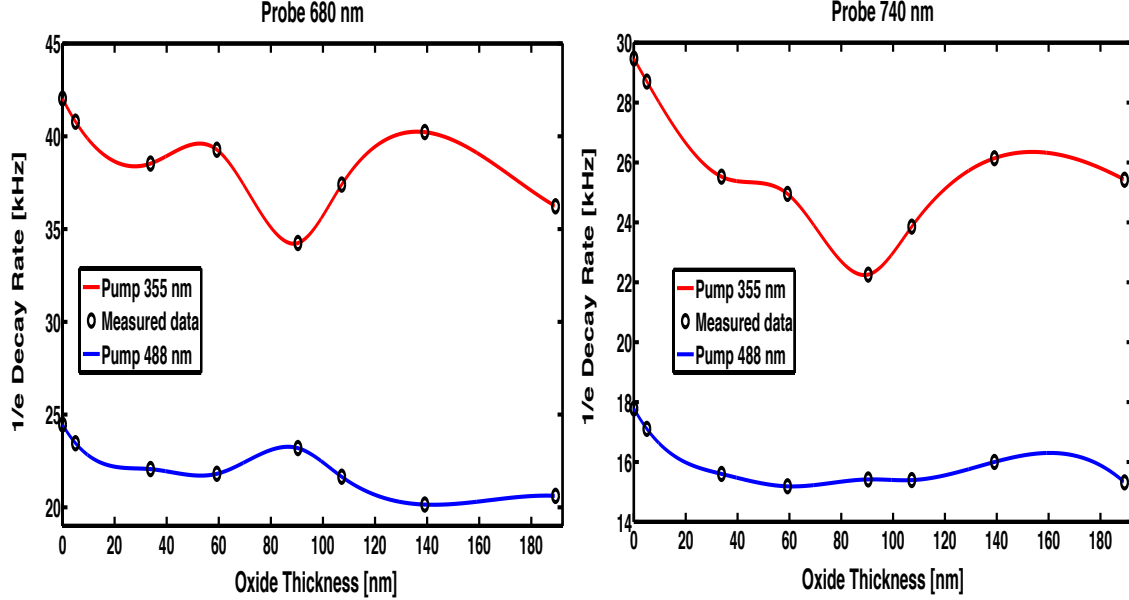


**Figure 2.10:** Variation of Kohlrusch  $1/e$  decay rate  $\Gamma_k$  as a function of the oxide thickness at an emission wavelength of 680 nm (left-side) and 740 nm (right-side). The black circles represent the decay rates obtained from fittings while the drawn lines are achieved performing a spline interpolation of these data. The red and blue line refer to an excitation wavelength of 355 nm and 488 nm respectively.

Fig.2.9 shows time resolved PL measurements fitted using the equation (2.19). The excited populations of nanocrystals decay with a characteristic microsecond time scale. From these analysis, we extracted the total decay rates that characterize these samples as a function of the oxide thickness.

Fig.2.10 displays  $\Gamma_k$  detected at 680 nm (left-side) and at 740 nm (right-side) using the two different excitation sources. The black circles refer to the measured data while the drawn lines are obtained performing a spline interpolation to show more clearly the oscillations of the total decay rates. These oscillations are related to the radiative part of  $\Gamma_k$  as  $\Gamma_{rad}$  is directly proportional to the LDOS (for further details see Chapter 4).  $1/e$  decay rate depends on both excitation and emission wavelength.

### Quantum Yield

Following the approach described in [84], the measured variation in the Kohlrausch decay rate  $\Gamma_k$  can be described using the equation:

$$\Gamma_k = \Gamma_{LDOS} \rho(\omega, z) + \Gamma_{nonLDOS} = \Gamma_{rad}(\omega, z) + \Gamma_{nonrad} \quad (2.20)$$

where  $\rho(\omega, z)$  is the local density of states at the position  $z$  of the nanocrystal ensemble, and  $\omega$  is the emission frequency. The decay rate component,  $\Gamma_{nonLDOS}$ , does not depend on the LDOS and may include energy transfer and non-radiative decay channels. It is independent on the oxide thickness, but is thought to depend on the passivation quality at the nanocrystal-to-oxide interface, while energy transfer processes likely depend on the average arrangement of nanocrystal ensemble [106]. Fermi Golden's rule relates the radiative recombination rate ( $\Gamma_{rad}$ ) with the local density of states:

$$\begin{aligned} \Gamma_{rad}(\omega, z) &= D_{ab}^2 \sum_n \langle 0 | \hat{E}^\dagger(z) | n \rangle \langle n | \hat{E}(z) | 0 \rangle \delta(\omega - \omega_n) \\ &= D_{ab}^2 \frac{\hbar\omega}{2} \rho(\omega, z) \end{aligned} \quad (2.21)$$

where  $D_{ab}^2 = 2\pi | \langle a | \hat{\mu} | b \rangle |^2 / \hbar^2$  is the oscillator strength for the transition, *i.e.* coupling between nanocrystal and radiation field (for more details, see section 4.2, and [84]). In order to evaluate the quantity  $\rho(\omega, z)$ , we used the model described in [107] based on the quantization of the radiation field according to

$$\hat{E}(z) = \sum_j \left[ i \frac{\hbar\omega_j}{2\epsilon(z)} a_j^\dagger \phi_j(z) + h.c. \right]$$

where  $a_j^\dagger$  is the creation operator of the mode  $|\phi_j(z)\rangle$  [84, 101, 102]. The calculation of  $\rho(\omega, z)$  sums a complete set of normalized plane waves at a single frequency for each polarization. The radiative mode functions  $\phi_j(z)$  contain both a propagation and a standing plane wave component dictated by Fresnel's coefficient of the interfaces. Moreover, this approach use an isotropic combination of dipole orientations since the PL is unpolarized and both the luminescence and measured decay are independent of the pump beam polarization. However, this formalism does not take into account the effects of absorption and homogeneous broadening. In Chapter 4, we will discuss a different approach, that contains these two effects, to estimate the

power radiated by an ensemble of Si-NCs placed in different environments. The equation (2.20) permits to evaluate the QY of our Si-NCs defined as

$$QY = \frac{\Gamma_{LDOS}}{\Gamma_{LDOS} + \Gamma_{nonLDOS}} \quad (2.22)$$

Indeed, using the simulated LDOS as a function of the oxide thickness, we could extrapolate  $\Gamma_{LDOS}$  (slope of the drawn lines) and  $\Gamma_{nonLDOS}$  (intercepts of the drawn lines) performing a least square fit to the linearized total decay rates (see Fig.2.11). The data are well fit by assuming a liner dependence on the total density of optical states, especially when we excite the active emitters with a wavelength of 488 nm

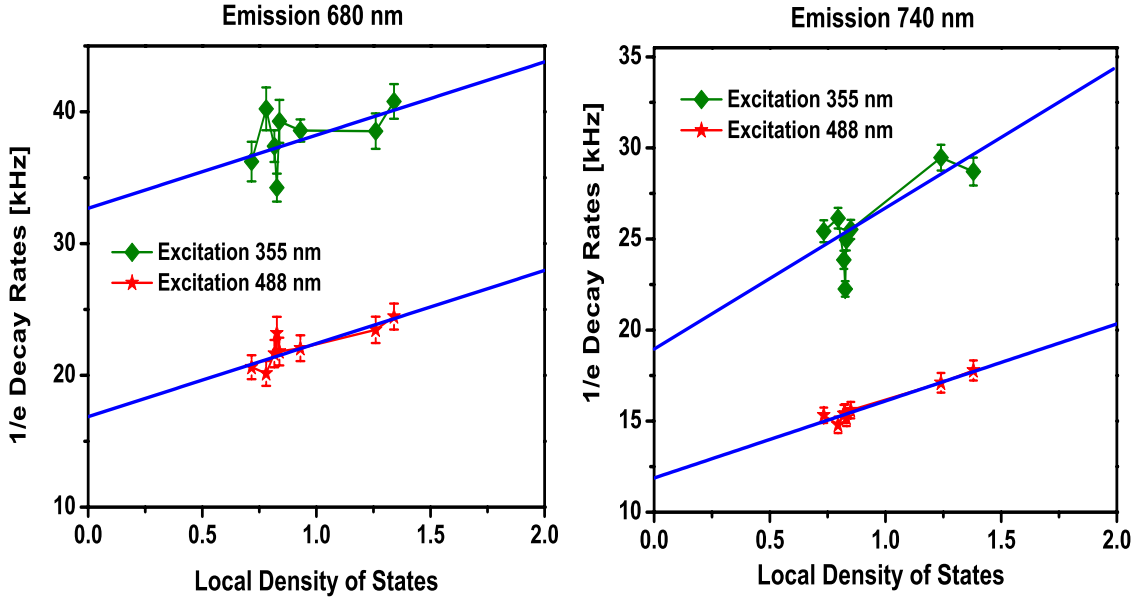


**Figure 2.11:**  $1/e$  decay rates as a function of the local density of states for different excitation and emission wavelengths: green and red lines refer to an excitation wavelength of 355 nm and 488 nm respectively. The drawn lines permit to extrapolate the values of  $\Gamma_{LDOS}$  (slops) and  $\Gamma_{nonLDOS}$  (intercepts).

**Table 2.4:** Quantum yield obtained using the equation (2.20) for different excitation and emission wavelengths.

Excitation wavelength [nm]	355	488	355	488
Emission wavelength [nm]	680	680	740	740
Quantum Yield [%]	$15 \pm 9$	$25 \pm 6$	$31 \pm 9$	$26 \pm 3$

(red stars). Moreover, excluding the case excitation/emission 355 nm/740 nm, the drawn lines shows a common slope corresponding to a  $\Gamma_{LDOS}$  of  $\sim 5 \pm 1.7$  kHz.

Table 2.4 shows the values of the quantum yield obtained. These values pertain only to the optically active fraction of nanocrystals in the ensemble that contributes to the photoluminescence signal.

We assumed a conservative value of 10% for the QY in the simulations. This value is lower with respect to the measured ones reported in Table 2.4. The problem here is the lack of complete dependence of QY from the wavelength. Moreover, these results show that QY depend also on the emission frequency, *i.e.* on the wavelength at which we collect the PL signal. Our assumption of only 10% seems reasonable considering that in the equation (2.17) QY is modulated by the optical absorption  $\alpha(\lambda)$  that is practically zero for wavelengths greater than  $\sim 500$  nm.

### 2.2.3 Optimization of the double layer stack

We applied the formalism of subsection 2.2.1 to a double-layer structure composed by a SiO<sub>2</sub> and of a SRO layer on a silicon substrate. Using the thicknesses and the refractive index ( $N(\lambda) = n(\lambda) + ik(\lambda)$ ) of air, SiO<sub>2</sub>, SRO, and silicon as input, we calculated the reflection in air, the absorption in the active layer and the transmission into the silicon substrate at normal and oblique incidence. The dielectric function and, hence, the refractive index, of the SRO layer, were measured with variable-angle ellipsometry [86]. The refractive indices of the other materials were taken from the database of the thin film modeling software Scout® [108]. Fig. 2.12 shows the imaginary ( $k$ ) and real ( $n$ ) of SiO<sub>2</sub> (blue) and SRO (red) as a function of the wavelength used in the simulations. The presence of an imaginary part of the SRO refractive index can be considered as an indication of the Si-NCs formation.

The optimization of the SiO<sub>2</sub>/SRO stack was carried out by finding the layer thicknesses that maximize the short circuit current density ( $J_{sc}$ ) of the solar cell. The starting point of this analysis is the cell internal quantum efficiency (IQE). We used the SILVACO software tools [60, 109] to simulate two different solar devices, called laboratory and commercial, with markedly different properties.

The first cell is a high efficiency laboratory cell realized on FZ p-type silicon substrate 300  $\mu\text{m}$  thick and with 1  $\Omega$  cm resistivity. The cell cross section is shown in the inset of Fig. 2.13. The phosphorous doping profile of the emitter and the Boron Back-Surface-Field (BSF) are optimized to minimize the surface recomb-

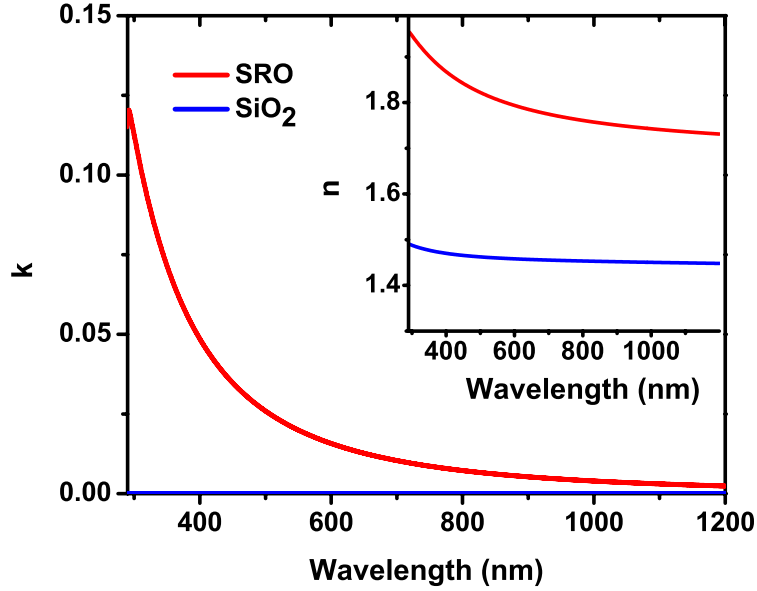


**Figure 2.12:** Imaginary ( $k$ ) and real ( $n$ ) part of the SiO<sub>2</sub> (blue) and SRO (red) refractive index. The refractive index of the SRO layer, containing Si-NCs, was measured with variable-angle ellipsometry.

nation velocity [110]. 10  $\mu\text{m}$  wide lines are opened in the passivating layer using photolithography and the metal fingers are deposited by sputtering. The second cell is a typical commercial silicon solar cell realized on CZ p-type silicon. The metal grid is deposited by screen printing with a typical width of 150  $\mu\text{m}$ . The phosphorous doping profile used here is standard for commercial solar cells [111]. The main characteristics of the cells are listed in Table 2.5. Fig.2.13 shows the simulated IQE. The two cells have very different IQE, in particular for wavelength lower than 500 nm.

We used these two IQE and equations (2.13) and (2.15) to calculate  $J_{sc}$  for different thickness values of SiO<sub>2</sub> and SRO. The thickness range investigated was 0 to 300 nm and 0 to 700 nm for SiO<sub>2</sub> and SRO, respectively. Fig.2.14 (a) and (b) show the short circuit current density ( $J_{sc}$ ) of both the laboratory and commercial solar cell as a function of the SRO thickness calculated using a  $QY = 10\%$  in the equation (2.17). The color lines refer to different thickness values of the SiO<sub>2</sub> layer.

The dependence of  $J_{sc}$  on the SRO and SiO<sub>2</sub> thicknesses is ruled by the double

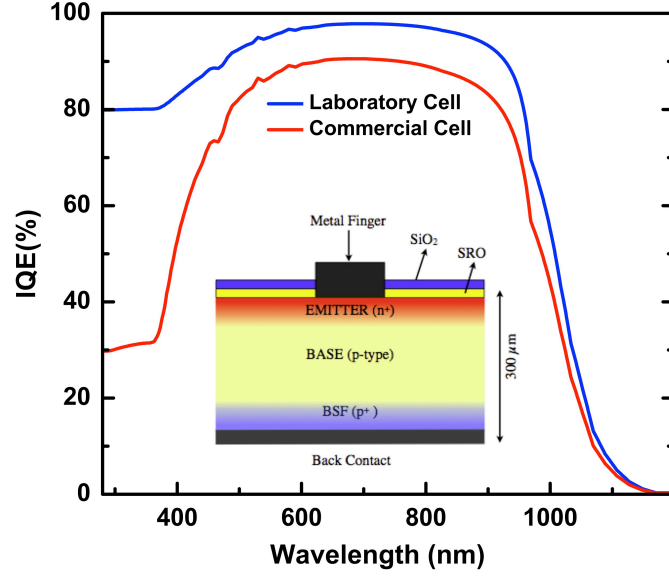


**Figure 2.13:** Simulated internal quantum efficiency of a laboratory and commercial solar cell. Inset: cross section of a  $n^+$ - $p$ - $p^+$  silicon solar cell with a  $\text{SiO}_2/\text{SRO}$  double layer stack coating (not in scale).

layer stack transmittance, the emission of the Si-NCs, and the IQE of the solar cell (equations (2.13) and (2.15)). For thin SRO layer, maxima are observed in  $J_{sc}$ , see Fig.2.14. For a given  $\text{SiO}_2$  thickness value, a different SRO value maximizes  $J_{sc}$  (Fig.2.15 (a)). In fact, interference effects, which depend both on the refractive index and thickness of each layer, account for the oscillatory behavior of  $J_{sc}$ . Different

**Table 2.5:** Main parameters of the laboratory (Lab. Cell) and of the commercial (Com. Cell) solar cell.

Parameters	Lab. Cell	Com. Cell
Substrate	FZ p-type Si (1 Ohm cm)	CZ p-type Si (1 Ohm cm)
Cell Thickness ( $\mu\text{m}$ )	300	300
Finger Pitch ( $\mu\text{m}$ )	400	2500
Finger Width ( $\mu\text{m}$ )	10	150
Front surface recombination velocity (cm/sec)	$10^4$	$4.5 \times 10^5$
Sheet Resistance ( $\Omega/\text{sq}$ )	120	50

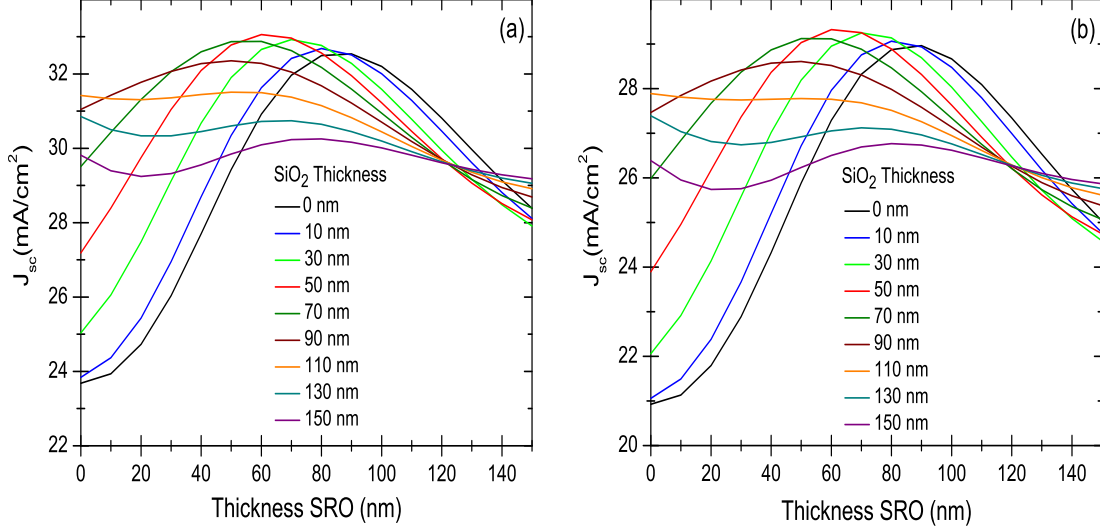


**Figure 2.14:** Short circuit current density as a function of the SiO<sub>2</sub> and SRO thickness of the laboratory (a) and commercial (b) solar cell (from [87]).

thickness combinations produce different phases between the wave reflected from the double layer stack top surface and the wave reflected from the SRO/Si interface. This thickness dependent effect explains the different thicknesses at which the short circuit current has a maximum in Fig.2.14. Moreover, Fig.2.14 shows that the presence of an active SRO layer increases  $J_{sc}$  with respect to the bare SiO<sub>2</sub> single layer. These results prove that a cell coated with a SiO<sub>2</sub>/SRO double layer stack shows better performances than a cell coated with a single SRO layer. The maximum  $J_{sc}$  obtained with a single SRO layer (black line) is lower than the one obtained with the double layer stack. Note also in Fig.2.15 (b) that the higher QY the thicker (thinner) is the SRO (SiO<sub>2</sub>) thickness.

The optimum stack parameters are summarized in Table 2.6. The difference between these optimized combinations is due to the different IQE of the laboratory

**Table 2.6:** Optimized thickness values of the laboratory and commercial solar cell for a QY=10%.

	SiO <sub>2</sub> Thickness (nm)	SRO Thickness (nm)
Laboratory Cell	51 ± 0.5	62 ± 0.5
Commercial Cell	48 ± 0.5	64 ± 0.5

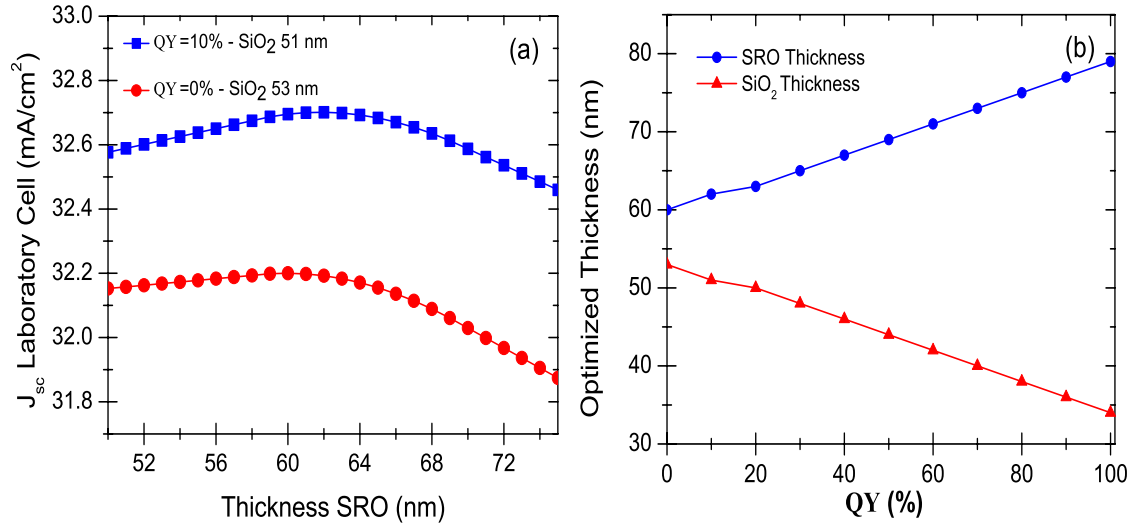


**Figure 2.15:** (a)  $J_{sc}$  of the laboratory cell as a function of the SRO thickness for two SiO<sub>2</sub> thicknesses with (blue curve) and without (red curve) the LDS effect. (b) Optimized thickness combinations that maximize the  $J_{sc}$  of the laboratory solar cell as a function of the conversion efficiency of the Si-NCs. (from [87]).

and the commercial solar cells (see Fig.2.13). In fact, the IQE enters into the thickness optimization of  $J_{sc}$  via equations (2.16) and (2.17). It is found that the two thickness combinations differ only by few nanometers. This means that the double layer stack works as a good ARC independently of the IQE of the specific solar cells. On the other hand, the LDS effect is critically dependent on the IQE which must be considered in the optimization simulations.

### Effect of LDS on the energy conversion efficiency.

To further investigate the energy conversion efficiency enhancement, we studied three different implementations of the cells: (1) the laboratory and the commercial cell with the optimum layer stack (named ACTIVE cell); (2) the cells with the optimum layer stack where QY=0 (named PASSIVE cell); and (3) a reference cell coated with an ARC layer formed by a 107nm thick SiO<sub>2</sub> layer (named REF cell). This SiO<sub>2</sub> thickness maximizes  $J_{sc}$ . The PASSIVE cell is used to single out the role of the Si-NCs emission from the combined ARC action of the double stack structure. Therefore, these three different implementations allow demonstrating the

performances improvement of the ACTIVE cell with respect to the others. Note that the three cells have the same IQE.

Fig.2.16 (a) and (b) show  $\mathcal{SR}$  of the various cells. This parameter allows the detection of the LDS effect. An increase in the short wavelength range of the  $\mathcal{SR}$  is expected for a cell formed by a Si-NCs active layer. The amount of this enhancement depends on the cell IQE. In more details, the LDS effect is more efficient in a cell with a low blue-IQE and a high red-IQE behavior. The ratio between them, determines the increase of the solar cell efficiency due to the LDS effect. An effective increase of  $\mathcal{SR}$  is observed for the short wavelengths. The laboratory and commercial cell show a relative enhancement of 6.5% and 10.6%, respectively. This enhancement was computed comparing the integral of the spectral responsivity for the ACTIVE and PASSIVE cells over the wavelength range 280 – 450 nm, *i.e.* where Si-NCs absorb. The enhancement due to the LDS effect is higher in the commercial cell with respect to the laboratory cell, because the commercial solar cell has a lower IQE in the UV-blue region than the laboratory IQE and a similar IQE in the red [112]. However, the best parameters of the laboratory cell produce a higher laboratory  $\mathcal{SR}$  with respect to the commercial cell (see Table.2.5).

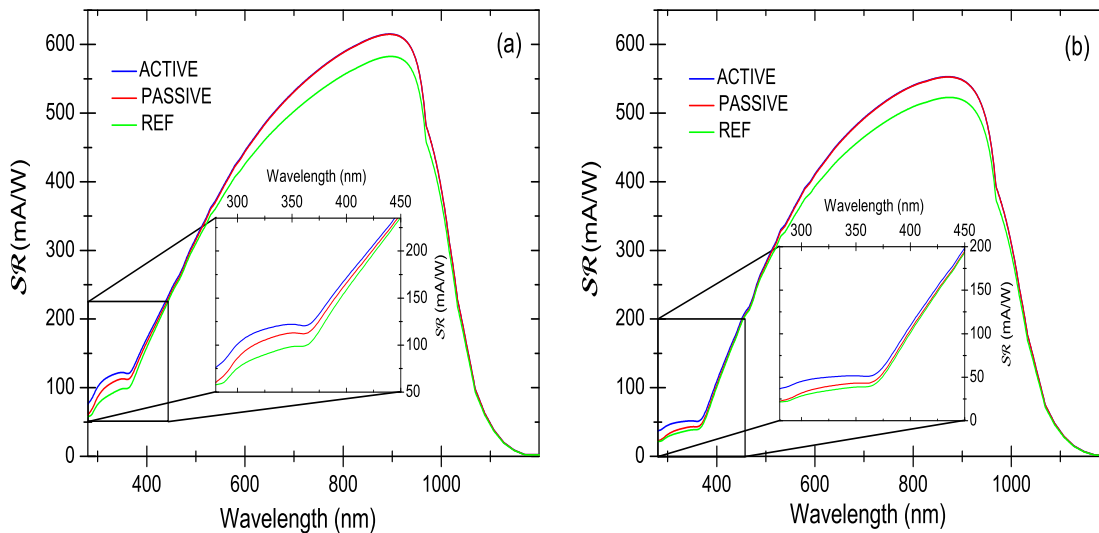


**Figure 2.16:** Spectral Responsivity of the laboratory (a) and commercial (b) solar cells. The green, red and blue curves refer to the REF, PASSIVE and ACTIVE cells. The inset is a zoom in the short wavelength region (from [87]).

Using the AM1.5G solar spectrum to illuminate the solar cell, the electrical parameters can be simulated. Fig.2.17 shows the modified solar spectra that reach the silicon for the REF (green curve), PASSIVE (red curve) and ACTIVE (blue curve) cells. Interestingly, more light reaches silicon when the double stack structure is used. In addition, considering the Si-NCs emission, a further increase is observed at about 750 nm. This is a direct evidence of the down-shifter effect in Si-NCs: photons absorbed in the blue are re-emitted in the red.

Fig.2.18 shows the IV characteristics of the laboratory (a) and commercial (b) solar cells under AM1.5G illumination, respectively. The open circuit voltage and the fill factor do not change due to the different cells since their electrical properties are unaffected by the coating layer [94]. Yet, we obtained an overall enhancement in the energy conversion efficiency from 16.50% to 17.56% between the REF and ACTIVE laboratory cells and from 14.20% to 15.11% between the REF and ACTIVE commercial cells due to the increased short-circuit current density. These values correspond to a relative improvement of 6.44% and 6.36% for the laboratory and commercial cells. Comparing the ACTIVE and PASSIVE cells it is possible to single out the contribution of the down-shifter effect to these values. We find 1.47% for the laboratory and 1.52% for the commercial cell. These enhancements are related to the increase of the  $J_{sc}$ . Moreover, the values of  $J_{sc}$  reported in the Fig.2.18,

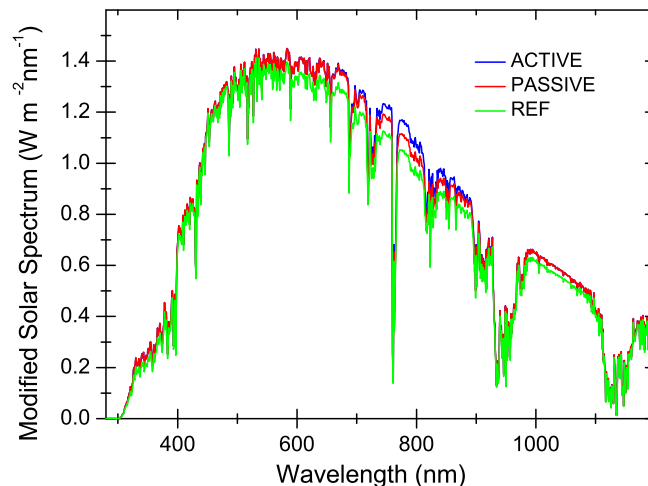


**Figure 2.17:** Modified solar spectra for the REF (green curve), PASSIVE (red curve) and ACTIVE (blue curve) laboratory cells, respectively (from [87]).

obtained using the Silvaco software tool, are practically the same achieved using the optimization code for the optimal thickness reported in Table.2.6 (see Fig.2.14).

To further investigate the Si-NCs contribution in the energy conversion efficiency, we changed the fraction of shifted photons, *i.e.* QY. As shown in Fig.2.19, the relative enhancement due to the down-shifter effect increases linearly with respect to QY. The energy conversion efficiency of the laboratory cell increase from about 17% to approximatively 20% .

Previous modelling studies have shown an increase of approximatively 10% in the energy conversion efficiency due to the LDS effect [113,114]. On top of the fact that these studies have been done for CdSe nanocrystals and fluorescent dye coating, there are other important differences to the present study. In [113] the energy conversion efficiency is evaluated using the integral of the modified solar spectra as the input power. This method produces a smaller spectral density than  $0.1 \text{ W/cm}^2$ , the value we used, and therefore, overestimates the energy conversion

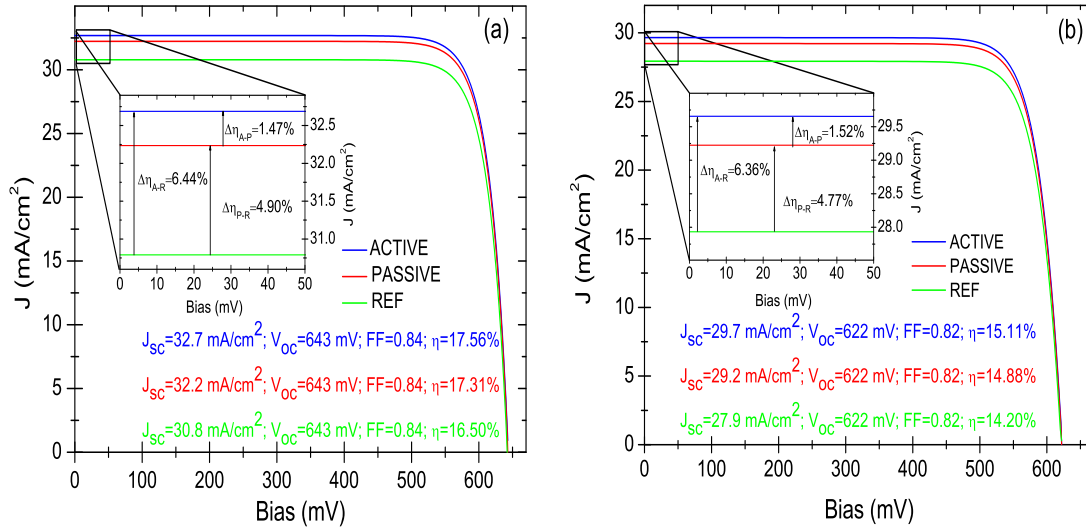


**Figure 2.18:** IV characteristics of the laboratory (a) and commercial (b) cells. The green, blue and red curve refer to the REF, PASSIVE and ACTIVE cells, respectively. The insets show the enhancement of  $J_{sc}$  due to the LDS effect.  $\Delta\eta_{A-P}$ ,  $\Delta\eta_{P-R}$  and  $\Delta\eta_{A-R}$  refer to the relative variations in the energy conversion efficiency between the ACTIVE-PASSIVE, PASSIVE-REF and ACTIVE-REF cells respectively. The differences between the laboratory and commercial solar cells are due to the difference in the optimized thickness combinations as well as to the different simulation parameters (see Table.2.5)(from [87]).

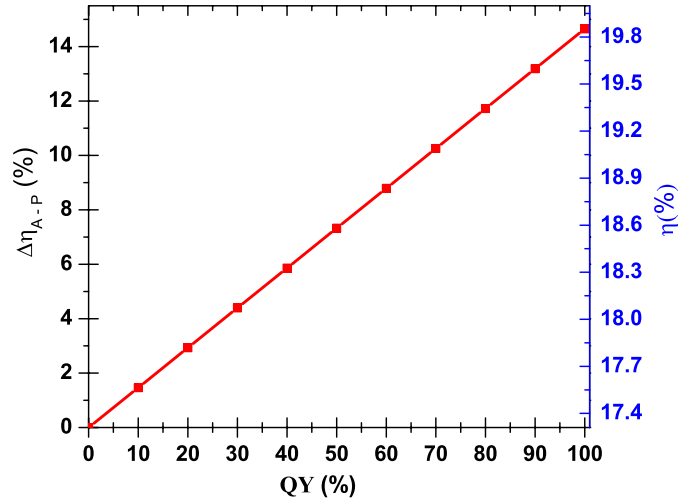


**Figure 2.19:** Relative enhancement in the energy conversion efficiency for the laboratory cell due to the down-shifter effect ( $\Delta\eta_{A-P}$ ) as a function of the QY, *i.e.* the fraction of shifted photons. The right axes expresses the total energy conversion efficiency ( $\eta$ ) for the laboratory cell (from [87]).

efficiency. Moreover,  $3/4$  of the emitted photons is assumed directed towards the underlying solar cell due to the internal reflection in the down-shifter layer independently from the wavelengths, whereas in our model we compute this ratio for each frequency and for each emission angle. The model presented in [114] is characterized by a conversion-collection factor evaluated as the product of the conversion efficiency with a collection probability factor. This quantity is assumed equal to the integral of the emissivity. In our model, we avoid these assumptions: the amount of emitted photons arriving in the substrate is calculated by the optical software itself (see equation (2.17)). Furthermore, in [113, 114], the authors assume a conversion efficiency of their CdSe nanocrystals and fluorescent dyes of about 80%. Our results shown a relative enhancement of  $\simeq 12\%$  for a QY=80% (see Fig.2.19 ).

## 2.3 Lima Project

The LIMA Project aims to develop novel structures increasing light-matter interactions in order to improve the efficiency of standard silicon solar cell. It proposes using nanostructured surface layers to increase light absorption in the solar cell while decreasing surface and interface recombination losses. The idea was to use metal

nanoparticles (plasmons) to enhance light absorption and internal scattering, and silicon quantum dots (Si-QDs) to modify the incident solar spectrum via downshifting.

This european project is composed of both academic and industrial partners which have strongly collaborated to reach project's goal.

In particular, our role, in collaboration with the Advanced Photonics & Photovoltaics group (AP&P-FBK-Trento-Italy), and the Institute Solar Energy (ISC) Research Center (Kostanz-Germany), was the study, characterization, and implementation of silicon nanoparticles. In more details, we have investigated a device designed to separate the carriers generation in the Si-QDs layer from the carriers collection in the junction region near the contacts, using an Interdigitated Back Contact (IBC) device configuration [3]. This has the additional obvious advantage of reducing shading losses and improving the light-matter interactions [115].

In this section, I will present the main results obtained during the three years of LIMA concerning the application of only silicon quantum dots.

### 2.3.1 Final integrated IBC device.

Many methods were subsequently developed for the synthesis of Si-NCs including the annealing of  $\text{SiO}_x$  powders followed by etching with HF [116], plasma synthesis [117], solution reduction of  $\text{SiCl}_4$  [118], and electrochemical dispersion of bulk silicon [119]. However, most Si-NCs fabrication methods are incompatible with the solar cell manufacturing process. In order to circumvent this problems, Pi X. *et all* [120,121] have used a new Si-NCs synthesis approaches (non thermal plasma) to produce freestanding Si-quantum dots [52], which are then dispersed in an organic solvent to form Si-QDs ink and then spin coated at the surface of Si solar cells. They showed an enhancement of almost 2% on  $I_{sc}$  after the inkjet printing of Si-QDs ink [121] demonstrating the key role of the LDS effect.

During the LIMA project several routes to fabricate IBC solar cells with Si-QDs have been investigated. In total three complete solar cell fabrication experiments were carried out. Each of these experiments resulted in an incremental improvement with respect to the previous one. This is a consequence of modifications/optimizations of the fabricated route indicated by the feedback/results from the previous ones. Two main fabrication ways have been identified to successfully integrate the novel layers in the final devices:

- integration of the novel layers during the fabrication of IBC solar cell devices,
- integration of the novel layers after the fabrication of IBC solar cell devices (for further details see Chapter 3).

Integration of novel layers during the fabrication process of the IBC solar cells has been the main focus throughout the LIMA project. In order to fabricate such complex solar cells, several optimization runs have been performed beforehand. The main problem concerning the incorporation of Si-QDs layer was the high thermal annealing step (typical 1100°C for 1 hour) necessary for the silicon nanocrystals formation. This additional thermal treatment is significantly higher than the typical diffusion temperature used to form the emitter or Back-Surface-Field (BSF)/Front-Surface-Field (FSF) region of IBC cells [115]. As a consequence, the whole IBC cell process will be damaged resulting in a lower solar cell performances. In order to overcome this fabrication drawback, we integrated the annealing between IBC cell process steps but after the formation of the FSF diffusion. Fig.2.20 (left-side) shows a process flow diagram of the best route found to integrate Si-QDs layers into the IBC cell process, while the right-side displays cross-section of the produced devices.

In order to have a direct quantification of the novel layer contribution to the cell performances, two prototype solar cells were developed :

- Prototype I cells are reference cells which received the same processes and temperature treatment but have a “dummy” SiN<sub>x</sub> (or SiN<sub>x</sub>/SiO<sub>2</sub>) layer(s) on the front side,
- Prototype II cells are devices where a SiO<sub>2</sub>/SRO (or SiN<sub>x</sub>/SiO<sub>2</sub>/SRO) layer stack are included on the front surface.

IBC cells, developed at the ISC center, are based on n-type (doping level  $3 \times 10^{14} \text{ cm}^{-3}$ ) high quality Float Zone (FZ) silicon substrate with 10-25  $\Omega \text{ cm}$  resistivity and a typical lifetime higher than 1 ms. The thickness of the wafer (200  $\mu\text{m}$ ) was chosen to guarantee a high collection efficiency of the minority carriers. The p<sup>+</sup> emitter is formed by a boron tribromide (BBr<sub>3</sub>) tube diffused of about 70  $\Omega/\text{square}$  while the BSF and FSF are formed by phosphorus oxychloride (POCl<sub>3</sub>) diffusion with 30 and 100  $\Omega/\text{square}$  sheet resistance, respectively. The cells are contacted using standard screen printing of a silver (Ag) (for BSF) and Ag/Al (for emitter) paste with a subsequent contact firing step. Thermal SiN<sub>x</sub> (or SiN<sub>x</sub>/SiO<sub>2</sub>) stake

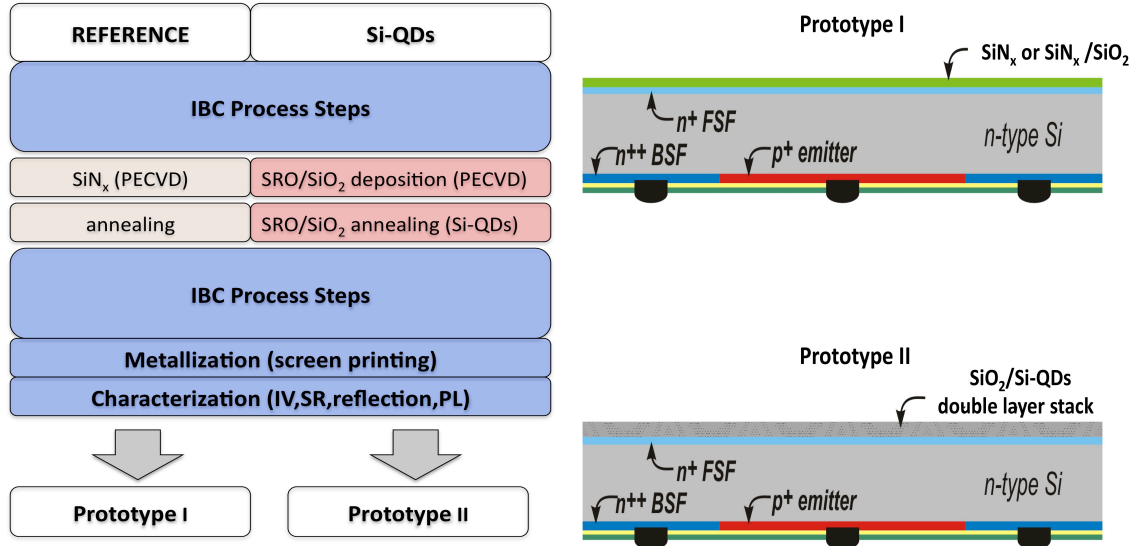


**Figure 2.20:** Left-side: Schematic process flow diagram used to integrate Si-QDs layers (Prototype II) during the fabrication process of IBC reference solar cells (Prototype I). Right-side: schematic cross-section of the produced device (not in scale) (from [115]).

layer(s) were used for the passivation of BSF and emitter regions on the back side. The front side  $\text{SiO}_2/\text{SRO}$  deposition method is described in the previous sections (for more details see also [122]).

### 2.3.2 Optimization

As pointed out in sections 2.1 and subsection 2.2.3, in order to develop a high performance solar cell with Si-QDs as active layer, the thickness optimization is a crucial step. In this way, the best trade off between active (LDS effect) and passive (optical losses) properties is carried out.

We applied the formalism described in section 2.2.3 to LIMA cells to find the optimal thickness of the  $\text{SiO}_2/\text{SRO}$  double layer stack. In order to perform this optimization, we used the measured internal quantum efficiency (IQE) (Fig.2.21 a) of a cell with Si-QDs (Prototype II) produced during the second run of the LIMA project. The IQE is, for definition, independent on the optical losses, *i.e.* independent on the anti-reflection-coating. Moreover, we used the refractive index (Fig.2.21 b) of a SRO ( $\Gamma_{12}$ ) layer deposited on a polished Si substrate. This “control” sample is necessary to measure the optical properties (dielectric function, and so,

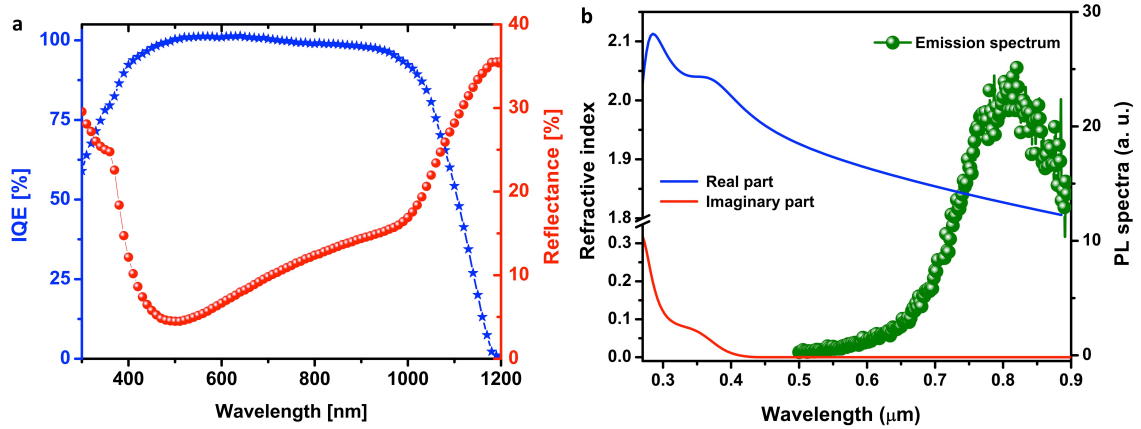


**Figure 2.21:** a) Measured IQE (blue) and Reflectance (red) of an IBC solar cell with a Si-QDs layer. b) Real (blue) and imaginary (red) part of a SRO layer deposited on polished Si substrate. This control sample is produced by using  $\Gamma_{12}$ . The green circles represent the PL spectra measured with the same methodology explained in the previous sections.

refractive index) of the Si-QDs embedded in a silicon dioxide matrix. We cannot determine the optical properties of the SRO layer performing direct measurements on the final device. It is important to observe that the refractive index of the SRO depends only on the fabrication prescription. In more details, it increases strongly

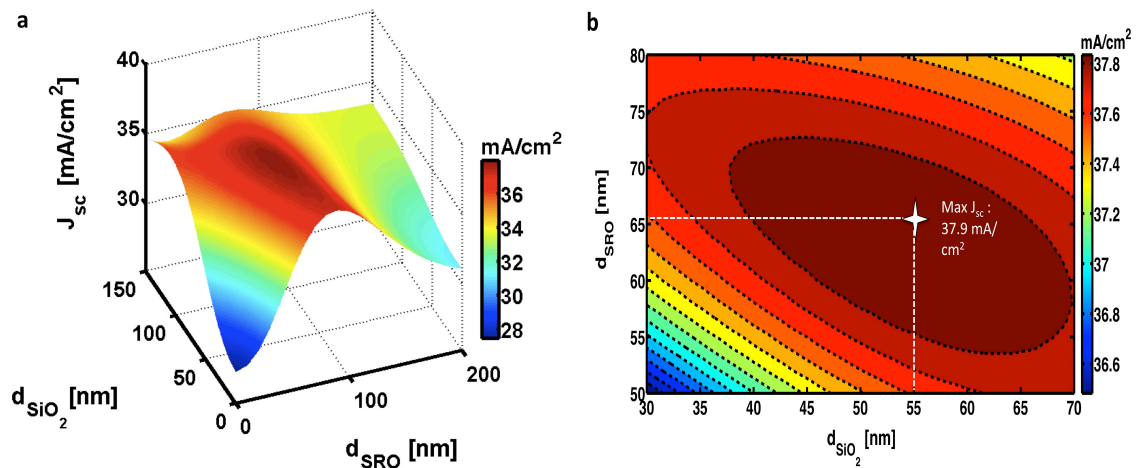


**Figure 2.22:** a) 3D plot of the simulated  $J_{sc}$  in mA/cm<sup>2</sup> as a function of the silicon dioxide and silicon rich oxide thicknesses. The color bar shows the values of the short circuit current density. b) Contour plot of this optimization in the optimal zone.

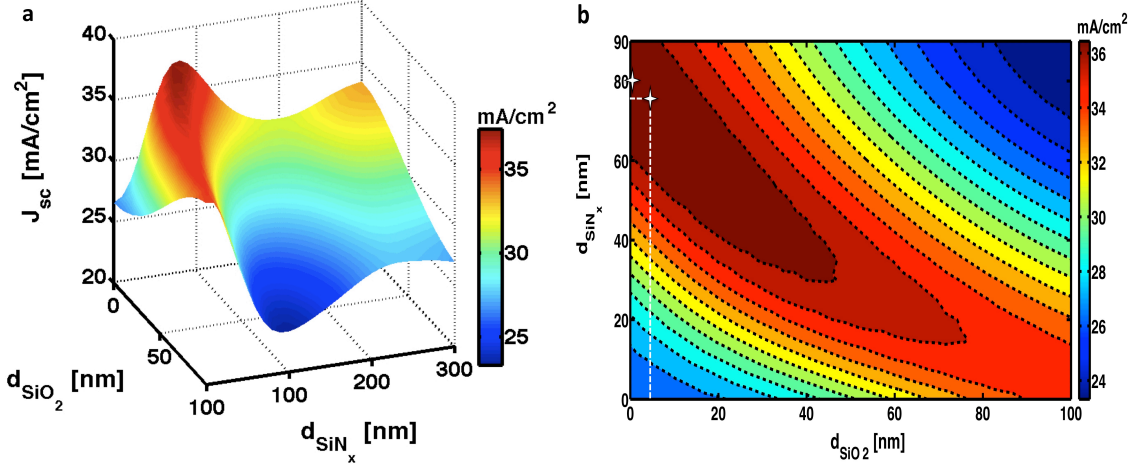


**Figure 2.23:** a): 3D plot of the simulated  $J_{sc}$  in  $\text{mA}/\text{cm}^2$  as a function of the silicon nitride and silicon dioxide thicknesses. The color bar shows the values of the short circuit current density. b): Contour plot in the optimal zone. The two markers refer to the thicknesses combinations that characterize the two LIMA reference cells (Prototype I) considered, as shown in Table.2.7.

during the thermal induced phase separation [122]. Therefore, the use of the same fabrication prescription assures the production of SRO layers with the same optical properties.

Fig.2.22 shows the results of our calculations. The 3D plot displays the variation of the short circuit current density as a function of the  $\text{SiO}_2$  and SRO thickness. The oscillatory behavior is produced by the thickness combination that maximize the transmission in the silicon substrate due to the mismatch between the refractive index of  $\text{SiO}_2$  and SRO, as explained in section 2.2.3. The maximum  $J_{sc}$  ( $\sim 37.9 \text{ mA}/\text{cm}^2$ ) is obtained for a double layer stack  $\text{SiO}_2/\text{SRO}$   $(55 \pm 2)\text{nm}/(65 \pm 2)\text{nm}$  thick (Fig.2.22 b). This thickness combination was used to fabricate IBC solar cells with Si-QDs as active layer<sup>3</sup>. Moreover, Fig.2.23 displays the optimization performed on the reference IBC devices (Prototype I):  $J_{sc}$  is maximized as a function of the  $\text{SiN}_x$  and  $\text{SiO}_2$  thickness.

<sup>3</sup>The error on the thickness was evaluated from the simulation step.

### 2.3.3 Results of integrated devices with Si-QDs as active layer

Two different configurations were chosen in the final integrated (Prototype II) and reference (Prototype I) device design to investigate the effect on the performances of different material/thickness combinations. The details of the different IBC solar cells are summarized in Table.2.7. The reported SRO 78 nm thick refers to the deposited thickness, *i.e.* before the annealing step. The total thickness  $d_{SRO}$  decreases during thermal annealing. This is mainly attributed to sintering of microvoids and loss of hydrogen [122]. Therefore, after this step the total SRO thickness is  $\sim (65 \pm 2)$  nm. In order to obtain a better passivation,  $(5 \pm 2)$  nm of PECVD silicon dioxide<sup>4</sup> was used in the G1B, G2A, and G2B IBC devices (see Table2.7). All these solar cells have a flat front surface.

Fig.2.24 shows the performances of the fabricated solar cells: short circuit current density (Fig.2.24 a), open circuit voltage (Fig.2.24 b), fill factor (Fig.2.24 c), and the efficiency (Fig.2.24 d). These measurements were performed at the ISC center, as well as at the Nanophotonics Technology Center Universidad Politécnic de Valencia (NTC-UPVLC), by using a class A solar simulator. The averaged short circuit current density is statistically higher for groups with Si-QDs (G2A and G2B) with up to 4%<sup>5</sup>. On the other hand, the open circuit voltage ( $V_{oc}$ ) does not show any

<sup>4</sup>The high annealing treatment (1100 °C) at which this passivation layer is subjected practically transforms it in a thermal silicon dioxide.

<sup>5</sup>Relative enhancement.

**Table 2.7:** Characteristics of anti-reflection-coating (ARC) layers used in the different final devices for both reference and Si-QDs IBC cells. The order of the materials, reported in the column “Material (Thickness)”, from the left to the right corresponds to the sequence “from the top to the bottom” on the IBC solar cells. The thicknesses used in the reference cells G1A and G1B are the optimal ones, as reported in Fig.2.23.

Sample	Prototype	Material (Thickness)
G1A	I	SiN <sub>x</sub> (80 nm)
G1B	I	SiN <sub>x</sub> (75 nm)/SiO <sub>2</sub> (5 nm)
G2A	II	SiO <sub>2</sub> (55 nm) /SRO (78 nm)/SiO <sub>2</sub> (5 nm)
G2B	II	SiN <sub>x</sub> (10 nm)/ SiO <sub>2</sub> (20 nm) /SRO (78 nm)/SiO <sub>2</sub> (5 nm)

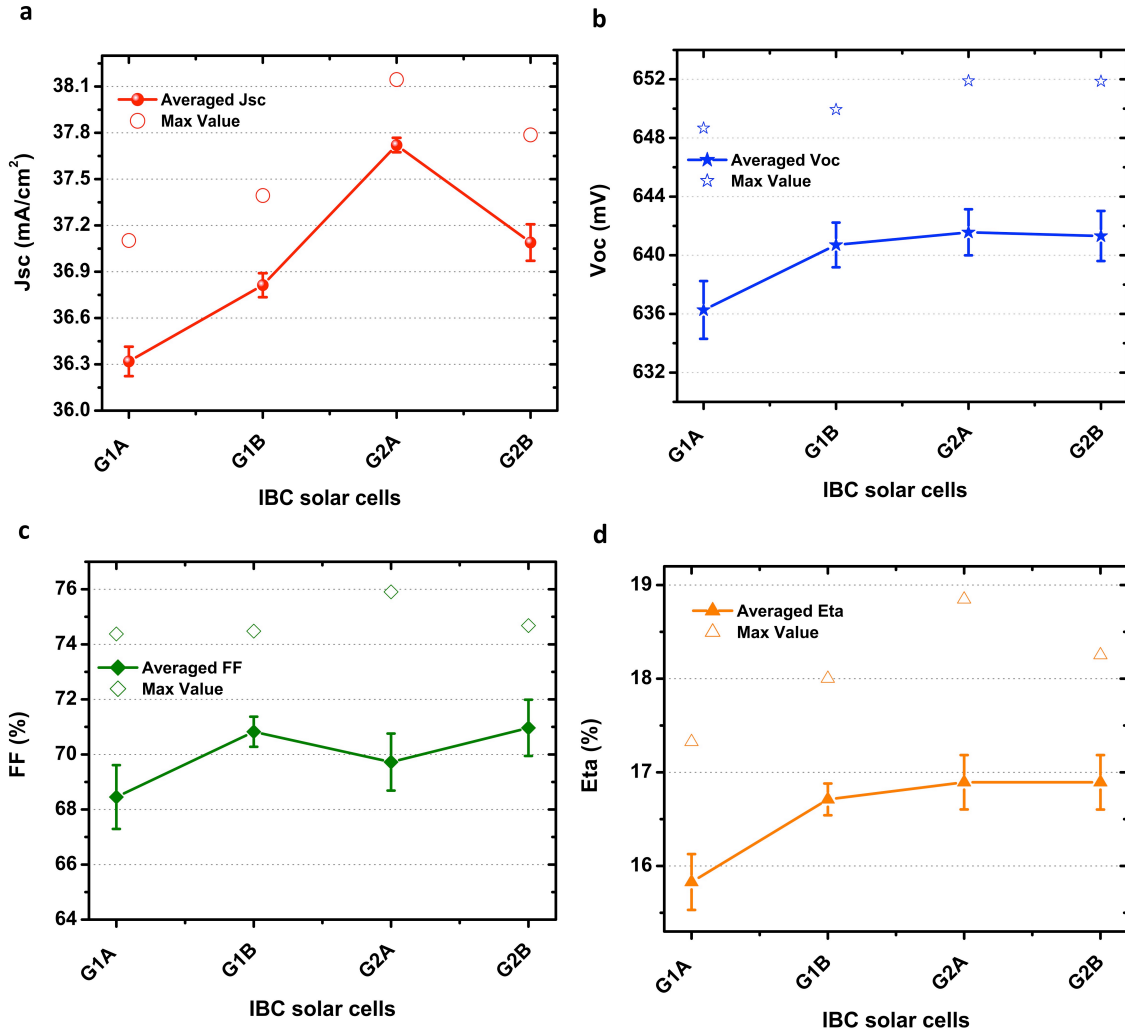


**Figure 2.24:** Short circuit current density (a), open circuit voltage (b), fill factor (c), and efficiency (d) of the reference (Prototype I) and Si-QDs (Prototype II) IBC cells. The statistics of each group are based on at least 26 solar cells. Max value refers to the best results obtained from each group of devices (see also Table.2.8).

**Table 2.8:** Best results obtained on integrated devices with (G2A) and without (G1B) Si-QDs.

Sample	Max $J_{sc}$ [mA/cm <sup>2</sup> ]	Max $V_{oc}$ [mV]	Max. FF [%]	Max. eta [%]
G1B	37.4	650	75	18
G2A	38.1	652	76	18.8

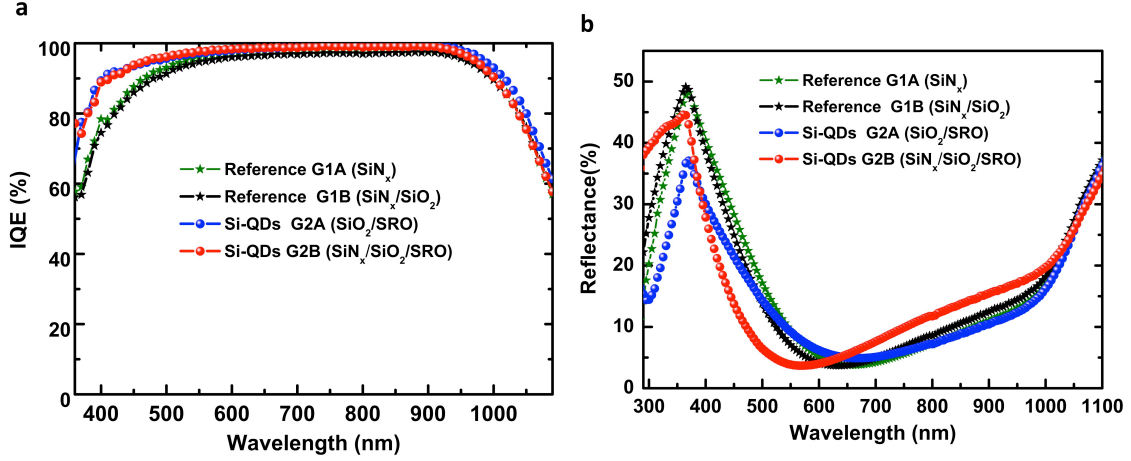
statistical variations on the number of cells measured for each group (more than 26 devices). Only, G1A shows a little decreasing, approximately 3 mV, with respect to the others. Also FF and Eta do not show any significant statistical variations. Although, G2A shows an enhancement in the short circuit current density with respect to G1B, its average efficiency is in the error bars of the G1B efficiency. This is due to the decrease of the fill factor (see Fig.2.24 c). Fig.2.24 shows also the best performances obtained from each group.

Table 2.8 displays the best results obtained on devices with and without Si-QDs. A measured cell efficiency of 18.8% was achieved with an IBC device characterized by an optimized SiO<sub>2</sub>/SRO double layer stack. This value is 4.44% (or 0.8% absolute) higher than the best reference cell fabricated in the LIMA project.

The substantial increase in the photocurrent using Si-QDs, as compared to reference cells, comes, in our opinion, from a combined effect of luminescent down-shifting (LDS) and an improved surface passivation of the silicon-rich-oxide layer. Fig.2.25 shows the IQE and reflection measurements of representative devices from each group. All cells with Si-QDs exhibit a better blue response with respect to references. Indeed, at short wavelengths Si-QDs absorb the incoming photons and reemit them at lower energies where the cell IQE is higher. As consequence, the IQE measurements reflect this behavior: better response at short wavelengths where less photons are lost due to recombinations. At the same time, the better chemical passivation on the front surface of the SRO layer results also in an enhanced blue response. It is not possible, at this stage, to attribute this short wavelength enhancement to LDS rather than to improved surface passivation.

G2A IBC devices, as well as G2B, show also a lower reflectance, more or less along all the investigated wavelength range, with respect to the reference cells G1A and G1B, as shown in Fig.2.25 b. The lowering of the reflectance indicates also a better optical role of the SiO<sub>2</sub>/SRO double layer stack with respect to the single SiN<sub>x</sub> ARC, as predicted from simulations. G2B (red points) has a higher reflectance in the UV-range, *i.e* where the Si-QDs absorb, with respect to G2A (blue points). This higher optical loss can explain the lower  $J_{sc}$  produced by G2B with respect to G2A (Fig.2.24). Moreover, this figure exhibits an enhancement of the reflectance in the infra-red region. This enhancement is produced by Fabry-Pérot interferences. Indeed, the parameter

$$F \sim \frac{4R}{(1-R)^2} = 1 + \frac{2F_r^2}{\pi} \quad (2.23)$$



**Figure 2.25:** Internal quantum efficiency (a) and Reflectance (b) of the reference (Prototype I) and Si-QDs (Prototype II) IBC cells.

, where  $R$  is the reflection and  $F_r = \Delta_{FSR}/\Delta_{FHWM}$  the finesse<sup>6</sup>, expresses the ratio between the maxima and minima of Fabry-Pérot fringes and it is called contrast factor [123]. Considering loss elements,  $F$  becomes

$$F = 1 + \frac{4}{\alpha_r^2 d^2} \quad (2.24)$$

where  $d$  expresses the Fabry-Pérot length while  $\alpha_r$  the loss coefficient. In our case, this parameter is the imaginary part of the silicon refractive index. Indeed, the contrast factor is practically one in the spectra range where the silicon absorb, *i.e.* no Fabry-Pérot fringes. On the contrary, in the infra-red region, where the silicon is practically transparent,  $F$  increases and therefore interference effects appear. Fig.2.26 illustrates this situation. The drawn lines represent simulated reflections, performed using the thin film Scout software [108], of the optical configuration of IBC G2A device changing the thickness of the silicon substrate. In particular, the red line is obtained using a silicon half-space as substrate, while the blue is achieved assuming the real value of the silicon wafer (200  $\mu\text{m}$ )<sup>7</sup>. Since the Free-Spectral-Range is inversely proportional to the Fabry-Pérot length, the red line does not show any

<sup>6</sup> $\Delta_{FSR}$  and  $\Delta_{FHWM}$  refer to the Free-Spectral-Range (spacing in optical frequency or wavelength between two successive reflected or transmitted optical intensity maxima or minima) and to the Full-Half-Width-Maximum.

<sup>7</sup>In this simulation, we used an air half-space on the bottom of the simulation shell.

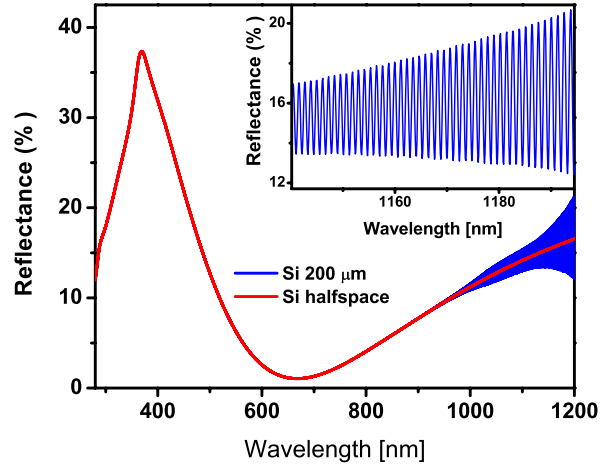


**Figure 2.26:** Simulated reflectance spectra of the G2A configuration. The difference between the drawn lines is in the silicon substrate thickness. The blue “line” appears only in the infra-red region because it perfectly matches the red for the other wavelengths. The inset shows the Fabry-Pérot fringes.

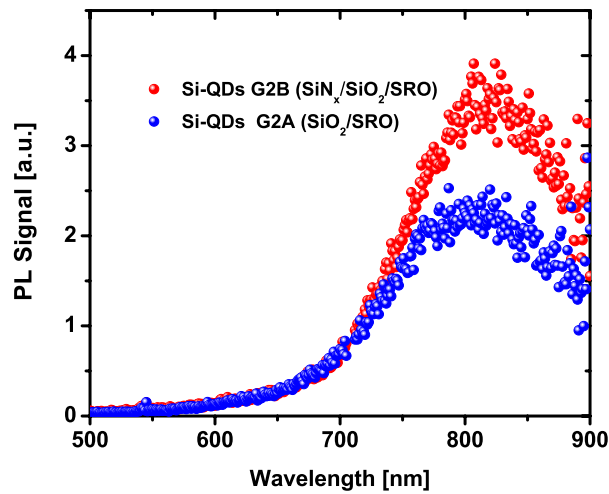


**Figure 2.27:** Photoluminescence (PL) signal of the Si-QDs as measured on the finished solar cells.

fringes because the finesse is zero (see equation (2.23)).

The starting point of our analysis on the separation between LDS and the passivation effect was to perform PL measurements on the finished cells to detect if we had or not emission. The IBC cells with the novel Si-QDs layer exhibited a

strong PL signal, as shown in Fig.2.27. Moreover, its intensity was similar to the one measured on control Si-QDs sample fabricated on a polished Si substrate. The reference cells did not display any signal since they do not have an active emitter layer. Fig.2.27 shows that the G2B configuration has a higher PL signal with respect to the G2A configuration, *i.e.* with respect to IBC solar cells that produce a higher  $J_{sc}$  (see Fig.2.24). First of all, in both devices the active layers are fabricated using the same prescription: PECVD deposition technique ( $\Gamma_{12}$ ), deposited thickness <sup>8</sup> 78 nm, annealing step 1100 °C for one hour. Therefore, the silicon-rich-oxide layers should possess the same “active” properties. Why PL measurements exhibit a different emission signal? One possible explanation could be the different optical composition of these devices (see Table.2.7), *i.e.* the different optical properties of these stacks can alter the absorption profiles and so the emission. In order to verify this hypothesis, we have simulated the absorption profiles ( $dA/dz$ ) through these structures changing the excitation wavelengths from 280 nm to 340 nm with a step of 20 nm. Fig.2.28 shows the results of this modeling<sup>9</sup>. In both configurations, the absorption takes place in the active layer (SRO) and exponentially decay in the silicon substrate, as expected. The G2A configuration exhibits a larger absorption

<sup>8</sup>Before the annealing treatment.

<sup>9</sup>We used the thin film Scout software [108] to perform these simulations.

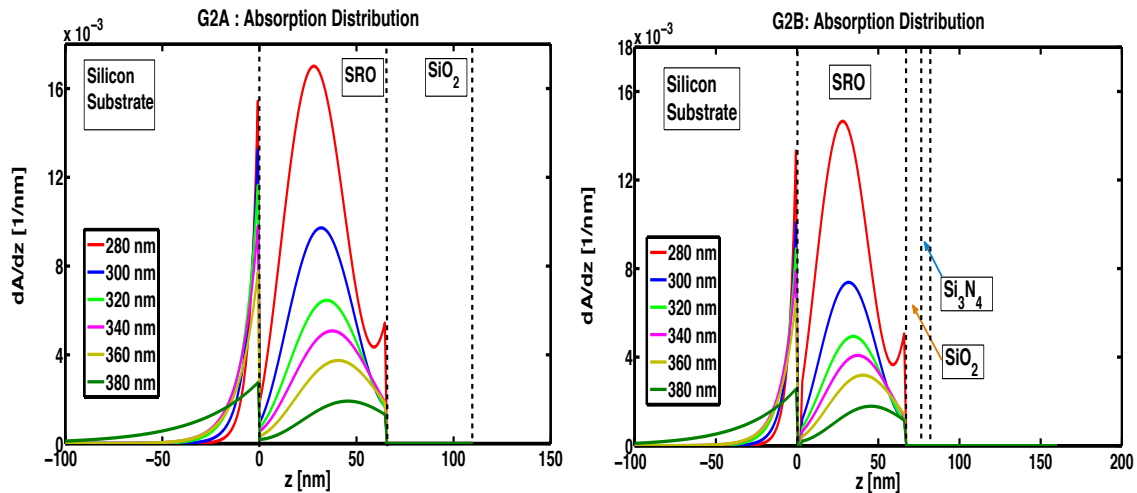


**Figure 2.28:** Absorption profile for different incident wavelengths (280 nm- 340 nm/step 20 nm) in the G2A (Left) and G2B (Right) configuration respectively.

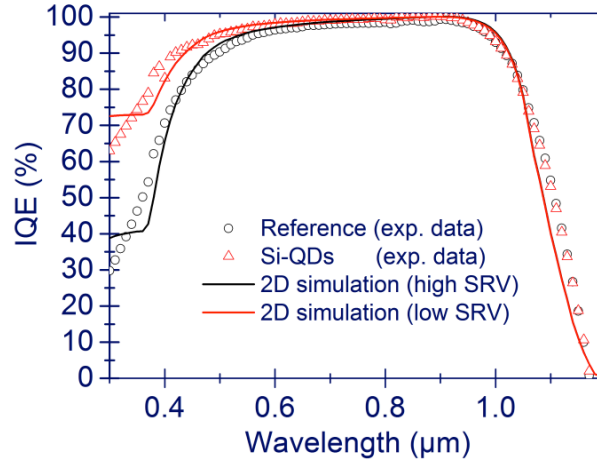


**Figure 2.29:** Comparison between simulated and measured IQE of the best IBC cell with and without Si-QDs. The drawn lines are obtained using two different surface recombination velocities (SRV):  $5 \times 10^5$  cm/sec for the reference (Prototype I) and  $5 \times 10^4$  cm/sec for the IBC cell with the novel layer (Prototype II).

distribution with respect to G2B for all the investigated excitation wavelengths. More absorption means more emission, and thus higher  $J_{sc}$ , as observed experimentally (Fig.2.24 a). At this stage, the larger G2B PL signal can be related to a higher emission towards the top (air) with respect to the bottom (silicon substrate) of this structure compared to the G2A configuration. In other words, the Si-QDs emission in the G2A configuration is directed more towards the silicon substrate producing a higher current with respect to G2B solar cell (for more details on this study see Chapter4 ). Moreover, this interpretation is reinforced by the fact that PL measurements, reported in Fig.2.27, are performed in back reflection.

In order to evaluate the contribution of the better surface passivation, our partners in Kostanz used the Silvaco software tool to compute the performances of IBC cells. The experimental data for doping profiles, device geometry, and material properties were used as input parameters to compare the simulated IQE with respect to the measured ones. The surface recombination velocity (SRV) is the only free parameter in these simulation. The best fittings were obtained using  $5 \times 10^5$  cm/sec and  $5 \times 10^4$  cm/sec for the reference and IBC-Si-QDs device respectively. As a consequence of this analysis, the IBC-Si-QDs solar cell which has a better surface passivation should have about 10 mV higher  $V_{oc}$  and about 3% higher  $J_{sc}$  than the

reference cell to explain alone the blue-IQE enhancement. As seen experimentally in Fig.2.24, none of these two conditions are clearly observable. However, their standard deviation is large (at least for  $V_{oc}$ ) to completely rule out this possibility.

Although the LDS and the surface passivation effects cannot be easily disentangled by integrating Si-QDs during the fabrication process of the cell, they are both part of the positive contribution in the use of this novel layer and of the project successful integration into IBC cell.

## 2.4 Conclusions

In this chapter, I have shown our efforts in order to fabricate an interdigitated back contact (IBC) silicon solar cell characterized by silicon quantum dots as active emitters. In the last years, the possibility to use semiconductor nano-structure in order to improve the performances of photovoltaic devices has been widely investigated. Here, the use of a double layer stack, formed by silicon dioxide and Si-QDs, has been optimized by means of transfer matrix simulations to find the best trade-off between passive (transmission, reflection, and absorption) and active (Si-QDs absorption and emission) properties. An additional optimization on the IBC fabrication process has been performed by our partners at ISC center to overcome the degradation of the cell properties due to the high annealing step necessary for the Si-QDs formation. With the most promising thickness combination (  $55\pm 2$  ) nm for  $\text{SiO}_2$  and  $(65\pm 2)$  nm for SRO), different IBC solar cells including Si-QDs have been produced within the european project LIMA. The resulting samples have shown good performances with respect to optimized IBC reference solar cells: an enhancement of 2.5% in the averaged short circuit current density is observed when using Si-QDs with respect to the best IBC reference, as shown in Fig.2.30. Moreover, a best cell efficiency of 18.8% was achieved. This value is 4.44% (or 0.8% absolute) higher than the best reference cell fabricated in the LIMA project.

A critical analysis of the observed results is also presented to determine the origins of the  $J_{sc}$  improvement. The enhancement of the internal quantum efficiency in the UV range, which causes the increase of the current, was attributed to a combination of LDS effect and an improved surface passivation of the silicon-rich-oxide. In order to separate these two contributions, studies based on PL measurements, as well as optical and electrical simulations have been performed. The results of

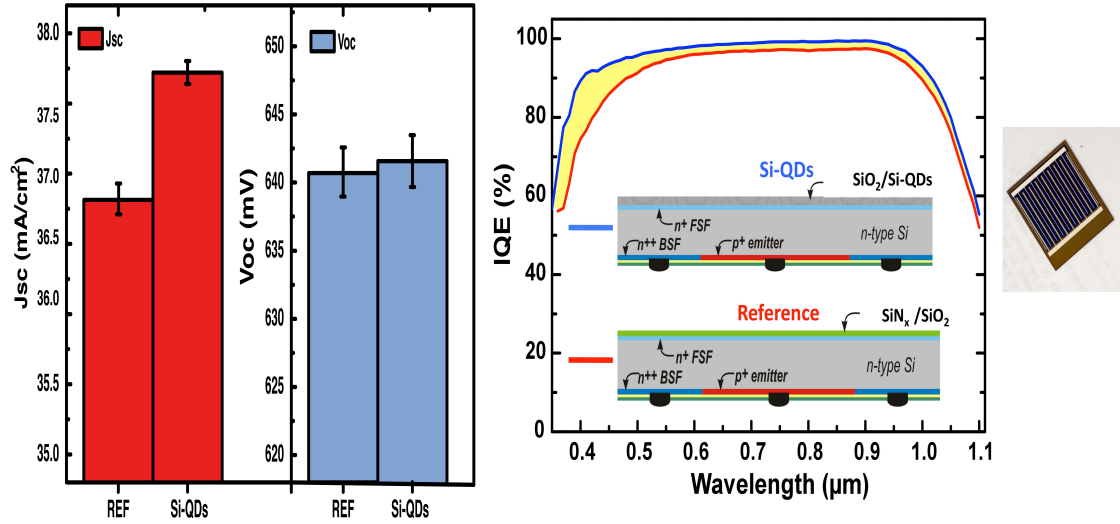


**Figure 2.30:** Left: experimental  $J_{sc}$  and  $V_{oc}$  produced by reference and Si-QDs solar cells. The error bars represent the standard deviation calculated on at least 26 devices for both REF and Si-QDs. Right: measured internal quantum efficiency enhancement of an interdigitated back contact solar cell with Si-QDs as active layer with respect to a reference device coated with a  $\text{SiN}_x/\text{SiO}_2$  double layer stack. A photo of the back side of the final IBC is also shown.

these investigations do not exclude a significant role played by the LDS effect in the improved performances. Therefore, although these two effects cannot be easily disentangled by integrating Si-QDs during the cell fabrication process, the LDS effect and the better surface passivation are both part of the positive contribution in the use of this novel layer and of its successfully integration into IBC cell.



---

## Chapter 3

# Detection of the LDS effect in Si-NCs

In Chapter 2, the improvement of the photocurrent (up to 4%) using Si-QDs as active layer in the IBC<sup>1</sup> devices was ascribed to a combined action between a better surface passivation and the LDS effect. However, we are not able to quantify the role of each one of these positive effects during the fabrication process of this integrated device.

In this chapter, I will report an alternative method to apply a down-shifter layer on IBC solar cells. The aim of this study is to separate the silicon nanocrystals (Si-NCs) layer from the cell. The IBC device is not affected by the Si-NCs formation during the fabrication process, *i.e.* the surface passivation quality of the cell remains unaffected after the application of the LDS layer. In this way, the downshifting contribution can be quantified separately from the passivation effect, as compared with the method presented in Chapter 2.

In section 3.1, I will describe this new approach based on the deposition of an optimal silicon rich oxide layer on a quartz substrate (500  $\mu\text{m}$  thick). This active layer is used as cell cover glass which is however not in contact with the cell. A sandwich is then realized between the IBC cells and the “active” cover glass. Different configurations have been studied by changing the medium between the cover/IBC spacing layer to “activate” the optical properties in the cell cover glass. Moreover, I will present also another method based on colloidal Si-NCs dispersed in

---

<sup>1</sup>Interdigitated Back Contact silicon solar cell.

a glycerol solution as “active liquids” located in the quartz-cover-glass/IBC spacing layer. The proposed approaches should be valid for any solar cell and it resembles the situation of a PV module where a glass cover is used to protect it from environmental influences.

### 3.1 Method Description

As pointed out in the conclusions of Chapter 2, the UV-enhancement of the internal quantum efficiency (IQE) of IBC devices based Si-QDs with respect to optimal reference cells, can be ascribed to a combination of LDS effect and a better surface passivation of the silicon-rich-oxide (SRO) layer. PL measurements on the integrated devices, as well as optical and electrical simulations were performed in order to understand and separate these two contributions. However, these preliminary analyses showed that both effects contribute to the improvement of the performances. The LDS and surface passivation effects cannot be easily disentangled integrating the Si-QDs layer into the IBC fabrication process.

In order to reach this aim, we propose an alternative method based on the integration of active layers after the production of IBC solar cell devices. In this way, we can separate the fabrication of silicon nanocrystals (Si-NCs) by the solar cell manufacture process. The strategy is to deposit the SRO layer not directly on the cell, as presented in section 2.3, but on a quartz substrate  $500 \mu\text{m}$  thick. Therefore, the high annealing treatment ( $\sim 1100 \text{ }^\circ\text{C}$ ) necessary for the silicon nanocrystals formation does not affect the IBC process and, thus, the surface passivation properties of the cell. This “active” cover is then used to encapsulate the IBC solar cell. We considered three different situations changing the medium in the cover/IBC spacing layer to “activate” the optical properties in the cell cover glass. We used as medium air, glycerol, and a refractive index matching liquid (RIML). Moreover, a cover glass composed by silicon rich oxide not annealed (SRO NA) deposited on a quartz substrate  $500 \mu\text{m}$  thick has also been studied to exclude possible improvement in the solar cell performances produced by a better Anti-Reflection-Coating (ARC). A schematic representation of the method used to integrate Si-NCs after the fabrication of the IBC solar cells is shown in Fig.3.1. The red flowchart illustrates the scheme described above and called Prototype Ia, while the green flowchart shows a different approach in which colloidal Si-NCs in a glycerol solution are used

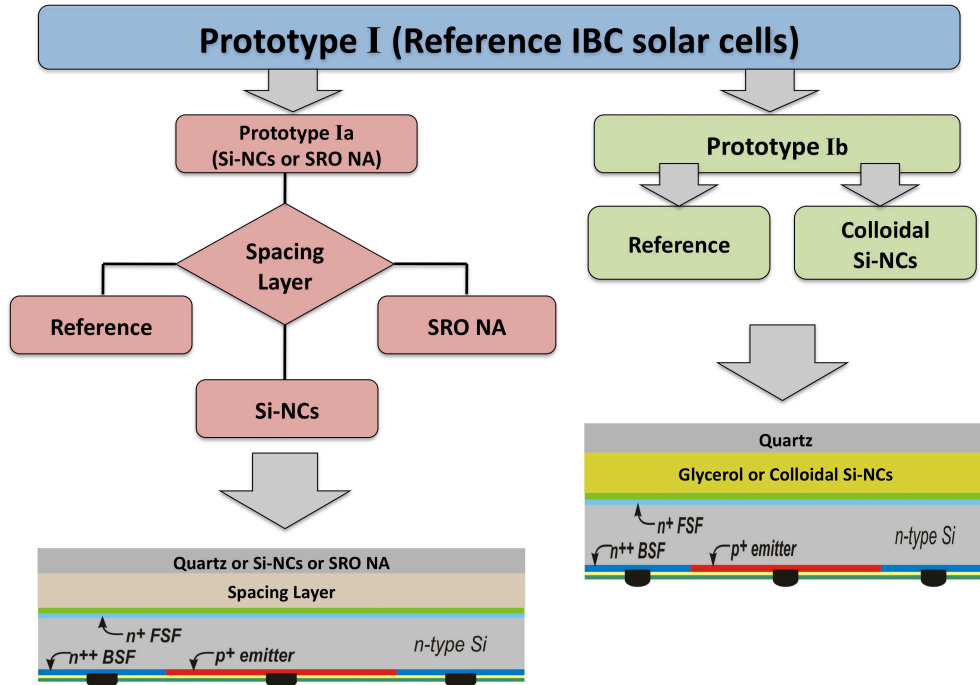


**Figure 3.1:** Method used to integrate silicon nanocrystals after the fabrication process of IBC solar cell. We considered two different approaches using a SRO layer deposited on quartz substrate ( $500\ \mu\text{m}$  thick), called Prototype Ia, and colloidal Si-NCs dispersed in a glycerol solution, called Prototype Ib, as active material respectively. In the method Prototype Ia (red flowchart), also a cover composed by SRO layer not annealed (without Si-NCs) deposited on a quartz substrate ( $500\ \mu\text{m}$  thick) has been taken into account (SRO NA). Different configurations (labeled air, glycerol and RIML) have been considered changing the medium in the cover-glass/IBC spacing layer. Reference means IBC solar cell (Prototype I) capped by a quartz cover ( $500\ \mu\text{m}$  thick) with the different “liquids” in the spacing layer. The green flowchart illustrates the path followed when we applied colloidal Si-NCs dispersed in a glycerol solution as “active liquid” in the spacing layer. A quartz layer was used as the cell cover. Here the reference configuration is characterized by glycerol in the spacing layer. It is important to observe that these different methods/configurations have a common element: we used exactly the same cell to perform the measurements.

as “active liquid” in the cover/IBC spacing layer (Prototype Ib). A quartz wafer ( $500\ \mu\text{m}$  thick) was used as cover glass in this case as well.

One of the advantages of this approach is its versatility. The very same IBC solar cells were used during the different measurements. In this way, we can eliminate the surface passivation contribution from a possible enhancement of the solar cell performances. Different references were considered, depending on the medium in

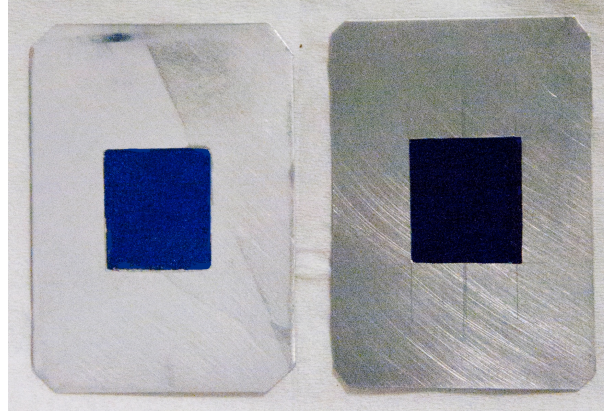


**Figure 3.2:** Top view of the IBC reference solar cells (Prototype I) used during the experiments: a flat (Left) and a textured (Right) front surface. Both devices are characterized by 80 nm of  $\text{SiN}_x$  as anti reflection coating. These two cells were stuck on a mask with an active area of  $1.8 \times 1.6 \text{ cm}^2$ . We used exactly the same cells during the different experiments.

the cover/IBC spacing layer. For all these configurations, a quartz  $500 \mu\text{m}$  thick was used to encapsulate the cell. In the approach Prototype Ib, glycerol was used in the spacing layer of the reference configuration.

We employed two different IBC reference cells (Prototype I) fabricated using the process flow described in Fig.2.20: a flat and a textured front surface (see Fig.3.2).

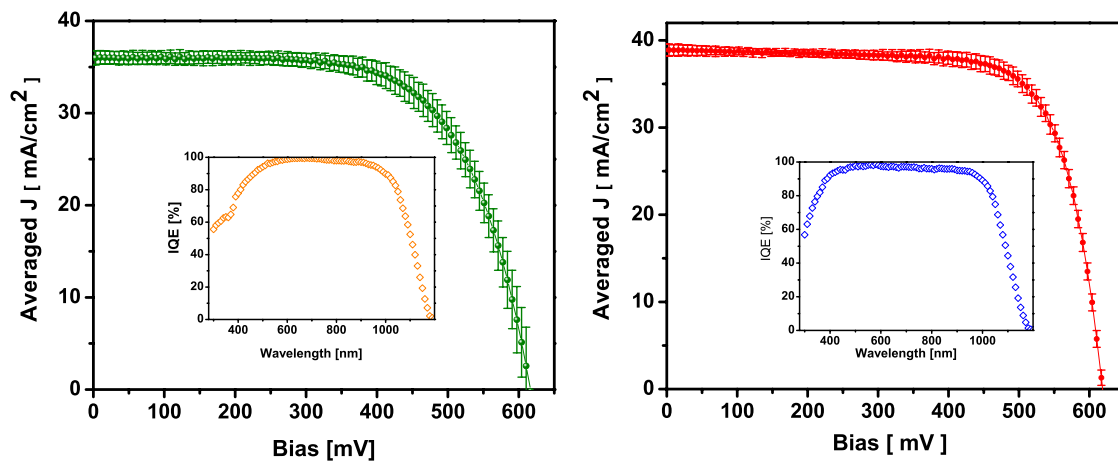


**Figure 3.3:** Measured J-V curves of the flat (Left) and textured (Right) front surface IBC solar cell. The statistics is based on at least 10 different measurements of the solar cells. The insets display the different internal quantum efficiency (IQE).

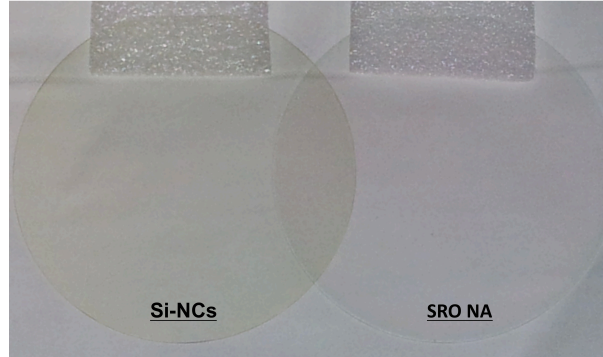


**Figure 3.4:** Picture of the produced cell covers. Left-side: 133 nm of annealed SRO layer deposited on a quartz substrate 500  $\mu\text{m}$  thick, called Si-NCs. Right-side: 141 nm of not annealed SRO layer deposited on a quartz substrate 500  $\mu\text{m}$  thick, called SRO NA. The Si-NCs cell cover glass shows the characteristic orange color of the SRO annealed at  $\sim 1110$   $^{\circ}\text{C}$  for one hour.

Fig.3.3 shows the measured J-V curves and the internal quantum efficiencies of these IBC devices. The textured cell was used in both approaches (Prototype Ia and Prototype Ib) while the flat front surface device only for Prototype Ia.

### 3.1.1 Si-NCs On Quartz substrate

The silicon nanocrystals have been produced at the Advanced Photonics & Photovoltaics center (AP&P-FBK-Trento-Italy) by thermal induced phase separation of plasma enhanced chemical vapor deposition (PECVD) depositing a silicon rich oxide (SRO) layer from  $\text{N}_2\text{O}$ ,  $\text{SiH}_4$  and nitrogen. The ratio of  $\text{N}_2\text{O}/\text{SiH}_4$  ( $\Gamma$ ) defines the excess amount of silicon in the film, while nitrogen is used for dilution (for more details see [122]). Homogeneous films with a  $\Gamma$  ratio of 15 and a different thicknesses were deposited on a quartz substrates 500  $\mu\text{m}$  thick. Two “covers” have been obtained with (annealing treatment  $\sim 1100$   $^{\circ}\text{C}$ ) and without (not annealed) active emitters, called Si-NCs and SRO NA respectively, as shown in the Fig.3.4.

The deposited thicknesses are the results of optimizations performed using the method described in subsections 2.2.1 and 2.2.3. In these simulations we used the IQE of the textured cell (Fig.3.3 right-side), a fixed quartz thickness (500  $\mu\text{m}$ ), a variable SRO thickness (from 0 nm to 800 nm) and QY (from 0% to 100%)<sup>2</sup>. The refractive indices used in the simulations are reported in Fig.3.5. As discussed

<sup>2</sup>Only for the Si-NCs “configuration”

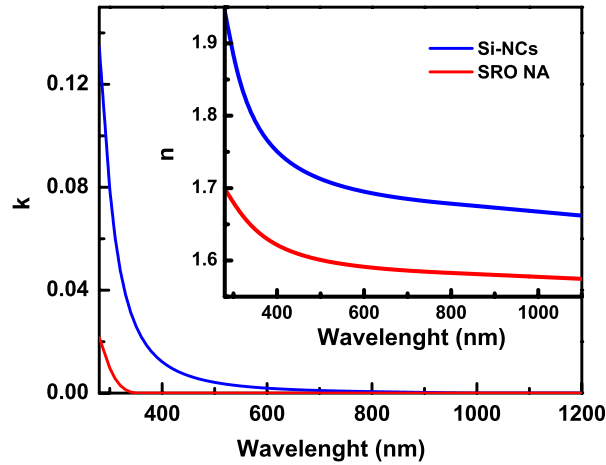


**Figure 3.5:** Nominal refractive index of two homogeneous films with a  $\Gamma$  ratio of 15 annealed (blue) and not annealed (red). The imaginary part of the not annealed sample is practically zero demonstrating no Si-NC formations. Measurements were done with a variable angle spectroscopy ellipsometer. These data were used in the optimization simulations for the two cell covers with and without active emitter.

in subsection 2.2.3, the optimization of the double layer stack is independent on the IQE of the specific solar cell. Fig.3.6 shows the results obtained assuming the

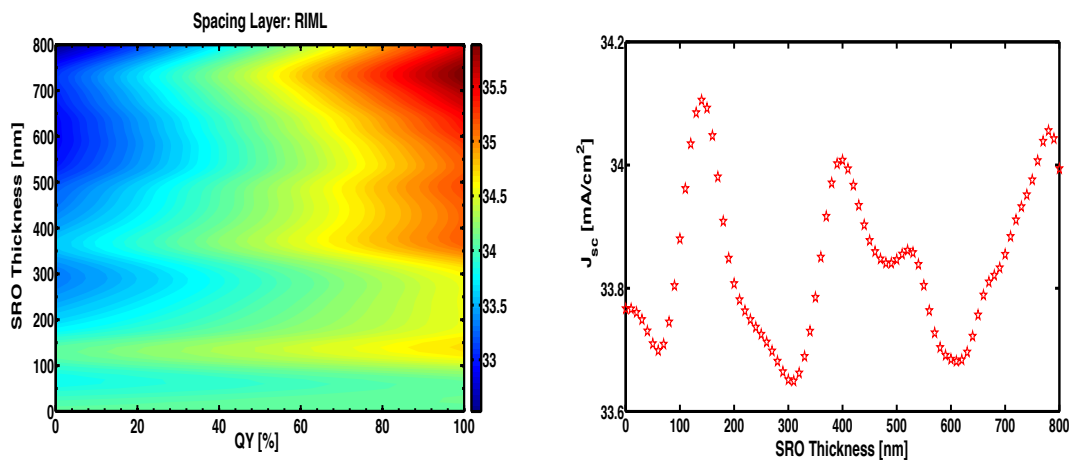


**Figure 3.6:** Optimization of the SRO layer thickness using as optimization gauge the short circuit current density ( $J_{sc}$ ). Left: Si-NCs “active cover” shows a maximum  $J_{sc}$  for  $\sim 130$  nm as a function of the quantum yield. Right-side:  $J_{sc}$  is maximized for  $\sim 140$  nm of SRO NA thickness. In both simulations the refractive index matching liquid ( $n \sim 1.7$ ) is used in the cover/IBC spacing layer.

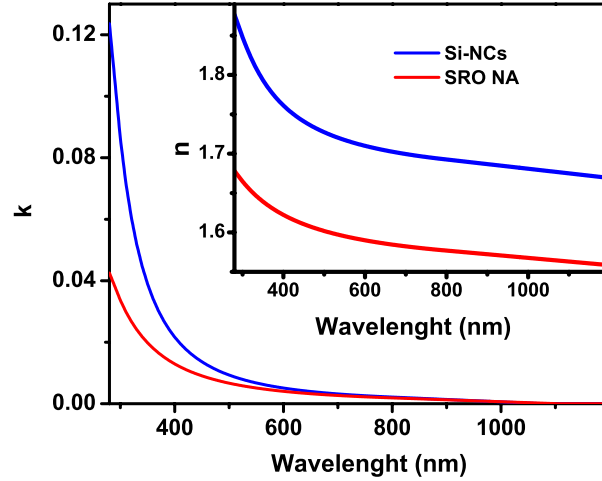


**Figure 3.7:** Imaginary ( $k$ ) and real ( $n$ ) part of the refractive indices of the covers measured using VASE.

refractive index matching liquid ( $n \sim 1.7$ ; for further details [124]) in the cover/IBC spacing layer. In the Si-NCs (for a fixed value of QY) and SRO NA “configuration”, the short circuit current density ( $J_{sc}$ ) is characterized by an oscillatory behavior as a function of the SRO thickness, *i.e.* different thicknesses means different interface effects. Moreover,  $J_{sc}$  increases with QY for a fixed value of the SRO thickness (Fig.3.6), *i.e.* more emission means more current produced. These simulations indicate an optimal SRO thickness value of 130 nm and 140 nm for the Si-NCs and SRO NA “configuration” respectively.

Optical properties of these devices were investigated with a variable angle spectroscopy ellipsometer (VASE) at the AP&P center. The ellipsometric spectra were measured from 280 nm to 1200 nm at different angles and the dielectric function, and then the refractive index, were obtained by a standard least square regression analysis (for further details [122]). The thicknesses of the two covers, extrapolated by these measurements, are 133 nm and 141 nm for Si-NCs and SRO NA respectively, in agreement with the simulation results. Moreover, Fig.3.7 displays the refractive index of these samples. These values are more or less equal to the ones used in the simulations (see Fig.3.5). SRO NA shows a low imaginary part ( $k$ ) of the refractive index, denoting no formations of the silicon nanoparticles. This hypothesis was validated performing photoluminescence (PL) measurements using the 355 nm line of a Nd:YVO<sub>4</sub> laser to excite the samples at normal incidence. Fig.3.8

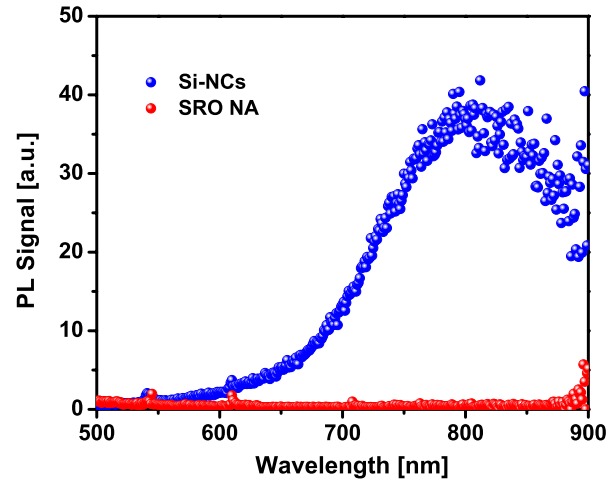


**Figure 3.8:** PL measurements performed on the produced samples. As expected, the SRO NA does not show any PL signal, confirming the absence of silicon nanoparticles.

exhibits the classical broad PL line shape for the Si-NCs due to the nanocrystals size distribution, while no PL is observed for the not annealed sample.

### 3.1.2 Colloidal Si-NCs in Glycerol solution

Glycerol suspended functionalized Si-NCs were obtained from sonification of porous silicon as described in [125]. These “active liquids” were produced by Dr.E.Froner at the University of Trento. Fig.3.9 shows a picture of vials containing the colloidal Si-NCs in glycerol suspension under an UV lamp illumination: a clear orange visible emission is observed.

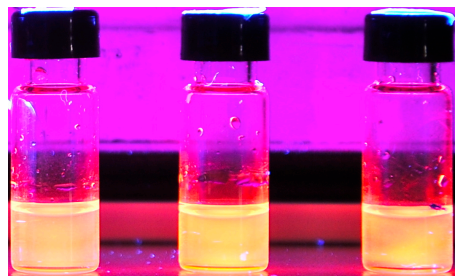


**Figure 3.9:** Vials containing colloidal silicon nanoparticles in glycerol suspension. An orange visible emission is produced by these “active liquids” under an UV lamp illumination.

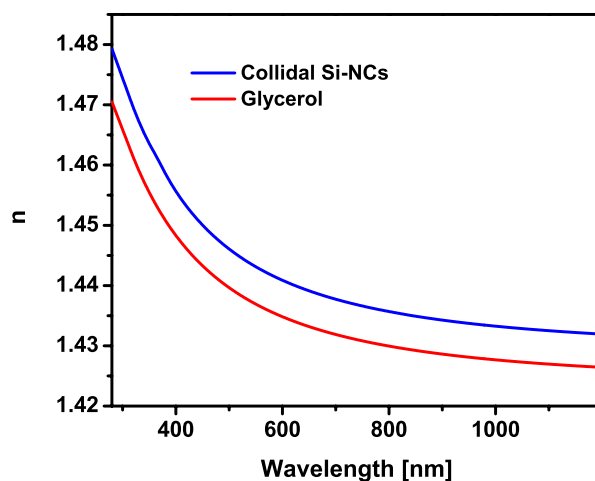


**Figure 3.10:** Real refractive index of colloidal Si-NCs in glycerol solution (blue line) compared with the refractive index of glycerol measured using a VASE.

In order to evaluate the optical properties of this colloidal solution, our partners at AP&P center measured its refractive index with respect to the refractive index of the glycerol. The results are shown in Fig.3.10. The optical properties of the “active liquid” are very similar to ones of the glycerol. This result is very important for our purpose. Indeed, we can compare the performances of the colloidal Si-

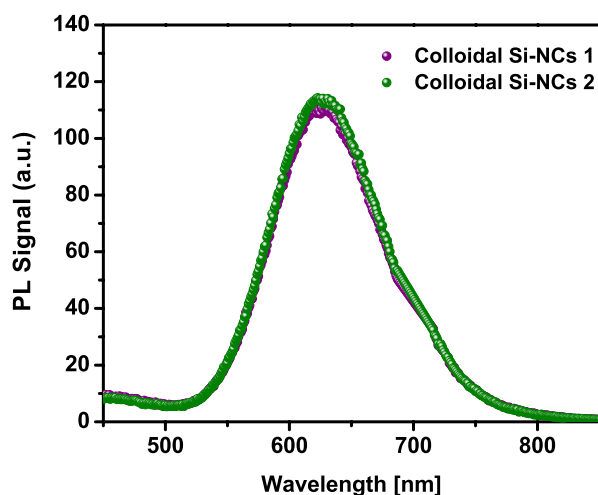


**Figure 3.11:** PL measurements of colloidal Si-NCs dispersed in a glycerol solution performed using a fluorescence spectrometer. These two “active liquids” show the same PL spectra.

NCs configuration with the ones of a reference cell characterized by glycerol in the quartz-cover-glass/IBC spacing layer excluding possible enhancements produced by a different optical composition.

Prepared Si-NCs suspended in glycerol show a broad luminescence band which peaks around 630 nm indicating an average size of 2 nm - 3 nm [25]. Fig.3.11 exhibits the photoluminescence signal generated by the colloidal solutions measured using a fluorescence spectrometer.

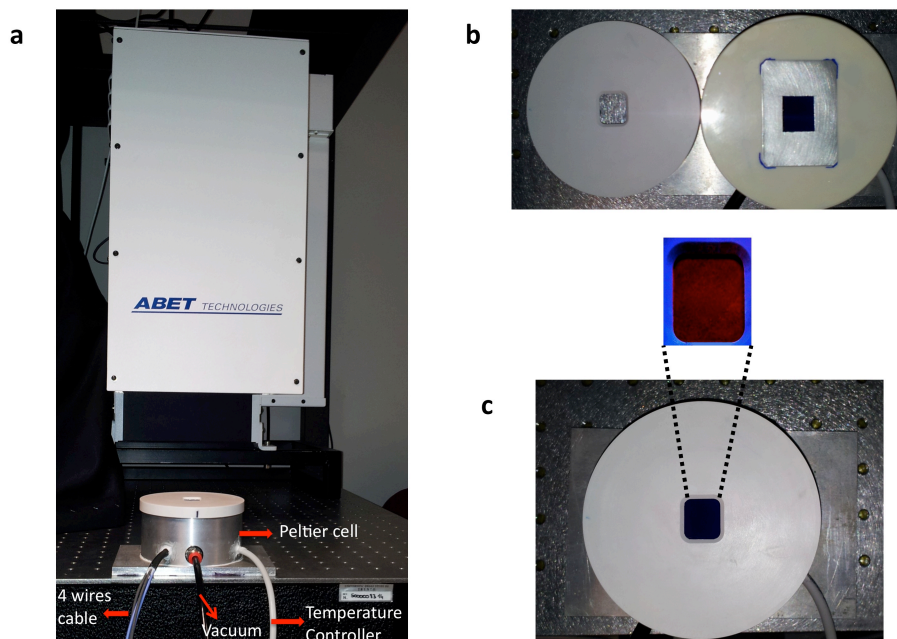


**Figure 3.12:** a) Picture of the setup: a Peltier cell was used to control the temperature of the cell during the experiments thanks to a vacuum pump and a temperature controller. The I-V curves were performed using four wires cables. b) Prototype Ia approach : two different covers were employed to encapsulate the IBC solar cell using different materials in the cover/IBC spacing layer. The white mask, showed in the figure, was used to illuminate only the active area of the cell and to preserve the realized “sandwich”. c) Method Prototype Ib: colloidal Si-NCs dispersed in glycerol solution were used as “active liquid” in the quartz-cover-glass/IBC spacing layer. The zoom shows the visible emission of the “active liquid” when it is encapsulated in the IBC cell under an UV lamp illumination.

## 3.2 Experimental Results

In this section, I will present the experimental results obtained using the methods described in section 3.1. These measurements were performed using an ABET sun 2000 solar simulator class AAB (as shown in Fig.3.12 a) and a Keithley series 2612A to evaluate I-V curves. In order to calibrate our setup, irradiance measurements were performed using a package silicon reference cell. The performances of this package cell are shown in Table.2.2. In order to be confident on the stability of the illumination source, calibration measurements were performed each time that we changed the different cell covers. Moreover, I-V curves were performed on the masked IBC solar cells (Fig.3.2) each time that we changed the medium in the spacing layer. These measurements were executed to control possible “degradation” effects on the IBC due to the application of the different “materials”. We observed each time the characteristic I-V curves shown in Fig.3.3.

### 3.2.1 SRO on Quartz: Experimental Results

The experimental results obtained with Prototype Ia (see Fig.3.12 b) are shown in Fig.3.13 and in Fig.3.14 using a textured and a flat IBC solar cell, respectively. In order to clarify the set of the performed measurements, Table.3.1 summarizes the composition of the cell covers used in the different configurations.

We used the relation

$$\Delta J_{sc}^{cover} = \left( \frac{J_{sc}^{cover} - J_{sc}^{ref}}{J_{sc}^{ref}} \right) \times 100 \quad (3.1)$$

to evaluate the  $J_{sc}$  enhancement.  $J_{sc}^{cover}$  and  $J_{sc}^{ref}$  are the short circuit current densities of the reference and “cover” configuration. “cover” refers to SRO NA or Si-NCs (see Table.3.1). The red, orange, and blue rectangles identify the Air, Glycerol, and RIML configuration respectively. The obtained results show the same trend, when

**Table 3.1:** Summary of the cell covers used in the different configurations

Ref.	Quartz 500 $\mu\text{m}$	Spacing Layer (Air, Glycerol, RIML)	IBC solar cell
SRO NA	Quartz 500 $\mu\text{m}$ + 140 nm SRO NA <sup>a</sup>	Spacing Layer (Air, Glycerol, RIML)	IBC solar cell
Si-NCs	Quartz 500 $\mu\text{m}$ + 130 nm SRO <sup>b</sup>	Spacing Layer (Air, Glycerol, RIML)	IBC solar cell

<sup>a</sup>Silicon rich oxide not annealed.

<sup>b</sup>Silicon rich oxide annealed at  $\sim 1100$  °C.

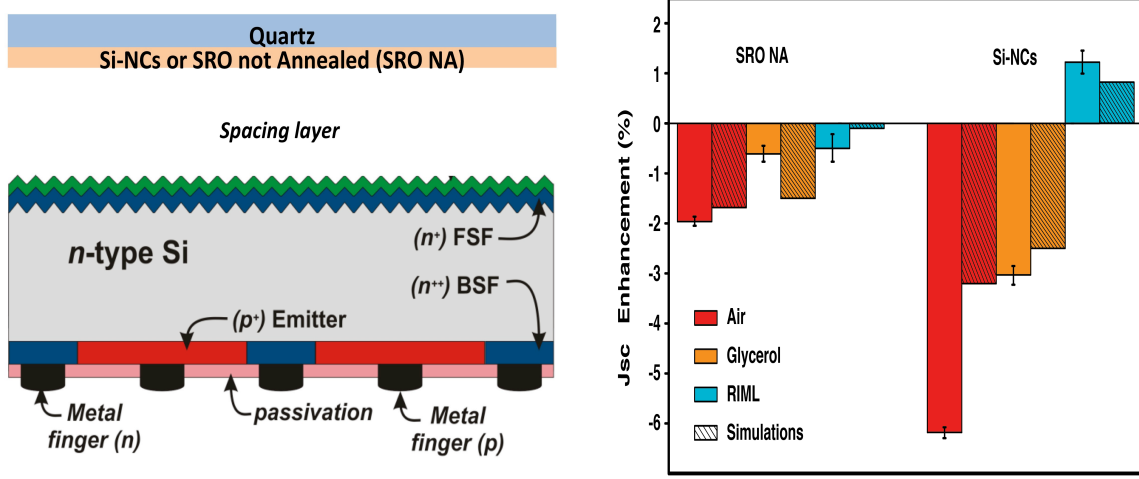


**Figure 3.13:** Left-side: A textured IBC device is capped with two cell covers with (Si-NCs) and without (SRO NA) active emitters. We used different materials in the cover/IBC spacing layer: air, glycerol, and refractive index matching liquid (RIML). Right-side:  $J_{sc}$  enhancement measured in the different configurations. The simulations are performed using the method described in subsection 2.2.3. We used a quantum yield (QY) equal to 20% to simulate the different Si-NCs configurations. A QY equal to 0% was assumed to model the SRO NA cover in the different configurations. The error bars are evaluated with the standard deviations of the mean performing J-V measurements repeated 15 times using the same cover.

we used the textured and the flat IBC solar cell. We found a positive enhancement ( $J_{sc}^{cover} > J_{sc}^{ref}$ ) only in the case of Si-NCs as cover in the RIML configuration:  $(1.22 \pm 0.21)\%$  for the textured cell and  $(1.55 \pm 0.2)\%$  for the flat IBC device. Conversely, no enhancement was observed in the other configurations (Air and Glycerol), using both SRO NA and Si-NCs as covers.

The origin of these improvements in the short circuit current density are related to the luminescence downshifting effect. In fact, the same solar cell was used during these experiments, excluding any possible enhancements related to a better surface passivation. In order to exclude also the contribution related to the optical properties of the employed materials, we simulated the transmission in the silicon substrate by using the Si-NCs, SRO NA, and the quartz covers in the RIML configuration. These simulations were performed with the thin film software Scout [108] using the refractive indices reported in Fig.3.7, and the thicknesses of the different covers. As shown in Fig.3.15, the transmission produced by these three structures is practically

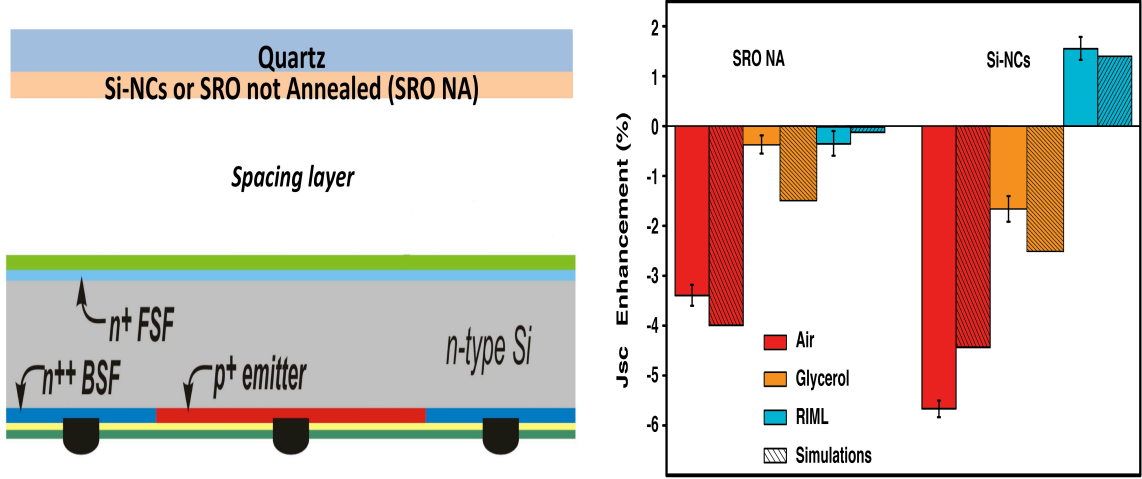


**Figure 3.14:** Left-side: A flat front surface IBC device is capped with two cell covers with (Si-NCs) and without (SRO NA) active emitters. We used different material in the cover/IBC spacing layer: air, glycerol, and refractive index matching liquid (RIML). Right-side: Short circuit current density enhancement in the different configurations. The simulations are performed using the method described in subsection 2.2.3. We used a quantum yield (QY) equal to 20% to simulate the different Si-NCs configurations. A QY equal to 0% was assumed to model the SRO NA cover in the different configurations. The error bars are evaluated with the standard deviations of the mean performing J-V measurements repeated 15 times using the same cover.

the same, excluding the UV-range where the Si-NCs absorb. Moreover, the quartz layer transmits more UV-photons with respect to the SRO NA configuration. This can explain why  $J_{sc}^{ref}$  is larger than  $J_{sc}^{SRO NA}$  in the Fig.3.13 and Fig.3.14 in the RIML configuration. The observed enhancement in the  $J_{sc}$  is not produced by a better matching between the refractive index in the Si-NCs with respect to the reference “configuration”. The last possible explanation is that Si-NCs absorb high energy photons and efficiently emit low energy photons towards the IBC solar cell. The simulations, reported in Fig.3.13 and Fig.3.14, seem validate this analysis.

The reason why we observe an enhancement only for the RIML configuration is because in this case its refractive index is appropriate to drive most of the Si-NC emission towards the silicon cell. In order to demonstrate this effect, in Chapter 4 we will show simulations based on Purcell’s effect to evaluate the fraction of the emitted light that reaches the silicon solar cell in the different configurations. This study suggests that the emission, produced by an array of electric dipoles, is highly directed

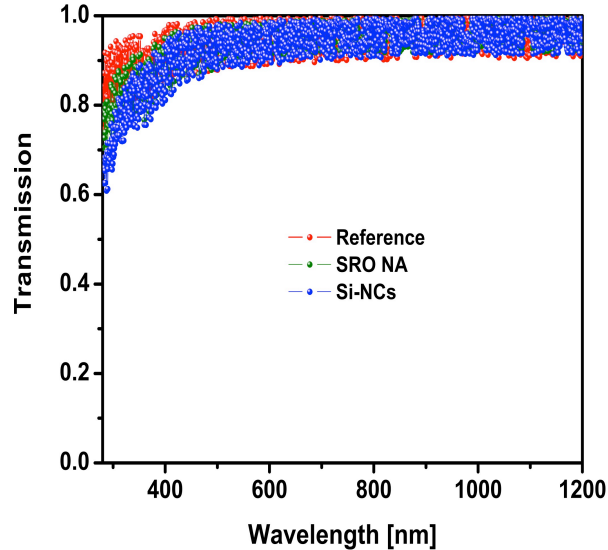


**Figure 3.15:** Simulated transmissions in the silicon substrate produced by the Si-NCs (blue points), SRO NA (green points), and the quartz (red points) covers in the RIML configuration. The oscillations are related to Fabry Perot interferences caused by the quartz ( $500 \mu\text{m}$ ) and the spacing layer ( $\approx 200 \mu\text{m}$ ) thickness.

towards the substrate only in the RIML configuration thanks to the modification of the local optical density of states.

### 3.2.2 Colloidal Si-NCs: Experimental Results

Fig.3.16 shows the results obtained using colloidal Si-NCs in glycerol solution as active material in the quartz-cover/IBC spacing layer (see Fig.3.12 c). A quartz substrate  $500 \mu\text{m}$  thick has been used to encapsulate the “active liquid” on the textured IBC solar cell (see Fig.3.2). Also in this configuration, an enhancement<sup>3</sup> of  $(2.33 \pm 0.17)\%$  was measured using Si-NCs with respect to a reference “configuration” characterized by glycerol in the quartz-cover/IBC spacing layer.

In order to analyze the origin of this improvement, we performed an experiment based on the modification of the incident sunlight radiation. We used a long wave pass filter (L.W.P.F.) and a short wave pass filter (S.W.P.F.) located on the top of the white mask shown in Fig.3.12 c. The UV part of the incident radiation is cut using the L.W.P.F., as shown in Fig.3.17 left-side. In this situation, we expect

<sup>3</sup>Computed using the relation (3.1).

no enhancement thanks to the LDS effect because Si-NCs do not absorb. Indeed, we measured a “negative” gain equal to  $(-0.48 \pm 0.12)\%$ , *i.e.*  $J_{sc}^{Ref} > J_{sc}^{Si-NCs}$ . On the other hand, an improvement of  $(1.58 \pm 0.21)\%$  was observed using the S.W.P.F. (Fig.3.17 left-side).

We simulated the optical properties of these structures to analyze the contribution of a better matching between the refractive index of the materials involved in the colloidal Si-NCs with respect to the reference configuration. Fig.3.18 shows the simulated transmission spectra, performed by using the thin film software Scout [108], that reach the silicon substrate, multiplied by the measured transmissions of the two filters. The transmissions towards the silicon are practically the same in the range  $\sim 600$  nm-1200 nm for both structures. On the contrary, more UV photons are transmitted in the reference with respect to the colloidal Si-NCs configuration (Fig.3.18 left-side). Indeed, the Si-NC absorbs the incident UV light resulting in a lowering transmission. The active material is simulated as an effective medium

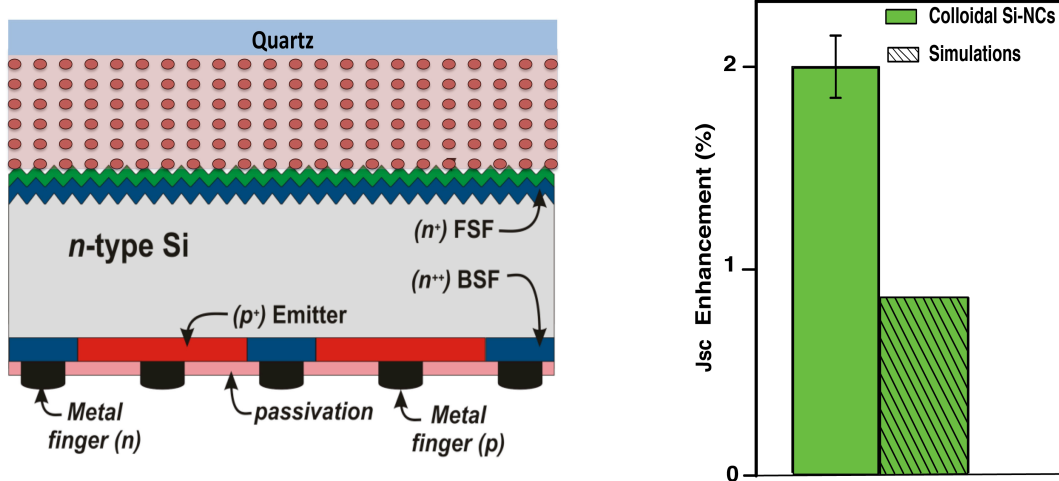


**Figure 3.16:** Left-side: Colloidal Si-NCs dispersed in a glycerol solution are used as active material in the quartz-cover/IBC spacing layer. Right-side: Short circuit current density enhancement. The simulations are performed using the method described in subsection 2.2.3. We used a QY equal to 30% in these simulations. This value was independently confirmed by experimental measurements [125]. From the QY and the values for absorption cross section of Si-NC found in literature [126], the concentration of these functionalized Si-NC was estimated to be approximately  $10^{13}$   $\text{cm}^{-3}$  [125]. The error bars are evaluated with the standard deviations of the mean performing J-V measurements repeated 15 times using the same cover.

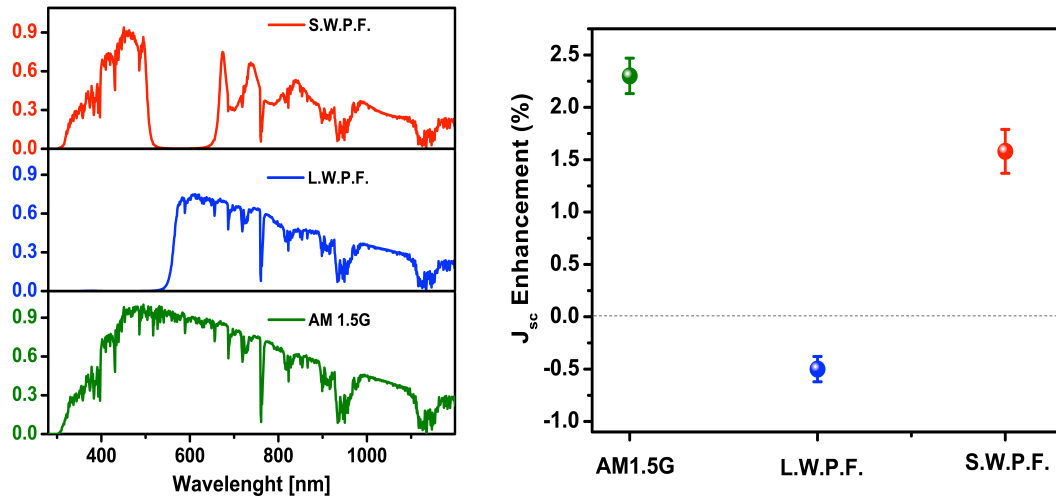


**Figure 3.17:** Left-side: Normalized (to the maximum value) solar spectra: AM1.5 G (green), normalized AM1.5 G multiplied by the measured transmittance of a long-wave-pass-filter (L.W.P.F.) (blue), normalized AM1.5 G multiplied by the measured transmittance of a short-wave-pass-filter (S.W.P.F.). Right-side: Measured  $J_{sc}$  enhancements, evaluated using the relation (3.1), using different incident solar spectra: AM1.5G (green), AM1.5G filtered by a L.W.P.F. (blue), and AM1.5G filtered by a S.W.P.F. (red).

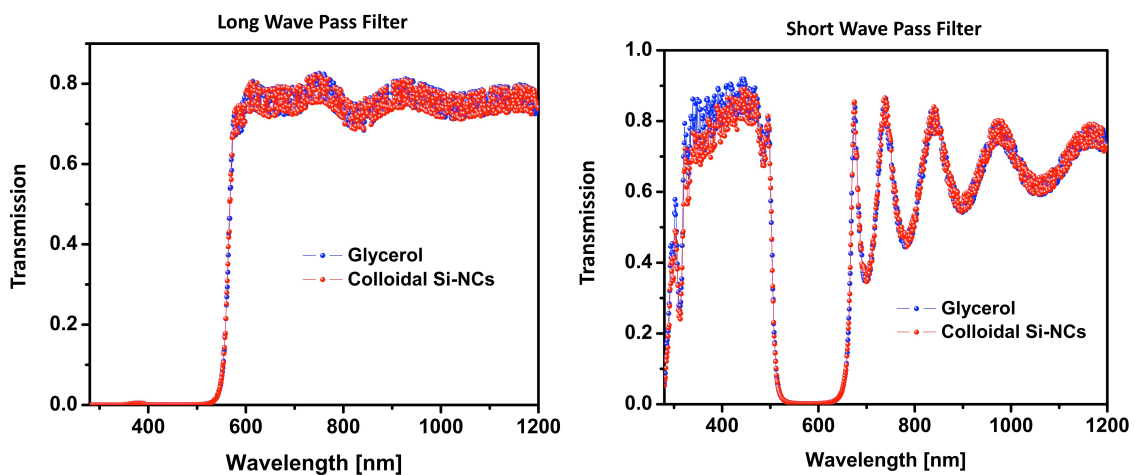


**Figure 3.18:** Simulated transmission spectra multiplied by the measured transmission spectra produced by the long wave pass filter (left side) and the short wave pass filter (right-side) used during the measurements.

via its refractive index, *i.e.* only the “passive” properties of the colloidal Si-NCs dispersed in a glycerol solution are taken into account in these simulations. The  $J_{sc}$  enhancement using colloidal Si-NCs (red point in Fig.3.17) cannot be related to a more fraction of photons that arrive in the IBC cell with respect to the reference configuration. Therefore, we can argue that the active role of Si-NCs is switched on using the short wave pass filter with respect to the long wave pass filter: high energy photons are absorbed and low energy photons are re-emitted increasing the number of light generated carrier effectively used by the solar cell. As consequence, also the enhancement of  $(2.33 \pm 0.17)\%$  under AM1.5G illumination can be explained using the LDS effect in combination with an increased number of the available optical states, *i.e.* LDOS modification effect (for further details see Chapter 4)

### 3.3 Conclusions

While in Chapter 2 a method based on the integration of a silicon quantum dots layer during the fabrication process of the interdigitated back contact (IBC) silicon solar cells was presented, in this chapter I showed two alternative approaches to integrate an active layer after the fabrication of an IBC solar devices.

The first method was based on the deposition, via PECVD, of a silicon rich oxide layer not directly on the cell but on a quartz substrate  $500 \mu\text{m}$  thick. The idea, resembling the cover glass of a PV module, was to use this “active cover” to encapsulate the IBC device changing the material in the cover/IBC spacing layer to “activate” the optical properties in the cell cover glass. An advantage in the use of this innovative scheme is its versatility, *i.e.* it can be used on different solar cells. Moreover, we can separate the luminescence downshifting effect (LDS) by the surface passivation in a possible improvement of the solar cell performances because the same device is used during the experiments, contrary to what found in Chapter 2.

Improvements of  $(1.22 \pm 0.21)\%$  and  $(1.55 \pm 0.2)\%$  with respect to a reference configuration were measured using a refractive index liquid matching ( $n \sim 1.7$ ) in the cover/IBC spacing layer for two different IBC devices: a textured and a flat front surface, respectively.

In the second approach, colloidal Si-NCs dispersed in a glycerol solution were used as “active liquid” in the IBC/spacing layer. Then a “sandwich” was realized

using a quartz cover glass 500  $\mu\text{m}$  thick. Also in this situation, we found an improvement of  $(2.3 \pm 0.17)\%$  in the short circuit current density with respect to a reference configuration characterized by only glycerol.

Optical simulations were performed to relate these enhancements to the active role played by silicon nanoparticles in both approaches. Moreover, an experiment on the modification of the incident sunlight radiation using respectively a long and a short Wave Pass Filter (WPF) was considered in the case of colloidal Si-NCs as emitters. No enhancement was observed using the long WPF since the UV-radiation, *i.e.* the precursor of the LDS effect, is cut by the filter. On the other hand, an improvement was detected putting the short WPF. Excluding any possible enhancement produced by a better ARC of the used material in the “active”<sup>4</sup> with respect to the reference configurations, we have explained the observed improvements as a manifestation of the LDS effect.

---

<sup>4</sup>“Active” refers to the use of silicon nanoparticles.

---

## Chapter 4

# LDOS Modification: directionality of the emitted light

In this chapter, I will focus on the possibility to control the spontaneous emission process by placing emitters near a suitable environment. First, I will introduce this topic presenting some fundamental details on the radiation pattern produced by a classical oscillating dipole placed in a homogeneous media. After, the spontaneous emission will be treated using the Fermi Golden's rule, and the Dyadic Green's functions. These concepts will be exploited to establish a connection between the classical and the quantum mechanics framework: the partial local density of states (LDOS) can be connected with the power radiated by an oscillating electric dipole to analyze the LDOS modification due to the environment. In section 4.3, I will analyze the LDOS modification induced by emitters located at the interface of two different materials and I will present some details concerning the radiation pattern generated by a vertical electric dipole. At the end, after some considerations on the validity of the dipole approximation in the case of silicon nanoparticles, I will consider an array of 100 electric dipoles placed within different multilayer systems in order to explain the results of chapter 3 in terms of Purcell's effect.

## 4.1 Classical Oscillating Dipole

An electric dipole is formed by two equal but opposite electric charges separated by a certain distance. The dipole acts as a current source defined by the equation

$$\mathbf{j}(\mathbf{r}, t) = \mathbf{p}\delta(\mathbf{r} - \mathbf{r}_0)e^{-i\omega_0 t} \quad (4.1)$$

where  $\mathbf{p} = I_0\mathbf{n}_p$  is the dipole moment,  $\mathbf{n}_p$  expresses the dipole orientation,  $I_0$  denotes  $i d$  where  $i$  is the total current and  $d$  is the dipole length,  $\delta(\mathbf{r} - \mathbf{r}_0)$  identifies the dipole position in the space, and  $\omega_0$  represents the emission frequency. In order to determine the emitted power produced by a dipole located in a homogeneous, linear and isotropic space, we can resolve Maxwell's equations using (4.1) as current source. After some manipulations, it follows that the Faraday law, in the *mks* system of units, becomes [127]

$$\nabla \times \nabla \times \mathbf{E}(\mathbf{r}, \omega) - k^2\mathbf{E}(\mathbf{r}, \omega) = -i\mu\omega_0 I_0\delta(\mathbf{r} - \mathbf{r}_0)\mathbf{n}_p \quad (4.2)$$

where  $\mu$  is the magnetic permeability and  $k = n\omega/c$  expresses the wave vector in a medium with refractive index  $n$ . To solve this problem, we can introduce the electric Hertz vector  $\mathbf{\Pi}(\mathbf{r}, \omega)$  and, using the Lorentz gauge, we can connect it to the electric and magnetic fields

$$\mathbf{E}(\mathbf{r}, \omega) = k^2\mathbf{\Pi}(\mathbf{r}, \omega) + \nabla(\nabla \cdot \mathbf{\Pi}(\mathbf{r}, \omega)) \quad (4.3)$$

$$\mathbf{B}(\mathbf{r}, \omega) = \frac{k^2}{i\omega_0}\nabla \times \mathbf{\Pi}(\mathbf{r}, \omega) \quad (4.4)$$

From (4.2), and (4.3) it follows, after some manipulation, that

$$\nabla^2\mathbf{\Pi}(\mathbf{r}, \omega) + k^2\mathbf{\Pi}(\mathbf{r}, \omega) = \frac{-i\omega_0\mu}{k^2}I_0\delta(\mathbf{r} - \mathbf{r}_0)\mathbf{n}_p \quad (4.5)$$

Because the dipole is located in a homogeneous environment, all three dipole orientations lead to fields that are identical upon suitable frame rotations. Choosing a coordinate system with origin in  $\mathbf{r}_0$ , and fixing the dipole orientations along the dipole axis, *i.e.*  $\mathbf{n}_p = \mathbf{e}_z$ , the field components, in a spherical coordinate system  $\mathbf{r} = (r, \theta, \phi)$  [128, 129], become:

$$E_r(t) = \frac{\cos\theta}{4\pi\epsilon_0\epsilon} \left[ \frac{2}{r^3} + \frac{2n}{cr^2} \frac{d}{dt} \right] |\mathbf{p}(t - nr/c)| \quad (4.6)$$

$$E_\theta(t) = \frac{\sin\theta}{4\pi\epsilon_0\epsilon} \left[ \frac{1}{r^3} + \frac{n}{cr^2} \frac{d}{dt} + \frac{n^2}{c^2r} \frac{d^2}{dt^2} \right] |\mathbf{p}(t - nr/c)| \quad (4.7)$$

$$H_\phi(t) = \sqrt{\frac{\epsilon_0\epsilon}{\mu_0\mu}} \frac{\sin\theta}{4\pi\epsilon_0\epsilon} \left[ \frac{n}{cr^2} + \frac{n^2}{c^2r} \frac{d^2}{dt^2} \right] |\mathbf{p}(t - nr/c)| \quad (4.8)$$

where  $\epsilon$  represents the relative dielectric constant,  $n$  denotes the (dispersion-free) index of refraction, and  $(t - nr/c)$  is the retarded time. Another important aspect regards the dimension of the radiating source. Indeed, the current source must be confined in a very small region compared to the emission wavelength. If the dimension of the source is of the order of  $d$  and the wavelength is  $\lambda_0 = 2\pi c/\omega_0$ , under the condition  $d \ll \lambda$ , three spatial regions must be analyzed [129]

- the near (static) zone  $d \ll r \ll \lambda$
- the intermediate (induction) zone  $d \ll r \simeq \lambda$
- the far (radiation) zone  $d \ll \lambda \ll r$

where  $r$  identifies the position of the detector, *i.e.* the position with respect to which we detect the radiation emission. The fields have very different properties in the different regions. In the near zone the fields are static fields, with radial components and variation with the distance that depend in detail on the properties of the source. In the intermediate zone, we can express the oscillating term of the Hertz vector as [129, 130]

$$\frac{e^{ikr}}{r^{(l+1)}}(1 + a_1(ikr) + a_2(ikr)^2 + \dots + a_l(ikr)^l)$$

that shows the transition from the static (for  $kr \ll 1$ ) to the radiation zone (for  $kr \gg 1$ ). In the far zone, the fields are transverse to the radius vector and fall off as  $r^{-1}$  (typical of radiation fields) demonstrating that  $\mathbf{\Pi}$  behaves as an outgoing spherical wave with an angular dependent coefficient [127]. Indeed, the equation (4.6) has not far field term, ensuring that the far field is purely transverse. The Poynting vector  $\mathbf{S}(t)$  associated with the far field<sup>1</sup> can be calculated by retaining only the  $r^{-1}$  terms in the equations (4.7) and (4.8) obtaining [128, 129]:

$$\mathbf{S}(t) = \mathbf{E}(t) \times \mathbf{H}(t) = \frac{1}{16\pi^2\epsilon_0\epsilon} \frac{n^3 \sin^2\theta}{r^2 c^3} \left[ \frac{d^2}{dt^2} |\mathbf{p}(t - nr/c)| \right]^2 \mathbf{n}_p$$

The radiated power  $P$  can be determined by integrating  $\mathbf{S}(t)$  over a closed spherical surface as

$$P(t) = \int_{\partial V} \mathbf{S} \cdot \mathbf{n}_{surface} dA = \frac{1}{4\pi\epsilon_0\epsilon} \frac{2n^3}{3c^3} \left[ \frac{d^2}{dt^2} |\mathbf{p}(t)| \right]^2$$

<sup>1</sup>Only the far field component of the dipole fields contributes to a net energy transport.

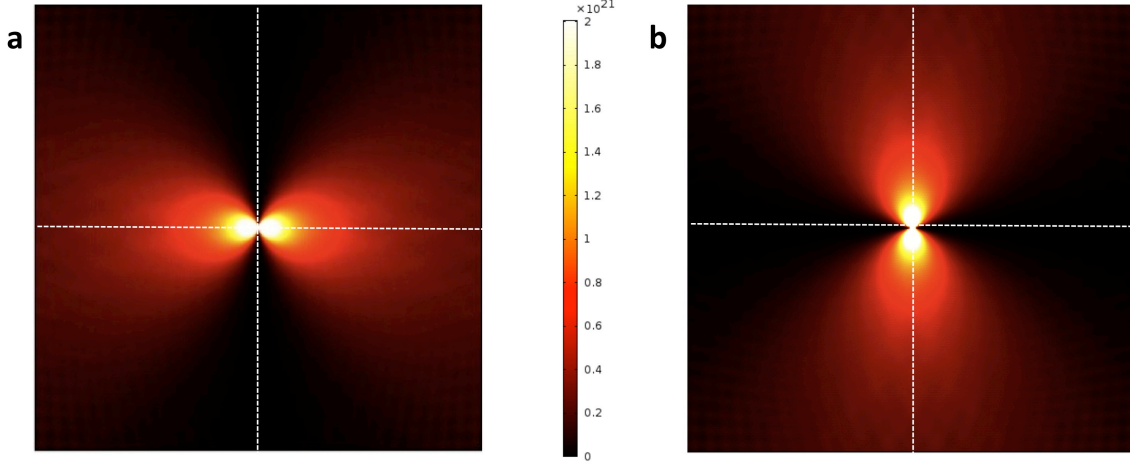


**Figure 4.1:** Radiation pattern of a vertical (a) and a horizontal (b) oscillating dipole in a homogeneous medium.

where we have shrunk the radius of the sphere to zero to get rid of the retarded time. The average radiated power for a harmonically oscillating dipole turns out to be

$$\bar{P} = \frac{|\mathbf{p}|^2}{4\pi\epsilon_0\epsilon} \frac{n^3\omega_0^4}{3c^3} \quad (4.9)$$

which could also have been calculated by integrating the time-averaged Poynting vector  $\langle \mathbf{S} \rangle = (1/2)\text{Re}[\mathbf{E} \times \mathbf{H}]$  where  $\mathbf{E}$  and  $\mathbf{H}$  are the complex dipole's amplitude.

Fig.4.1 shows the radiated emission (Poynting vector) of two oscillating dipoles with different orientations  $\mathbf{n}_p$ : a vertical ( $\mathbf{n}_p = \mathbf{e}_y$ ) oscillating dipole (Fig.4.1 a), and a horizontal ( $\mathbf{n}_p = \mathbf{e}_x$ ) oscillating dipole (Fig.4.1 b). The radiation pattern depends strongly on the dipole orientation because most of the energy is radiated perpendicular to the dipole moment. In both cases, the emission is zero along the dipole axes, as expected. Moreover, the far field behavior, when the distance of the detector increases with respect to the location of the dipole<sup>2</sup>, is evident. According to the Poynting's theorem, the radiated power of any current distribution with a harmonic time dependence in a linear medium has to be identical to the rate of energy dissipation  $dW/dt$  given by

$$\frac{dW}{dt} = \frac{1}{2} \int_V \text{Re}[\mathbf{E}(\mathbf{r}) \cdot \mathbf{j}^*(\mathbf{r})] \quad (4.10)$$

<sup>2</sup>Center of the simulation plane in both cases.

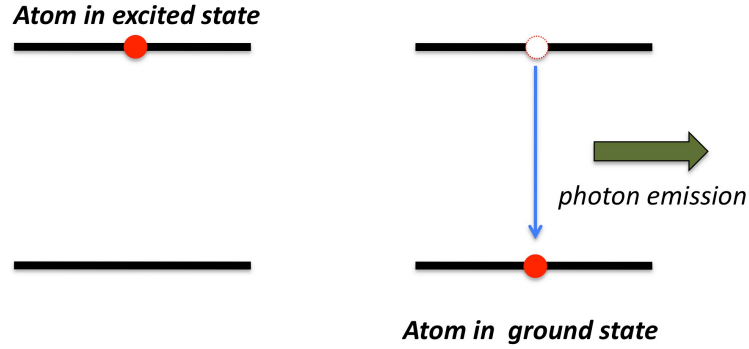


**Figure 4.2:** The interactions of the vacuum fluctuations of the electromagnetic field with the atom in the excited state produce a transition to the lower state emitting a photon to carry out the excess energy.

where  $V$  is the source volume,  $\mathbf{j}$  the source current density, and  $\mathbf{E}$  the electric field. The current density (equation(4.1)) can be expanded in a Taylor series around the origin  $\mathbf{r}_0$  and, in the lowest approximation, can be written as  $\mathbf{j}(\mathbf{r}) = -i\omega_0\mathbf{p}\delta(\mathbf{r} - \mathbf{r}_0)$ . The equation (4.10), then, becomes

$$\frac{dW}{dt} = \frac{\omega}{2} \text{Im}\{\mathbf{p}^* \cdot \mathbf{E}(\mathbf{r}_0)\} \quad (4.11)$$

The electric field  $\mathbf{E}(\mathbf{r}_0)$  is the field generated by the dipole and evaluated at the dipole's origin  $\mathbf{r}_0$ . The power of this approach is its generalization at more interesting situations, as the radiation patterns of emitters located on the separation interface of two half spaces characterized by different materials. In order to understand this important issue, we need to discuss first the characteristics of the spontaneous emission.

## 4.2 Spontaneous Emission

The spontaneous emission occurs when an atom is in an unstable excited state and randomly decays to a less energetic state, emitting a photon to carry off the excess energy. The unstable state decays in a characteristic time, called the lifetime. The simplest example of this kind of radiation is a two-level quantum emitter, as depicted in the Fig.4.2. The radiative decay rate of a two-level quantum system  $|i\rangle$

and  $|f\rangle$  is evaluated using Fermi's golden rule [131, 132]

$$\gamma = \frac{2\pi}{\hbar^2} \sum_f |\langle f | \hat{H}_I | i \rangle|^2 \delta(\omega_i - \omega_f) \quad (4.12)$$

where  $\hat{H}_I = -\hat{\mathbf{p}} \cdot \hat{\mathbf{E}}$  is the interaction hamiltonian in the dipole approximation (DA). DA is one of the most central and successful approximations in quantum optics and quantum electrodynamics (QED). In the framework of light-matter interaction, DA is valid if the variation of the electromagnetic field is negligible over the spatial extent of the emitter. This is an excellent approximation in atomic physics since optical wavelengths exceed atomic dimensions by orders of magnitude. Moreover, the equation (4.12) has been obtained with the first order perturbation theory and thus is valid in the limit of weak-coupling regime, that is when light and matter can be treated as separated, yet interacting entities. The radiative decay rate can be also expressed as

$$\gamma = \frac{2\omega_0}{3\hbar\epsilon_0} |\mathbf{p}|^2 \rho_p(\mathbf{r}_0, \omega_0) \quad (4.13)$$

introducing the *partial local density of states*, which corresponds to the number of modes per unit of volume and frequency, defined by the relation:

$$\rho_p(\mathbf{r}_0, \omega_0) = 3 \sum_{\mathbf{k}} [\mathbf{n}_p \cdot (\mathbf{u}_{\mathbf{k}} \mathbf{u}_{\mathbf{k}}^*) \cdot \mathbf{n}_p] \delta(\omega_{\mathbf{k}} - \omega_0) \quad (4.14)$$

where  $\mathbf{u}_{\mathbf{k}}$  are the normal modes of electric field in a second quantization framework [128]. The presence of the delta function seems to introduce some singularities in the partial local density of states that are compensated by the normal modes whose magnitude tends to zero for a sufficiently large mode volume (for details [128]).

In order to establish a connection between the spontaneous emission of a two-level system with the classical theory of oscillating dipole, we need to introduce the concept of dyadic Green's function.

### 4.2.1 Spontaneous Emission: Dyadic Green's functions

Dyadic Green's functions  $\overleftrightarrow{\mathbf{G}}$  are defined as solutions of the equation <sup>3</sup>

$$\nabla \times \nabla \times \overleftrightarrow{\mathbf{G}}(\mathbf{r}, \mathbf{r}'; \omega) - k^2 \overleftrightarrow{\mathbf{G}}(\mathbf{r}, \mathbf{r}'; \omega) = \overleftrightarrow{\mathbf{I}} \delta(\mathbf{r} - \mathbf{r}') \quad (4.15)$$

---

<sup>3</sup>For further details see [133].

where the term “dyadic” means that (4.15) is a vectorial equation, *i.e.*  $\overleftrightarrow{\mathbf{G}}$  is a  $3 \times 3$  matrix or a tensor of rank 2. We can observe that (4.15) is very similar to the equation (4.2) that defines the complex amplitude of the electric field generated by a classical oscillating dipole. In order to establish a relation between the classical and the quantum treatment of the emission, we can expand  $\overleftrightarrow{\mathbf{G}}$  in terms of the normal modes of the electric field [128, 129, 133], obtaining

$$\overleftrightarrow{\mathbf{G}}(\mathbf{r}, \mathbf{r}'; \omega) = \sum_{\mathbf{k}} c^2 \frac{u_{\mathbf{k}}^*(\mathbf{r}', \omega_{\mathbf{k}}) u_{\mathbf{k}}(\mathbf{r}, \omega_{\mathbf{k}})}{\omega_{\mathbf{k}}^2 - \omega^2} \quad (4.16)$$

and, using the mathematical identity

$$\text{Im} \left\{ \lim_{\eta \rightarrow 0} \sum_{\mathbf{k}} \frac{u_{\mathbf{k}}^*(\mathbf{r}, \omega_{\mathbf{k}}) u_{\mathbf{k}}(\mathbf{r}, \omega_{\mathbf{k}})}{\omega_{\mathbf{k}}^2 - (\omega + i\eta)^2} \right\} = \frac{\pi}{2} \sum_{\mathbf{k}} \frac{1}{\omega_{\mathbf{k}}} u_{\mathbf{k}}^*(\mathbf{r}, \omega_{\mathbf{k}}) u_{\mathbf{k}}(\mathbf{r}, \omega_{\mathbf{k}}) \delta(\omega - \omega_{\mathbf{k}})$$

we can relate the imaginary part of Green’s dyadic with the partial local density of states:

$$\rho_p(\mathbf{r}_0, \omega_0) = \frac{6\omega_0}{\pi c^2} \left[ \mathbf{n}_p \cdot \text{Im} \left\{ \overleftrightarrow{\mathbf{G}}(\mathbf{r}_0, \mathbf{r}_0; \omega_0) \right\} \cdot \mathbf{n}_p \right] \quad (4.17)$$

This formula permits to evaluate the spontaneous decay rate  $\gamma$  of a two-level quantum system in an arbitrary reference system knowing its Green’s dyadic. The Green’s dyadic functions are evaluated at its origin (equation (4.17)), which corresponds to the location of the atomic system. From a classical viewpoint this is equivalent to the electric field previously emitted by the quantum system and now arriving back at its origin.

Using the relation [128, 133]

$$\mathbf{E}(\mathbf{r}) = \omega^2 \mu \mu_0 \overleftrightarrow{\mathbf{G}}(\mathbf{r}, \mathbf{r}_0) \mathbf{p}$$

the dissipated power of a classical oscillating dipole (equation (4.11)) can be also re-written in terms of  $\overleftrightarrow{\mathbf{G}}$ :

$$\frac{dW}{dt} = \frac{\omega}{2} \text{Im}[\mathbf{p}^* \cdot \mathbf{E}(\mathbf{r}_0)] = \frac{\omega^3 |\mathbf{p}|^2}{2c^2 \epsilon \epsilon_0} \left[ \mathbf{n}_p \cdot \text{Im} \left\{ \overleftrightarrow{\mathbf{G}}(\mathbf{r}_0, \mathbf{r}_0; \omega) \right\} \cdot \mathbf{n}_p \right] \quad (4.18)$$

The mathematical analogy between the quantum and the classical description is evident comparing equation (4.17) and equation (4.18):

$$\begin{aligned} \frac{dW}{dt} \equiv P &= \frac{\pi \omega_0^2 |\mathbf{p}|^2}{12 \epsilon \epsilon_0} \rho_p(\mathbf{r}_0, \omega_0) \\ &= \frac{P_0}{\epsilon} \frac{\rho_p(\mathbf{r}_0, \omega_0)}{\rho_p^{(0)}(\omega_0)} \end{aligned} \quad (4.19)$$

where  $P_0 = \omega_0^4 |\mathbf{p}|^2 / 12\pi c^3 \epsilon_0$  and  $\rho_p^{(0)}(\omega_0) = \pi^2 c^3 / \omega_0^2$  are the average radiated power and the partial local density of states<sup>4</sup> in the free space, respectively.  $\epsilon$  is the relative dielectric constant,  $\mathbf{r}_0$  identifies the emitter's position while  $\omega_0$  is the emission frequency. The equation (4.19) allows us to evaluate the normalized partial local density of states by computing the normalized time average radiated power generated by an infinitesimal dipole<sup>5</sup>. The partial local density of states is equivalent to the power radiated by the dipole, which is a measure of how much the harmonic modes of a system overlap with the source point, *i.e.* the same current radiates a different amount of power depending on the surrounding geometry. The spontaneous decay rate is proportional to the partial local density of states, which depends on the power dissipated by a classical oscillating dipole. This explains why a change in the environment can modify the spontaneous decay rate  $\gamma$ .

The total local density of states (LDOS) is evaluated from equation (4.14) performing an average over the various orientations of the dipole. In an isotropic and homogeneous medium

$$\langle \mathbf{n}_p \cdot \text{Im} \left\{ \overleftrightarrow{\mathbf{G}}(\mathbf{r}_0, \mathbf{r}_0; \omega_0) \right\} \cdot \mathbf{n}_p \rangle = \frac{1}{3} \text{Im} \left\{ \text{Tr}[\overleftrightarrow{\mathbf{G}}(\mathbf{r}_0, \mathbf{r}_0; \omega_0)] \right\}$$

where  $\text{Tr}[\dots]$  is the trace of the tensor in the brackets. The LDOS counts the available number of electromagnetic modes in which photons can be emitted at the specific location of the emitter, and can be interpreted as vacuum fluctuations. The LDOS and, hence, the emission rate depend on the emission frequency  $\omega$  and on the emitter position, but not on the emission direction.

---

<sup>4</sup>The partial local density of states is equivalent to the local density of states (LDOS) in the free space.

<sup>5</sup>Normalized with respect to their respective quantities in the free space.

## 4.3 LDOS modification

The possibility of modifying the spontaneous emission rate by changing the environment was first pointed out by Purcell in 1946, for resonant atomic transition at radiofrequencies [134]. Nowadays, there are many efforts to control the emission rate of quantum emitters by optimizing the nanoscale environment *e.g.* by microcavities [135–137], photonics crystals [138, 139], plasmonic nanoantennae [140–142], or reflecting interface [127, 143, 144]. The control of the spontaneous emission is relevant to applications, including single-photon source for quantum information, light-emitting diode, and solar harvesting [145–147].

In the next sections, we will focus on the LDOS alteration induced by emitters located at the interface between two different materials. We will present some details about the radiation pattern of a vertical infinitesimal electric dipole located on the interface between two dielectric half spaces. Two different studies will be performed. Firstly, we will analyze the LDOS modification induced by a change of the materials in the bottom half space. Secondly, the effect of the emitter position on the radiated power will be discussed. Both analysis are fundamental to understand a more complex situation in which we will consider a random array of 100 electric dipoles placed within different multilayer systems to explain the experimental results of Chapter 3 in terms of Purcell’s effect.

### 4.3.1 Radiation pattern of interfacial vertical dipole

It is well known that the presence of an interface near emitting atoms (represented by oscillating electric dipoles) introduces important changes in their radiation. Indeed, when an atom is located near the boundary of a dielectric or metallic medium, part of the radiation will be reflected at the interface, leading to constructive or destructive interference with the radiation emitted directly by the atom towards a detector in the far field. Therefore, LDOS is modified due to interference of the emitted and reflected light. For example, the influence of the interface on the emitted lifetime has been studied extensively. It was found that the interface enhances the energy transfer of the radiating dipole, which results in a shortening of the emission lifetime [148, 149].

In order to analyze in details this effect, we studied the LDOS modification induced by an infinitesimal vertical dipole ( $\mathbf{n}_p = \mathbf{e}_z$ ) located at the interface between

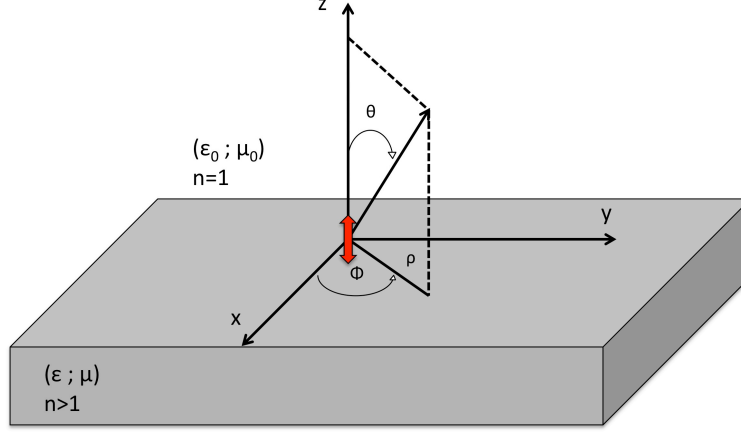


**Figure 4.3:** Infinitesimal vertical electric dipole located at the interface of two different materials. The dielectric constant of the upper ( $z > 0$ ) and lower ( $z < 0$ ) half space are  $\epsilon_0$  and  $\epsilon$  which is greater than  $\epsilon_0$ .

two different materials (see Fig.4.3). As show in section 4.1, we can evaluate the emitted power using the electric Hertz vector  $\mathbf{\Pi}$ . The formalism described in section 4.1 can be easily applied to study the characteristic of a dipole near an interface. The only difference is represented by the boundary conditions on  $\mathbf{\Pi}$  to relate the electromagnetic fields in the upper half space with the fields in the lower half space and vice versa. Using Sommerfeld's method [130], we can see that  $\mathbf{\Pi}_z$  is the only component that is necessary when the dipole is vertically located at the separation interface. The boundary conditions along the plane  $z = 0$  are

$$\Pi_{1z} = n^2 \Pi_{2z} \quad (4.20)$$

$$\partial \Pi_{1z} / \partial z = \partial \Pi_{2z} / \partial z \quad (4.21)$$

where  $\Pi_{1z}$  and  $\Pi_{2z}$  are the  $z$ -component of the Hertz vector in the upper ( $z > 0$ ) and lower media ( $z < 0$ ) respectively, while  $n$  indicates the refractive index of the lower half space (see Fig.4.3). Thus the problem is reduced to find the solution of equation (4.5) that gives outgoing spherical waves in the far zone and that satisfies the boundary conditions (4.20) and (4.21) along the plane  $z = 0$ . Knowing the electric and magnetic field in both half spaces, we can evaluate the Poynting vector  $\mathbf{S}$  by using the relation

$$S_r = \frac{1}{2} \text{Re}[E_\theta H_\phi^*]$$

obtaining [127]:

- for the upper half space ( $k_0 r \rightarrow \infty$ ,  $0 \leq \theta \leq \pi/2$ );

$$S_{r1} = \frac{I_0^2}{8\pi^2} \left( \frac{\mu_0}{\epsilon_0} \right)^{1/2} \frac{n^4 k_0^2 \sin^2 \theta \cos^2 \theta}{[n^2 \cos \theta + (n^2 - \sin^2 \theta)^{1/2}]^2} \frac{1}{r^2} \quad (4.22)$$

- for the lower half space ( $k_0 r \rightarrow \infty$ ,  $\pi - \theta_c \leq \theta \leq \pi$ )

$$S_{r2} = \frac{I_0^2}{8\pi^2} \left( \frac{\mu_0}{\epsilon_0} \right)^{1/2} \frac{n^5 k_0^2 \sin^2 \theta \cos^2 \theta}{[n(1 - n^2 \sin^2 \theta)^{1/2} - \cos \theta]^2} \frac{1}{r^2} \quad (4.23)$$

- for the lower half space ( $k_0 r \rightarrow \infty$ ,  $\pi/2 \leq \theta \leq \pi - \theta_c$ )

$$S_{r2} = \frac{I_0^2}{8\pi^2} \left( \frac{\mu_0}{\epsilon_0} \right)^{1/2} \frac{n^5 k_0^2 \sin^2 \theta \cos^2 \theta}{n^2(n^2 \sin^2 \theta - 1) + \cos^2 \theta} \frac{1}{r^2} \quad (4.24)$$

where  $\theta_c = \arcsin(n_{upper}/n_{lower})$  is the critical angle. If the incidence angle of the emitted plane wave exceeds  $\theta_c$ , then the transmitted wave in the substrate becomes evanescent, *i.e.* these waves die out exponentially in the negative z-direction, and do not contribute to the radiated power.

We simulated the radiation pattern of a vertical infinitesimal electric dipole using Comsol multiphysics [150] in which the equations (4.22), (4.23) and (4.24) are implemented. Fig.4.4 shows  $S_r$  as a function of  $\theta$  when we place the emitter in different environments<sup>6</sup>. We fixed the position of the emitter (center of the simulation plane), the emission wavelength at 800 nm, and the material of the upper half space while we changed the refractive index of the lower medium from 1 (free space) to 3 ( $\sim$  silicon). The Poynting vector is zero at the interface ( $\theta = \pi/2$ ) and along the dipole axis ( $\theta = 0$  and  $\theta = \pi$ ) in all configurations (see Fig.4.4). The maxima of the radiation pattern in the upper half space increase as  $n$  increases from 1 to 3. In the lower half space ( $\pi/2 \leq \theta \leq \pi$ ), the maxima of  $S_{r2}$  lie along the conical angle  $\theta = \pi - \theta_c$ , and the angle  $\theta_c$  decreases as  $n$  increases, *i.e.* the pattern becomes highly directional. Fig.4.4 c and Fig.4.4 d show the reflection effects of the emitted radiation with the interface. These interference effects create additive emission pattern and the number of these new lobes increases with respect to the refractive index  $n$ .

Fig.4.5 a and Fig.4.5 b display the normalized emitted power into the upper ( $P_1$ ) and lower ( $P_2$ ) half space respectively. Normalized means with respect to  $P_0 = |\mathbf{p}|^2 \omega_0^4 / 12\pi \epsilon_0 c^3$  which represents the time average power in the free space. As

<sup>6</sup> $S_r$  does not depend on  $\phi$  due to the symmetry of the configuration.

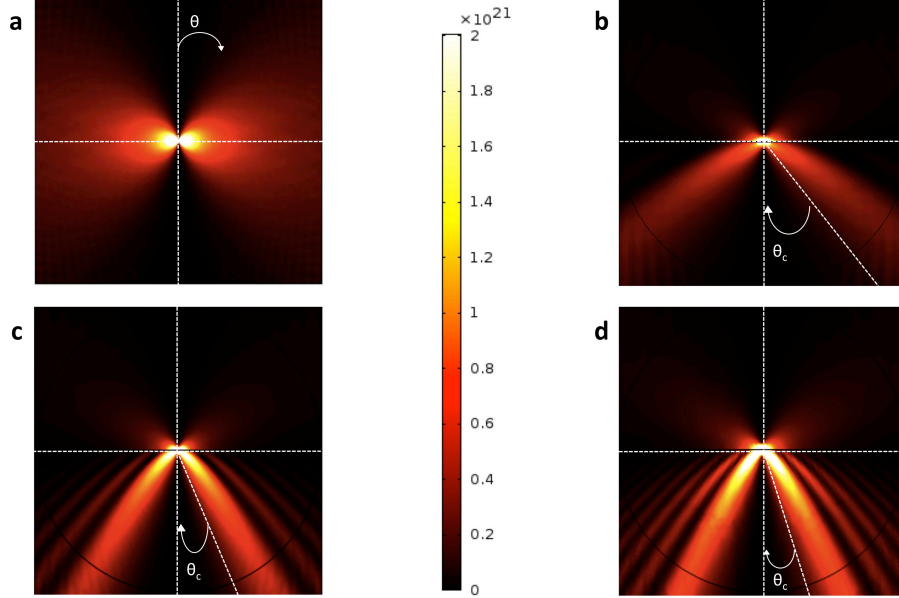


**Figure 4.4:** Radiation pattern of a vertical electric dipole placed in different environments. We fixed the position of the emitter (center of the simulation plane), the emission wavelength at 800 nm, and the refractive index of the upper medium to 1 while we changed the refractive index of the lower half space. a) free space; b)  $n_{lower} = 1.5$ ; c)  $n_{lower} = 2.5$ ; d)  $n_{lower} = 3$ . The critical angle  $\theta_c$  decreases when  $n_{lower}$  increases.

$n$  approaches to 1,  $P_1$  and  $P_2$  reach the value  $P_0/2$ : in vacuum the emitted radiation is equally distributed. As  $n$  increases,  $P_1$  first is almost constant and then increases reaching  $P_0$  for  $n$  almost equal to 5. On the other hand,  $P_2$  smoothly increases and becomes  $2P_0$  just for  $n = 2$ . A vertical dipole placed at the interface emits more radiation into the material with high refractive index because there are more available optical states that can be occupied by photons.

As discussed in subsection 2.2.2, the radiative and non radiative contributions to the total decay rate can be separated by placing quantum dots (QDs) at different distances from an interface, since only the radiative component varies with the distance. Here, we can relate the measured oscillations of the total decay rates (see Fig.2.10) with the modification of the partial local density of states.

For sake of simplicity, let consider a situation in which we change the distance of the emitter from the interface between free space ( $n_{upper} = 1$ ) and a high-refractive index material ( $n_{lower} = 1.5$ ). The emitter is described as a vertical electric dipole with an emission wavelength of 800 nm. Fig.4.6 shows the change in the emission

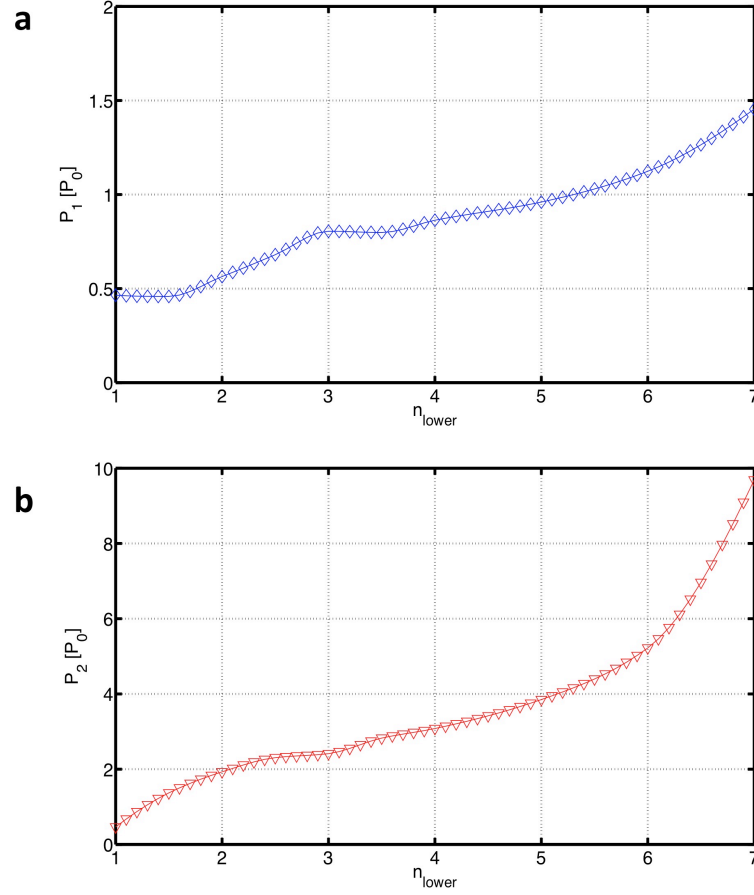


**Figure 4.5:** Power emitted by a vertical dipole ( $\lambda_0 = 800$  nm) radiated into the upper half-space (a) and lower half space (b) as a function of the refractive index of the lower material. The power is normalized to the power emitted by the same dipole in the free space (Fig.4.4 a).

when the dipole is placed at 150 nm (Fig.4.6 a), 250 nm (Fig.4.6 b),  $-150$  nm (Fig.4.6 c), and  $-250$  nm (Fig.4.6 d) from the interface. The emission pattern depends on the emitter's position. Indeed, the emitted light from a dipole in the upper half space goes from a medium with low to a material with high refractive index. Therefore, the interference between the emitted and reflected light is reduced due to Snell's law. On the other hand, the emitted radiation travels from a medium with a higher refractive index to the one with a lower refractive index when the dipole is located in the upper half space. In this case, the critical angle ( $\theta_c$ ) is small, *i.e.* the total internal reflections increased. Indeed, the transmitted radiation in the upper half space is very small when the dipole is located in the lower media

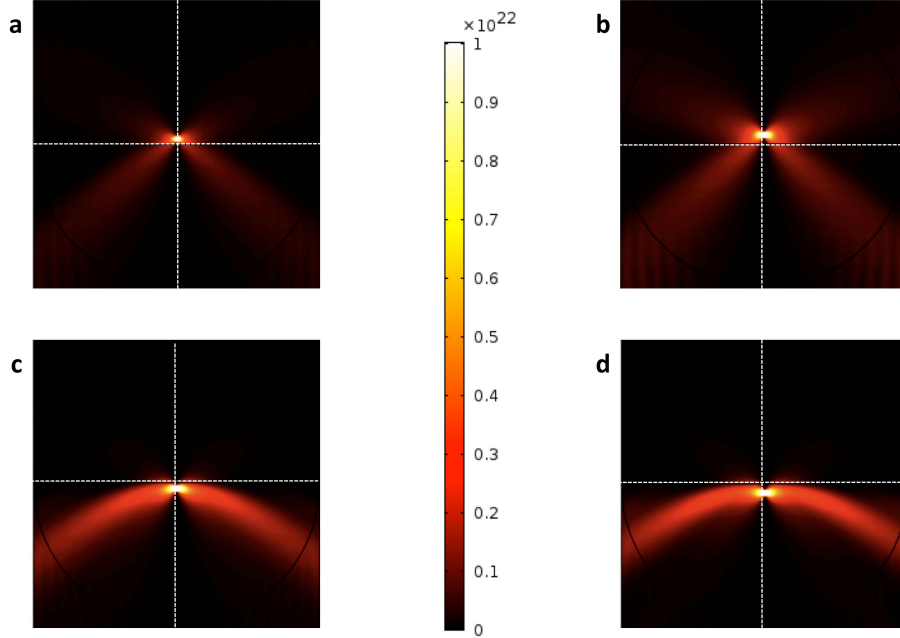


**Figure 4.6:** Poynting vector of a vertical electric dipole located at different distances from the interface: a)  $t = 150\text{nm}$ , b)  $t = 250\text{nm}$ , c)  $t = -150\text{nm}$ , d)  $t = -250\text{nm}$ . The emission patterns are completely different changing the position of the emitter due to the reflection effects.

(Fig.4.6 c and Fig.4.6 d). Using the equation (4.18), we can relate the normalized partial local density of states to the normalized time-average power:

$$\frac{\rho_p(\mathbf{r}_0, \omega_0)}{\rho_p^{(0)}(\omega_0)} = \epsilon \frac{P}{P_0} \quad (4.25)$$

where  $\epsilon$  is the relative dielectric constant of the material in which the dipole is located. This relation permits to evaluate the partial local density of states by computing the emitted power. The results of this study is summarized in the Fig.4.7. We moved the emitter vertically, from the center of the simulation plane, through the upper and lower half space (inset of the Fig.4.7). The “negative position” identifies the lower half medium. At the interface ( $t = 0\text{ nm}$ ),  $\rho_p \simeq 2\rho^{(0)}$ . Indeed, the image dipole of an emitter oriented perpendicular to the interface is added to the dipole itself, giving almost doubling of  $\rho_0$  [130]. Increasing the dipole distance in the upper half space,  $\rho_p$  decreases smoothly and becomes  $\rho^{(0)}$  for  $t = 200\text{ nm}$ , *i.e.* at  $\lambda_{\text{emission}}/4$ . Further away from the interface, oscillations occur due to the interference between the emitted and the reflected light. These oscillations are more evident in the lower half space. Indeed,  $\rho_p/\rho^{(0)}$  increases very fast and reaches its maximum value around

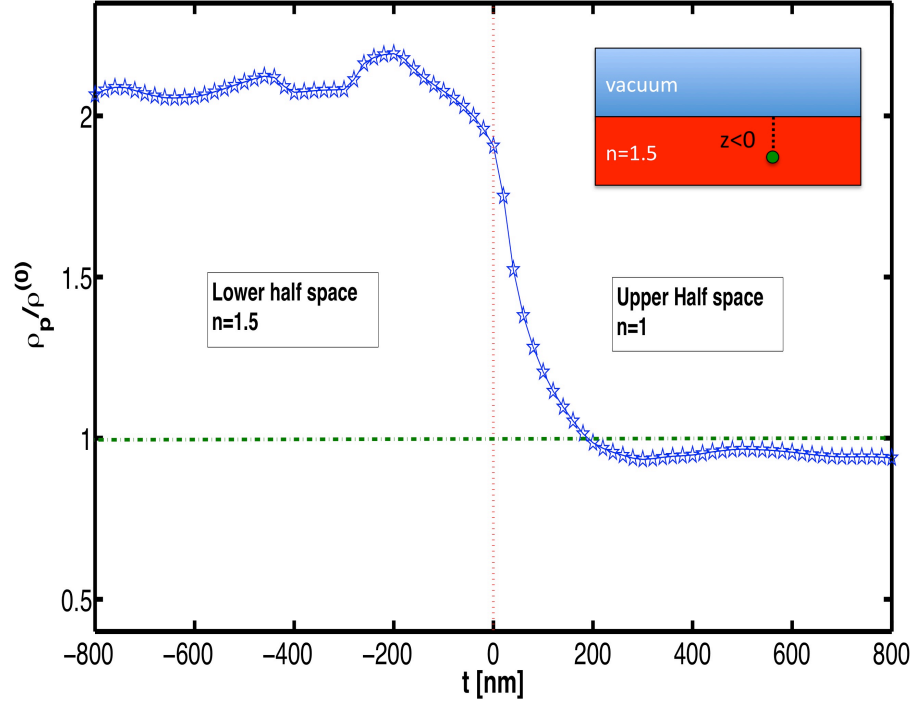


**Figure 4.7:** Normalized partial local density of states as a function of the emitter distance from an interface between free space (upper half space) and a high refractive index material ( $n = 1.5$  lower half space). The normalization is taken with respect to LDOS of the same emitter placed in the free space.

200 nm. The distance between the abscissas of two consecutive extrema in the lower half space is  $\sim \lambda_{emission} / (2n_{lower}) \simeq 260$  nm. This corresponds to the interference between the emitted radiation and the radiation which is reflected by the interface in the lower medium. Further increasing the distance, these interference effects are not longer sufficiently strong to modify the partial local density of states resulting in constant values in both half spaces. Interferences between the emitted and reflected light are responsible of the oscillations in the normalized partial local density of states changing the position of the emitter.

## 4.4 Quantum dots emission: validity of the dipole approximation.

As pointed out in the previous sections, the radiative decay rates can be evaluated using Fermi's golden rule in the weak-coupling regime. Moreover, it is possible to connect the partial local density of states with the power emitted by an oscillating electric dipole and in this way to analyze the modification of the LDOS produced by different environments. At this stage, the next step is to understand if we can describe the emission pattern of quantum dots (QDs) using electric oscillating dipoles. In other words, we need to analyze the range of validity of the dipole approximation.

As discussed in sections 1.2 and 1.5, semiconductor QDs are materials in which the electron motion is confined in all spatial directions. This confinement gives rise to a discrete energy spectrum for the electrons similar to that of atoms; hence the term artificial atoms is often used to refer to quantum dots, even if they actually consist of thousands, or even ten thousands atoms [151]. This discrete energy spectrum yields sharp emission lines for optical transitions between excited and ground states. As a consequence, the width of the emission may be much smaller than the thermal energy  $k_B T$ <sup>7</sup>. Indeed, this has been observed for nanocrystals of direct band gap semiconductor material of the type II-VI [152]. In certain circumstances, QDs can be described in the same way as atomic photon emitter, *i.e.* as point sources whose wavefunctions spatial extent can be disregarded. However, there are situations in which this assumption is not valid. Indeed, the usual criterion for the validity of the dipole approximation (DA) is that the product of the length of the optical wave vector  $\mathbf{k}$  and the spatial extent of the emitter  $d$  must be much smaller than one (see for example [153]):

$$|\mathbf{k}|d \ll 1 \quad (4.26)$$

This criterion is not sufficient to ensure the validity of DA in the case of QDs. Recently, a large deviation from DA was observed [154, 155]. In [154], QDs (volume  $20 \times 20 \times 6 \text{ nm}^3$ ) of indium arsenide embedded in gallium arsenide (GaAs) coupled with plasmonic nanostructures display decay rates that deviate significantly from the point-dipole theory for short distances from the silver mirror proving the breakdown of the point-emitter description. For QDs, there are four situations that can lead to the breakdown of DA [156]:

---

<sup>7</sup> $k_B$  is the Boltzmann constant and  $T$  the temperature.

- QDs embedded in semiconductors with a high refractive index as, for example, GaAs ( $n \approx 3.5$ ) which increases  $\mathbf{k}$ ,
- QDs with a lateral size of 100 nm [157],
- the equation (4.26) is valid for homogeneous media. In inhomogeneous material, the field can be expanded in terms of plane waves, *i.e.* there is not a unique  $\mathbf{k}$  for which we can evaluate the criteria (4.26)
- the asymmetry nature of the exciton wave functions can enhance the finite size of the QDs.

In our case, QDs are silicon nanocrystals (Si-NCs) embedded in silicon dioxide matrix ( $n_{SiO_2} \sim 1.4$ ) deposited using PECVD technique or colloidal Si-NCs dispersed in a glycerol suspension ( $n_{gly} \sim 1.45$ ). The refractive index of the host matrix is low and the dimension of nanoparticles vary from  $\sim 2$  nm to  $\sim 5$  nm. Fig.4.8 displays the normalized<sup>8</sup> emission spectra as a function of the energy in eV of the used samples. These spectra are consistent with previously reported silicon nanocrystals photoluminescence (PL) results. It is well established that the

<sup>8</sup>Normalized with respect to their maximum value.

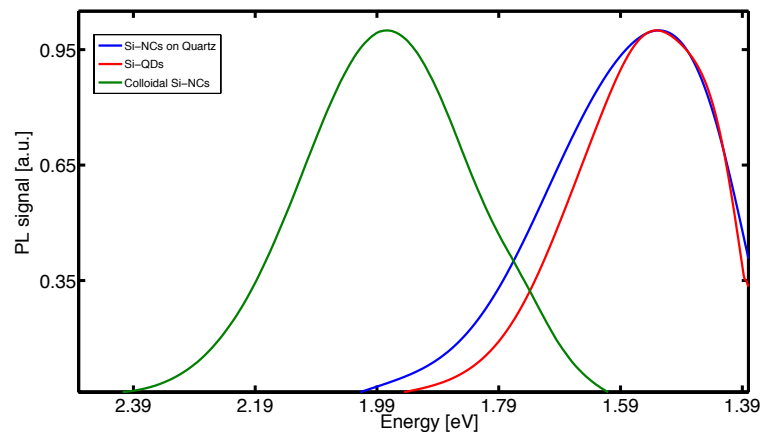


**Figure 4.8:** Normalized Photoluminescence spectra for silicon nanocrystals fabricated during our collaboration within Lima's project. The blue and red curves are more or less the same and express the emission spectra of Si-NCs growth with PECVD technique. In more details, the blue refers to the Si-NCs growth on Quartz  $500\mu\text{m}$  thick while the red to Si-NCs on an interdigitated back contact silicon solar cell. The green line refers to the emission spectrum produced by colloidal Si-NCs dispersed in a glycerol solution.

characteristic near-infrared photoluminescence, typically observed in the range from  $\sim 650\text{nm}$  to  $\sim 950\text{nm}$ , originates from the band-to-band recombination of quantum confined excitons [81, 158], *i.e.* as in the case of a two-level system. However, the PL band of Si-NCs is not sharp but it is very broad, as can be seen in Fig.4.8. Even at low temperatures, there is no significant narrowing of the emission bandwidth [29]. This suggests that this large width is due to inhomogeneous broadening. However, narrow emission line with a full half width maximum of  $2 - 2.3\text{meV}$  was observed for a single Si quantum dot at low temperature ( $\sim 35\text{ K}$ ) [159]. The emission line width of Si-NCs can be as sharp as for direct band gap material quantum dots confirming the atomic like nature of these low-dimensional entities. The broadening observed for Si nanocrystals ensembles is just due to size and shape distribution. Therefore, the emission from Si-NCs is an incoherent emission because it is generated by atom-like sources that emit at different frequencies. In other words, our emitters, characterized by different size, can be simulated as an “ensemble” of two level quantum system (as an array of oscillating electric dipoles) with different energy gaps (with different emission frequencies  $\omega_0$ ).

In optics, one usually deals with a source which emits light within a frequency range. The source may be regarded as arising from a large number of harmonic oscillators whose frequencies fall within this range. In order to obtain the intensity at a general point P, we must sum the individual fields generated by each oscillator (elements of the source) [92]:

$$\mathbf{E} = \sum_j \mathbf{E}_j \qquad \mathbf{H} = \sum_j \mathbf{H}_j \qquad (4.27)$$

where  $j$  expresses the number of the emitters. The intensity at the point P is then given by

$$\begin{aligned} I(P) = \langle |\mathbf{S}| \rangle &= | \langle \mathbf{E} \times \mathbf{H} \rangle | \\ &= \left| \sum_j \langle \mathbf{E}_j \times \mathbf{H}_j \rangle + \sum_{j \neq j'} \langle \mathbf{E}_j \times \mathbf{H}_{j'} \rangle \right| \end{aligned} \qquad (4.28)$$

The second term in equation (4.28) expresses interference phenomena. If the two beams are originated from the same source, their fluctuations are in general correlated, and the emission is called coherent. Conversely, the fluctuations are completely uncorrelated, and the beams are said to be incoherent, if they are generated

by different sources [92]. When such beams produced by different sources are superposed, no interference is observed. The total intensity ( $I$ ) is everywhere given by the sum of the intensities of the individual beams.

In conclusion, the criterion (4.26) is satisfied for Si-NCs, *i.e.* we can describe the Si-NCs emission as generated by an array of electric oscillating dipoles. Moreover, due to the incoherent nature of their emission, we can evaluate the intensity produced by the single dipoles and then take their sum neglecting the interaction term.

#### 4.4.1 Si-NCs as oscillating electric dipoles.

We considered different multilayer systems characterized by an array of 100 electric dipoles as active layer. The number of dipoles was chosen arbitrarily. These emitters act as a density current which is given by the sum of the single-dipole contributions:

$$\begin{aligned} \mathbf{j}(\mathbf{r}, t) &= \sum_k \mathbf{j}_k \\ &= \sum_k \mathbf{p}_k \delta(\mathbf{r} - \mathbf{r}_k) e^{-i(\omega_k t + \phi_k(t))} \end{aligned} \quad (4.29)$$

where  $\mathbf{p}_k = I_k \mathbf{n}_k$  is the dipole moment,  $\mathbf{r}_k$  identifies the position of the single emitter,  $\omega_k$  is the emission frequency, and  $\phi_k(t)$  expresses the oscillating phase as a function of the time  $t$ . In order to take into account all the features of the Si-NCs emission, we generated a random distribution of electric dipoles. This means that the emitters are characterized by

- random locations and orientations:  $\mathbf{r}_k$  and  $\mathbf{n}_k$  are generated using an uniformly distributed pseudorandom numbers for both the x and y component,
- random phases that evolve in time,
- different emission frequencies:  $\omega_k$  are chosen in a closed interval depending on the considered emitters (see Fig.4.8)

In this way, this ensemble of electric dipoles generates an incoherent emission that can be associated to the ones of the Si-NCs.

**Table 4.1:** Simulation details of the studied multilayered structures.

	Structure	Height	Width	Emission Range
Lima Configuration (G2A)	Air	$2\mu\text{m}$	$4\mu\text{m}$	
	Quartz	55nm	$4\mu\text{m}$	
	Si-QDs	65nm	$4\mu\text{m}$	[795nm,805nm]
	Si	$2\mu\text{m}$	$4\mu\text{m}$	
Colloidal Si-NCs Configuration	Quartz	$5\mu\text{m}$	$10\mu\text{m}$	
	Colloidal Si-NCs	500nm	$10\mu\text{m}$	[620nm,650nm]
	Si	$5\mu\text{m}$	$10\mu\text{m}$	
Air Configuration	Quartz	$6\mu\text{m}$	$10\mu\text{m}$	
	Si-NCs on Quartz	130nm	$10\mu\text{m}$	[790nm,810nm]
	Air	$6\mu\text{m}$	$10\mu\text{m}$	
Glycerol Configuration	Quartz	$6\mu\text{m}$	$10\mu\text{m}$	
	Si-NCs on Quartz	130nm	$10\mu\text{m}$	[790nm,810nm]
RIML Configuration	Glycerol	$6\mu\text{m}$	$10\mu\text{m}$	
	Quartz	$6\mu\text{m}$	$10\mu\text{m}$	
	Si-NCs on Quartz	130nm	$10\mu\text{m}$	[790nm,810nm]
	RIML	$6\mu\text{m}$	$10\mu\text{m}$	

#### 4.4.2 Simulated Structures

In order to simulate the multilayered structures presented in Chapter 2 and 3, we used the software package MatLab [160] and the Comsol software tool [150]. The MatLab code generates a two-dimension simulation environment that we analyze, via SimuLink connection, with Comsol multiphysics. Comsol multiphysics software is based on the finite element method (FEM). FEM is a numerical technique for finding approximate solutions of partial differential equations as well as of integral equations. It is a method for dividing up a very complicated problem into small elements that can be solved in relation to each other. One of the main motivations in applying the FEM for solving light propagation problems is the ability to use arbitrary geometries. After the definition of a geometry, a mesh is created. The accuracy of the FEM solution depends on the mesh quality, *i.e.* the mesh should have a high resolution around sources and also around detectors.

We simulated five different multilayered structures called lima, air, glycerol, refractive index liquid matching (RIML), and colloidal Si-NCs configurations (see Table.4.1). These multilayered structures correspond to the different solar cell schemes studied in Chapter 2 and 3. The composition and details of the simulated

structures are summarized in Table 4.1. The heights of the active layers correspond to the real dimensions of the fabricated devices. However, in the case of colloidal Si-NCs in glycerol solution this parameter was reduced from  $\approx 200 \mu\text{m}$  (effective thickness of the cover/IBC spacing layer) to 500 nm to decrease the computational time. The widths and the heights of the others materials was chosen arbitrarily. The different emission ranges were chosen considering the different emission profiles of silicon nanoparticles, as shown in Fig.4.8.

The MatLab code defines the simulation environment specifying all the characteristics summarized in Table.4.1. Moreover, the source in the Maxwell's equation, resolved by using Comsol, is formed by an ensemble of electric oscillating dipoles which are also implemented in the MatLab script with the relative features summarized in equation (4.29). Fig.4.9 shows an example of the simulation environment produced by this script. The active layer contains the random electric dipoles described as point-like sources. Their positions are arbitrary and change from one simulation to another as well as the others parameters specified in the previous section. In order to avoid edge effects, we decided to locate the emitters far away from the borders of the simulation plane. Moreover, we assumed scattering boundary

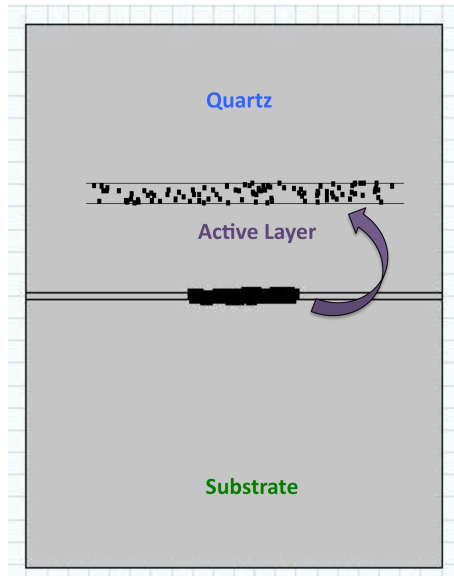


**Figure 4.9:** Example of the simulated structures produced by the MatLab script. The arrow shows a zoom of the active layer formed by electric oscillating dipoles. Their positions is arbitrary and change from one simulation to another as well as their orientations, emission frequencies, and phases.

conditions to circumvent reflection effects of the emitted light with the edges of the simulation plane, *i.e.* all the emitted waves generated by oscillating dipoles do not interfere with the edges of the simulation plane. We used the transient interface to compute the time dependence of the emitted radiation. The use of this interface permits us to simulate a situation in which the single sources emit with different frequencies ensuring an incoherent emission. In order to check this assumption, we have calculated the intensity produced by two point-like sources and we found that the total intensity was given by the sum of the single contributions without the interference term (second term in equation (4.28)).

#### 4.4.3 Simulation Results.

Fig.4.10 and Fig.4.11 display snapshots of the radiation pattern generated by randomly distributed electric dipoles and placed in different environments (details in Table4.1). As expected, different environments produce different emission patterns. However, all these snapshots show radiated light with spherical symmetry in both the upper and lower half space, far away from the sources. Indeed, the electric Hertz vector  $\mathbf{\Pi}(\mathbf{r})$  behaves as an outgoing spherical wave with an angular dependent

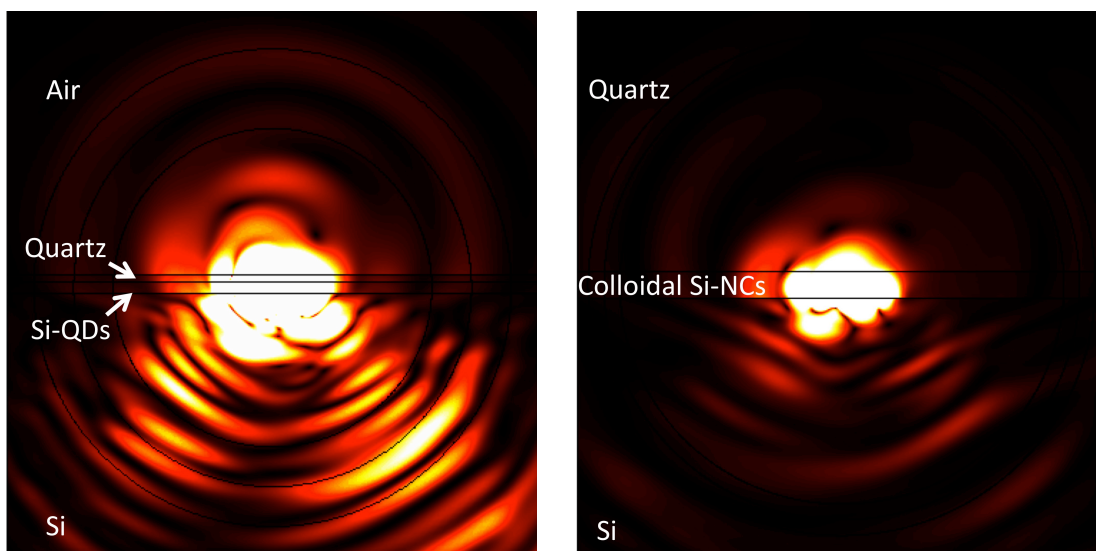


**Figure 4.10:** Emission patterns produced by randomly distributed electric oscillating dipole in the lima (left side) and colloidal Si-NCs in glycerol (right side) configuration.

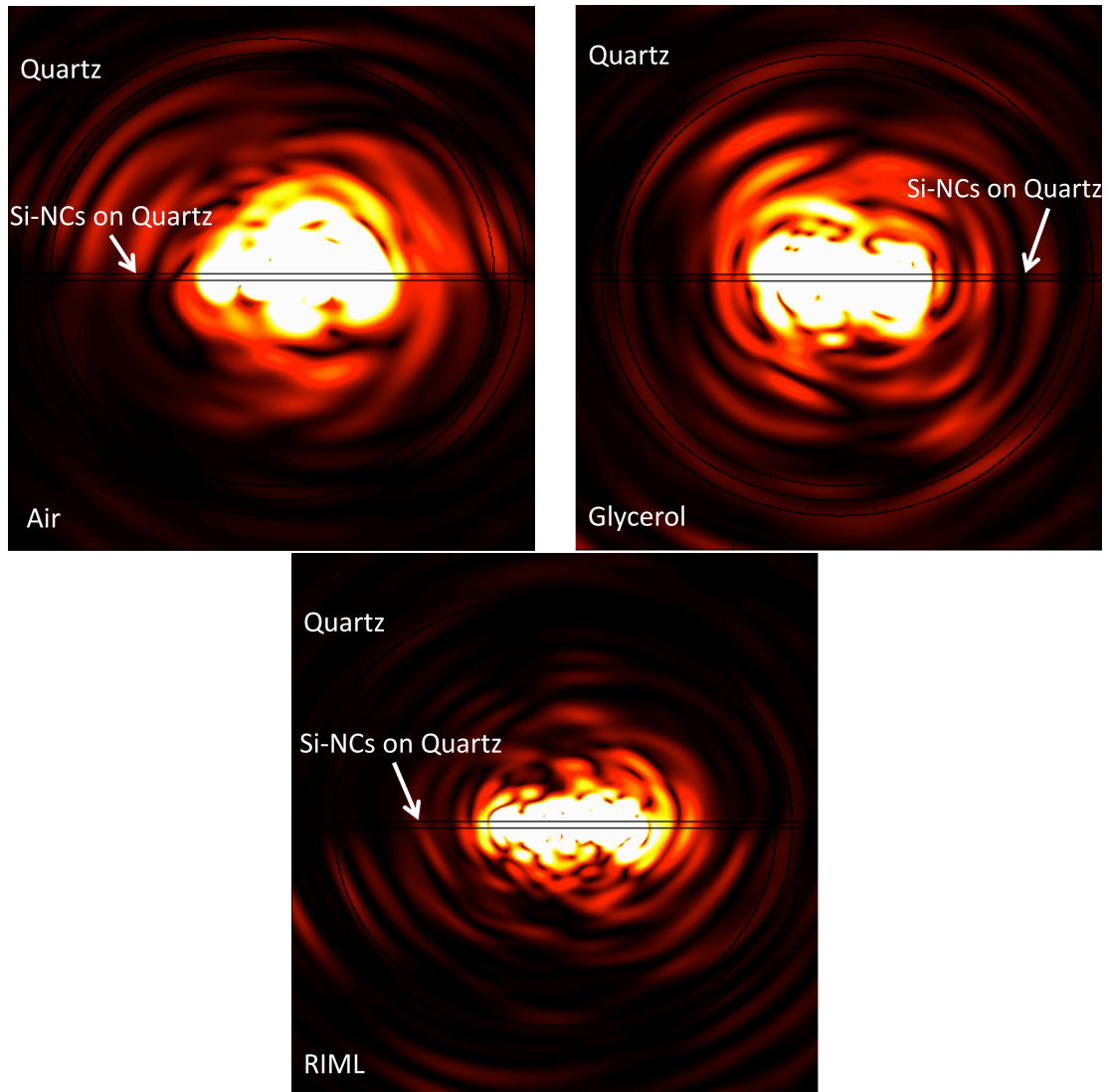


**Figure 4.11:** Poynting vector generated by Si-NCs deposited on a quartz substrate located in different environments: air, glycerol, and RIML “liquid” in the cover/IBC spacing layer (see Table.4.1).

coefficient in the far zone, as explained in section 4.1. Fig.4.10 shows the radiated power in the “lima” (left-side) and “colloidal Si-NCs” (right-side) configuration. In both cases, the radiation pattern is directed more towards the silicon substrate. On the contrary, Fig.4.11 display how change the Poynting vector through different configurations:

- air: the emission is directed principally towards the top half space,
- glycerol: the emission is practically isotropically directed,
- RIML: the radiation pattern is directed especially towards the bottom material.

As pointed out in subsection 3.2.1, the emitted light directions depends on the environment. These simulations validate this statement.

The radiated powers as a function of the “simulation time” are shown in Fig.4.12 and Fig.4.13. The blue, red, and green curves refer to the normalized emitted power<sup>9</sup> towards the top, the lateral, and bottom of the simulation plane, respectively. These

<sup>9</sup>Normalized with respect to the total radiated power.

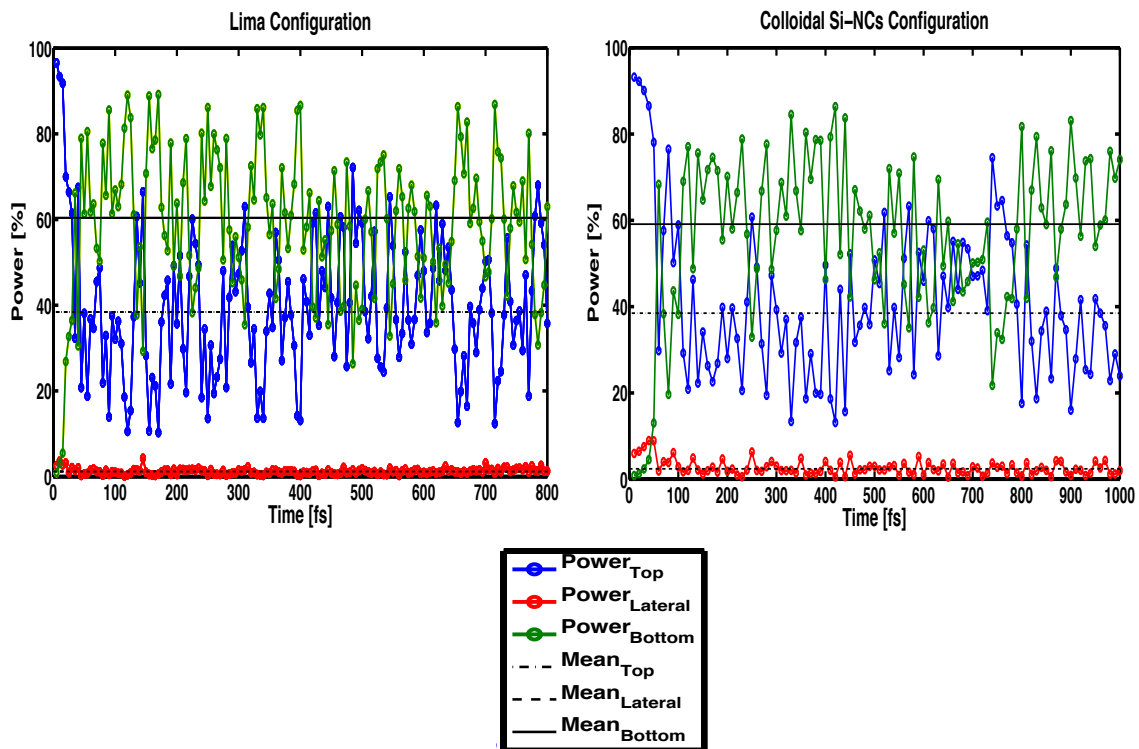


**Figure 4.12:** Radiated power as a function of the simulation time computed for the lima (left-side) and colloidal Si-NCs (right-side) configuration. The blue, red, and green curves refer to the radiated power into the top, lateral, and bottom zone of circles containing the detectors, respectively. The drawn lines indicate time-averaged quantities evaluated starting after the transient time.

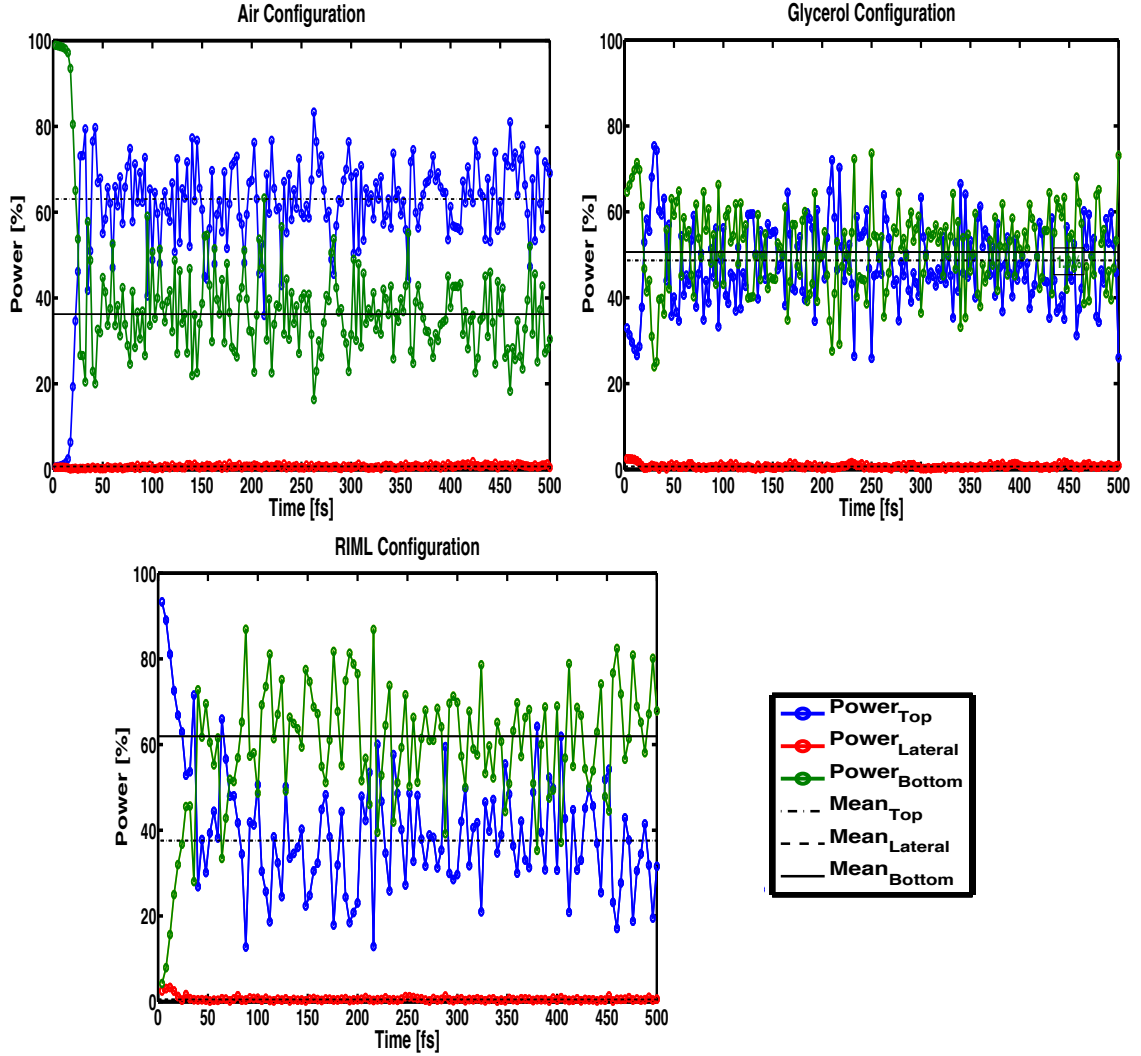


**Figure 4.13:** Radiated power as a function of the simulation time computed for the Air (left-side), Glycerol (right-side), and RIML (bottom) configuration. The blue, red, and green curves refer to the radiated power into the top, lateral, and bottom zone of circles containing the detectors, respectively. The drawn lines express time average emitted powers evaluated starting after the transient time.

fractions are evaluated with respect to detectors located far away from the source. In order to compute this analysis we used the equation

$$P_{zone}(t) = \frac{\int \mathbf{S}_{zone}(t) \cdot \mathbf{n}_{zone} dA}{\int \mathbf{S}_{total}(t) \cdot \mathbf{n}_{total} dA} \quad (4.30)$$

	Silicon <sup>✓</sup>		Silicon <sup>*</sup>		Air		Glycerol		RIML	
	n	%	n	%	n	%	n	%	n	%
<b>Quartz</b>	1.4	38.8±0.5	1.4	38.7±1	1.4	60.7±2.5	1.4	48.4±0.2	1.4	40.5±2.2
<b>Active layer</b>	1.8	1.2±0.1	1.43	2.5±0.2	1.7	0.5±0.1	1.7	0.8±0.1	1.7	0.5±0.04
<b>Substrate</b>	3.7	60±0.5	3.88	58.8±1	1	38.8±2.6	1.43	50.8±0.1	1.75	59±2.2

✓In the Lima Configuration, the top layer is formed by Air and Quartz. Here, we neglect air to make the table more clear.

\* Active layer is composed by colloidal Si-NCs in glycerol solution. The value of the refractive indexes  $n$  is taken at 630nm

**Figure 4.14:** Summary of the simulation results. The colored rows refer to the materials of the substrate and therefore to the Lima, colloidal Si-NCs, Air, Glycerol, and RIML configuration, respectively.  $n$  indicates the values of the refractive indices at 800 nm for all the configurations excepted for the colloidal Si-NCs scheme as specified in the footnote. % expresses the average radiated power with respect to the many simulations performed on the same configuration (at least 6). The errors are the standard deviations.

where *zone* stands for Top (blue curves), Lateral (red curves), and Bottom (green curves). The normal direction to the surface that contains all the detectors is called  $\mathbf{n}_{total}$ , while  $\mathbf{n}_{zone}$  is the normal with respect to a particular region, *i.e.* top, lateral, bottom respectively. Detectors are placed inside a circle centered in (0,0) and inscribed in the simulation plane. In this way, we considered the spherical symmetry of the emission. Their wave fronts propagate with different velocities through different materials. The oscillations of the normalized emitted power reflect this behavior. The black lines in the Fig.4.12 and Fig.4.13 are the time average radiated powers evaluated starting after the transient time.

As explained in the previous sections, an ensemble of dipole emitters can be considered as an incoherent light source. Each dipole is randomly distributed, it is independent of its neighbors (different emission frequencies), and it emits radiation with a random phase. At any given moment, the relative phases of all the dipoles are fixed. However, this relative phases change in a completely random fashion as a function of time. We performed many simulations of the same configuration to take into account the effect of the random parameters on the radiated power.

Fig.4.14 summarizes these results. We reported the refractive indices<sup>10</sup> of the different materials and the corresponding radiated power expressed in percentages. The radiated power is emitted towards the region with the largest refractive index, in all analyzed cases. Moreover, as shown in subsection 2.3.3, photoluminescence (PL) measurements, performed on different IBC devices with Si-QDs as active layer, showed different emissions. In order to explain these results, we applied this modelling to the structure of the G2B solar device characterized by silicon nitride as anti reflection coating. Also in this case, the emission is more directed towards the silicon substrate<sup>11</sup>. However, more light ( $\sim 4\%$ ) is emitted towards the top of the simulation plane with respect to the G2A configuration, as expected from the results reported in Fig.2.27.

The results of the simulations, reported in Fig.4.14, reflect the enhancement of the short circuit current density ( $J_{sc}$ ) measured in Chapter 2 and 3: in the RIML, lima, and colloidal Si-NCs configurations, approximately 60% of the emitted light is directed towards the silicon substrate explaining the reason why we detected  $J_{sc}$  enhancement only in these configurations. This behavior can be explained using Purcell's effect. The modification of the LDOS, characterized by interference phenomena between the emitted and reflected light, produces a large number of available electromagnetic modes in which photons can be emitted in the material with the higher refractive index. Therefore, the profile of the refractive indices needs to be tuned to get an efficiency enhancement. In this way, the photoluminescence emission of the Si-NCs results highly directed towards the silicon cell, reducing the loss mechanism hinted in subsection 1.4.2

## 4.5 Conclusions

In this chapter, a simulation method based on the modification of the local density of optical states (LDOS) is proposed to explain the experimental results obtained in Chapter 3.

In order to simulate the incoherent emission produced by silicon nanoparticles, we considered an array of electric oscillating dipoles randomly located and that

---

<sup>10</sup>@ 800 nm for the configurations characterized by Si-NCs deposited on quartz and @ 630 nm for the colloidal Si-NCs configuration.

<sup>11</sup>Top=  $(43 \pm 0.24)\%$ ; Lateral=  $(1 \pm 0.1)\%$ ;Bottom=  $(56 \pm 0.25)\%$ .

emit within a frequency range with different random phases. This approach was applied at different multilayered structures to simulate the “behavior” of the Si-NCs emission in the different systems considered in Chapters 2 and 3. The aim of these analysis was to evaluate the fraction of the emitted light effectively directed towards the silicon substrate in these different configurations. The simulation results reflect the enhancement of the short circuit current density measured in the previous chapters: approximately 60% of the emitted light is directed towards the silicon solar cells only in the lima, colloidal Si-NCs, and RIML configurations due to the LDOS modification produced by interference effect between the emitted and reflected light.

---

# Conclusions and future perspectives

In this thesis, the luminescent downshifting effect (LDS), a phenomenon produced by light-matter interaction at the nanometer scale, has been investigated for photovoltaic applications. The aim of my research activity, developed within the european project LIMA, was the modeling of a novel photovoltaic device to improve the performances of conventional silicon solar cells. In this sense my work, exploring interesting fundamental physic effects, could be interpreted as “a piece of a puzzle” in the realization of this project’s goal.

In this thesis, I have shown our efforts to fabricate an interdigitated back contact (IBC) silicon solar cell characterized by silicon quantum dots (Si-QDs) as active material. The use of a double layer stack, formed by silicon dioxide and Si-QDs, has been optimized by means of transfer matrix based simulations, to find the best tradeoff between its passive and its active optical properties. An additional optimization on the IBC fabrication process has been performed, by our partners at ISC center, to overcome the degradation of the cell properties due to the high annealing step necessary for the nanoparticles formation. Thanks to both these optimizations, IBC solar cells including Si-QDs were successfully produced. The resulting devices have shown good performance with respect to an optimized IBC reference solar cells coated with only silicon nitride: an enhancement of 2.5% in the averaged short circuit current density ( $J_{sc}$ ) is observed. Moreover, a best cell efficiency of 18.8% was achieved. This value is 4.44%, or 0.8% absolute, higher than the best reference cell fabricated in the LIMA project. A critical analysis of the observed results reveals that the UV-enhancement of the internal quantum efficiency, which causes the increase of the current, can be attributed to a combination of the LDS effect and an improved surface passivation. Although these two effects cannot be easily separated

by integrating Si-QDs during the cell fabrication process, they are both part of the positive contribution in the use of this novel layer and of its successful integration into IBC cells.

On the other hand, an alternative method is also proposed to separate the LDS effect by the improved surface passivation. We adopted the strategy to integrate LDS samples after the fabrication of IBC solar devices. In this way, the same solar cell is used both as a reference and as an active configuration. A silicon rich oxide layer is deposited on a 500  $\mu\text{m}$  quartz substrate and not directly on IBC solar cells. Then, this active layer is used as cell cover glass. Different configurations are studied changing the liquid between the cover/IBC spacing layer to activate the properties of the cover. These experiments revealed a  $J_{sc}$  enhancement of 1.22% and of 1.55% using a textured and a flat IBC solar cell respectively. These results are obtained pouring a refractive index liquid matching,  $n \sim 1.74$ , in the cover/IBC spacing layer. Moreover, also a  $J_{sc}$  improvement of 2.3% is measured using colloidal silicon nanocrystals dispersed in a glycerol solution as active liquid. A modification of the local optical density of states explains the obtained results: a large number of available electromagnetic modes, in which photons can be emitted, are produced in the material with the higher refractive index. By simulating the Si-QDs emission through an ensemble of oscillating electric dipoles, we estimated the fraction of the emitted light in the different configurations studied. Approximately, 60% of the emission is directed towards the silicon solar cell only in those configurations where we detected the  $J_{sc}$  improvements. All these analysis demonstrate the positive role of Si-NCs as downshifting material.

The results obtained during my Phd reveal a deep connection with applications, that could represent real innovations for technology advancements. In other words, it is based on the investigation of fundamental physic concepts applied to the “real world”. This research line, if further analyzed, can allow a full understanding and exploitation of the properties of silicon nanoparticles for photovoltaic applications.

---

# Bibliography

- [1] Teske and Bitter. Solar Generation V-Solar electricity for over one billion people and two million jobs by 2020. <http://www.epia.org/S>.
- [2] <http://www.nrel.gov>.
- [3] <http://www.limaproject.eu>.
- [4] <http://hyperphysics.phy-astr.gsu.edu/hbase/tables/elabund.html>.
- [5] H Takagi, H Ogawa, Y Yamazaki, A Ishizaki, and T Nakagiri. Quantum size effects on photoluminescence in ultrafine Si particles. *Applied Physics Letters*, 56(24):2379, 1990.
- [6] L. Canham. Silicon quantum wire array fabrication by electrochemical and chemical dissolution of wafers. *Applied Physics Letters*, 57(1046), 1990.
- [7] PDJ Calcott, KJ Nash, LT Canham, MJ Kane, and D Brumhead. Identification of radiative transitions in highly porous silicon. *Journal of Physics: Condensed Matter*, 5(7):L91, 1999.
- [8] PDJ Calcott, KJ Nash, LT Canham, MJ Kane, and D Brumhead. Spectroscopic identification of the luminescence mechanism of highly porous silicon. *Journal of luminescence*, 57(1):257–269, 1993.
- [9] Martin A. Green, Keith Emery, Yoshihiro Hishikawa, Wilhelm Warta, and Ewan D. Dunlop. Solar cell efficiency tables (version 40). *Progress in Photovoltaics: Research and Applications*, 20(5):606–614, 2012.
- [10] William Shockley and Hans J. Queisser. Detailed Balance Limit of Efficiency of p-n Junction Solar Cells. *Journal of Applied Physics*, 32(3):510–519, March 1961.

- 
- [11] A. Luque A. Marti. *Next Generation Photovoltaics: High efficiency through full spectrum utilization*. IOP Publishing, London, 2004.
- [12] A. J. Nozik. Spectroscopy and hot electron relaxation dynamics in semiconductor quantum wells and quantum dots. *Annual review of physical chemistry*, 52(1):193–231, 2001.
- [13] William A. Tisdale, Kenrick J. Williams, Brooke A. Timp, David J. Norris, Eray S. Aydil, and X. Y. Zhu. Hot-Electron Transfer from Semiconductor Nanocrystals. *Science*, 328(5985):1543–1547, June 2010.
- [14] M C Beard and R J Ellingson. Multiple exciton generation in semiconductor nanocrystals: Toward efficient solar energy conversion. *Laser Photonics Review*, 2(5):377–399, 2008.
- [15] Gavin Conibeer. Third-generation photovoltaics. *Materials Today*, 10(11):42–50, 2007.
- [16] R T Ross and A J Nozik. Efficiency of hot-carrier solar energy converters. *Journal of Applied Physics*, 53(5):3813, 1982.
- [17] A J Nozik. Quantum Dot Solar Cells. *Physica E: Low-dimensional Systems and Nanostructures*, 14(1-2):115–120, 2002.
- [18] A J Nozik, M C Beard, J M Luther, M Law, R J Ellingson, and J C Johnson. Semiconductor quantum dots and quantum dot arrays and applications of multiple exciton generation to third-generation photovoltaic solar cells. *Chemical Reviews*, 110(11):6873–6890, 2010.
- [19] Arthur J Nozik. Nanoscience and Nanostructures for Photovoltaics and Solar Fuels. *Nano Letters*, 10(8):100702082155032, 2010.
- [20] Peter T. Landsberg. *Recombination in Semiconductors*. Cambridge University Press, London, 2004.
- [21] Martin A Green. *Third Generation Photovoltaics: Advanced Solar Energy Conversion*, volume 10. Springer, 2006.

- [22] L. V. De Broglie. *Recherche sur la Theorie des Quanta (Research on the Quantum Theory)*. PhD thesis, Doctoral thesis, Univ. of Paris. Paris: Masson & Cie, 1924.
- [23] A. D. Yoffe. Semiconductor quantum dots and related systems: Electronic, optical, luminescence and related properties of low dimensional systems. *Advances in Physics*, 50:1–208, 2001.
- [24] L E Brus. Electronelectron and electron-hole interactions in small semiconductor crystallites: The size dependence of the lowest excited electronic state. *The Journal of Chemical Physics*, 80(9):4403, 1984.
- [25] L. Pavesi and T. Rasit, editors. *Silicon Nanocrystals: Fundamentals, Synthesis and Applications*. Oxford University Press, Inc. and The American Chemical Society, Berlin, 2010.
- [26] E C Cho, P Reece, M A Green, R Corkish, and M Gal. Optical transitions from SiO<sub>2</sub>/crystalline Si/SiO<sub>2</sub> quantum wells, 2002.
- [27] Thipwan Fangsuwannarak. *Electronic and optical characterisations of silicon quantum dots and its applications in solar cells*. PhD thesis, ARC Centre of Excellence for Advanced Silicon Photovoltaics and Photonics University of New South Wales Sydney, Australia, 2007.
- [28] Y Kanemitsu. Light-emitting silicon materials. *Journal of Luminescence*, 70(1-6):333–342, 1996.
- [29] Shinji Takeoka, Minoru Fujii, and Shinji Hayashi. Size-dependent photoluminescence from surface-oxidized Si nanocrystals in a weak confinement regime. *Phys. Rev. B*, 62:16820–16825, Dec 2000.
- [30] Tae-Wook Kim, Chang-Hee Cho, Baek-Hyun Kim, and Seong-Ju Park. Quantum confinement effect in crystalline silicon quantum dots in silicon nitride grown using SiH<sub>4</sub> and NH<sub>3</sub>. *Applied Physics Letters*, 88(12):123102, 2006.
- [31] Tae-Youb Kim, Nae-Man Park, Kyung-Hyun Kim, Gun Yong Sung, Young-Woo Ok, Tae-Yeon Seong, and Cheol-Jong Choi. Quantum confinement effect

- of silicon nanocrystals in situ grown in silicon nitride films. *Applied Physics Letters*, 85(22):5355, 2004.
- [32] U. Bockelmann and G. Bastard. Phonon scattering and energy relaxation in two-, one-, and zero-dimensional electron gases. *Phys. Rev. B*, 42:8947–8951, Nov 1990.
- [33] H. Benisty, C. M. Sotomayor-Torrès, and C. Weisbuch. Intrinsic mechanism for the poor luminescence properties of quantum-box systems. *Phys. Rev. B*, 44:10945–10948, Nov 1991.
- [34] U. Bockelmann. Exciton relaxation and radiative recombination in semiconductor quantum dots. *Phys. Rev. B*, 48:17637–17640, Dec 1993.
- [35] H. Benisty. Reduced electron-phonon relaxation rates in quantum-box systems: Theoretical analysis. *Phys. Rev. B*, 51:13281–13293, May 1995.
- [36] Xin-Qi Li, Hajime Nakayama, and Yasuhiko Arakawa. Phonon bottleneck in quantum dots: Role of lifetime of the confined optical phonons. *Phys. Rev. B*, 59:5069–5073, Feb 1999.
- [37] P. Lugli and S. M. Goodnick. Nonequilibrium longitudinal-optical phonon effects in GaAs-AlGaAs quantum wells. *Phys. Rev. Lett.*, 59:716–719, Aug 1987.
- [38] V. B. Campos, S. Das Sarma, and M. A. Stroschio. Phonon-confinement effect on electron energy loss in one-dimensional quantum wires. *Phys. Rev. B*, 46:3849–3853, Aug 1992.
- [39] R. P. Joshi and D. K. Ferry. Hot-phonon effects and interband relaxation processes in photoexcited GaAs quantum wells. *Phys. Rev. B*, 39:1180–1187, Jan 1989.
- [40] Marco Govoni, Ivan Marri, and Stefano Ossicini. Carrier multiplication between interacting nanocrystals for fostering silicon-based photovoltaics. *Nature photonics*, 6:672–679, 2012.
- [41] D Timmerman, J Valenta, K Dohnalov, W D A M De Boer, and T Gregorkiewicz. Step-like enhancement of luminescence quantum yield of silicon nanocrystals. *Nature Nanotechnology*, 6(October):1–4, 2011.

- [42] William A Tisdale, Kenrick J Williams, Brooke A Timp, David J Norris, Eray S Aydil, and X-Y Zhu. Hot-electron transfer from semiconductor nanocrystals. *Science*, 328(5985):1543–1547, 2010.
- [43] Randy J Ellingson, Matthew C Beard, Justin C Johnson, Pingrong Yu, Olga I Micic, Arthur J Nozik, Andrew Shabaev, and Alexander L Efros. Highly efficient multiple exciton generation in colloidal PbSe and PbS quantum dots. *Nano Letters*, 5(5):865–871, 2005.
- [44] Svetlana V Kilina, Dmitri S Kilin, and Oleg V Prezhdo. Breaking the phonon bottleneck in PbSe and CdSe quantum dots: time-domain density functional theory of charge carrier relaxation. *ACS nano*, 3(1):93–99, 2009.
- [45] Ryan Cooney, Samuel Sewall, Kevin Anderson, Eva Dias, and Patanjali Kambhampati. Breaking the Phonon Bottleneck for Holes in Semiconductor Quantum Dots. *Physical Review Letters*, 98(17):1–4, 2007.
- [46] M Nirmal, B O Dabbousi, M G Bawendi, J J Macklin, J K Trautman, T D Harris, and L E Brus. Fluorescence intermittency in single cadmium selenide nanocrystals. *Nature*, 383(6603):802–804, 1996.
- [47] Al. L. Efros and M. Rosen. Random Telegraph Signal in the Photoluminescence Intensity of a Single Quantum Dot. *Phys. Rev. Lett.*, 78:1110–1113, Feb 1997.
- [48] R. D. Schaller and V. I. Klimov. High Efficiency Carrier Multiplication in PbSe Nanocrystals: Implications for Solar Energy Conversion. *Phys. Rev. Lett.*, 92:186601, May 2004.
- [49] James E Murphy, Matthew C Beard, Andrew G Norman, S Phillip Ahrenkiel, Justin C Johnson, Olga I Ellingson Randy J Yu, Pingrong, and Arthur J Nozik. PbTe colloidal nanocrystals: synthesis, characterization, and multiple exciton generation. *Journal of the American Chemical Society*, 128(10):3241–3247, 2006.
- [50] J J H Pijpers, E Hendry, M T W Milder, R Fanciulli, J Savolainen, J L Herek, D Vanmaekelbergh, S Ruhman, D Mocatta, D Oron, and et al. Carrier

- Multiplication and Its Reduction by Photodoping in Colloidal InAs Quantum Dots. *Journal of Physical Chemistry B*, 111(11):4146–4152, 2007.
- [51] Yoichi Kobayashi, Takeshi Udagawa, and Naoto Tamai. Carrier Multiplication in CdTe Quantum Dots by Single-photon Timing Spectroscopy. *Chemistry Letters*, 38(8):830–831, 2009.
- [52] L. Mangolini, E. Thimsen, and U. Kortshagen. High-Yield Plasma Synthesis of Luminescent Silicon Nanocrystals. *Nano Letters*, 5(4):655–659, 2005.
- [53] Matthew C. Beard, Kelly P. Knutsen, Pingrong Yu, Joseph M. Luther, Qing Song, Wyatt K. Metzger, Randy J. Ellingson, and Arthur J. Nozik. Multiple Exciton Generation in Colloidal Silicon Nanocrystals. *Nano Letters*, 7(8):2506–2512, 2007.
- [54] M Wolf, R Brendel, J H Werner, and H J Queisser. Solar cell efficiency and carrier multiplication in Si<sub>1-x</sub>Ge<sub>x</sub> alloys. *Journal of Applied Physics*, 83(8):4213–4221, 1998.
- [55] D Timmerman, I Izeddin, P Stallinga, I N Yassievich, and T Gregorkiewicz. Space-separated quantum cutting with silicon nanocrystals for photovoltaic applications. *Nature Photonics*, 2(2):105–109, 2008.
- [56] R. Podila R. Singh N. Gupta, G. F. Alapatt and K. F. Poole. Prospects of Nanostructure-Based Solar Cells for Manufacturing Future Generations of Photovoltaic Modules. *International Journal of Photoenergy*, 2009(3), 2009.
- [57] J. B. Sambur, T. Novet, and B. A. Parkinson. Multiple Exciton Collection in a Sensitized Photovoltaic System. *Science*, 330:63–66, 2010.
- [58] B S Richards. Luminescent layers for enhanced silicon solar cell performance: Down-conversion. *Solar Energy Materials and Solar Cells*, 90(9):1189–1207, 2006.
- [59] Antonio Luque and Antonio Martí. Increasing the Efficiency of Ideal Solar Cells by Photon Induced Transitions at Intermediate Levels. *Phys. Rev. Lett.*, 78:5014–5017, Jun 1997.
- [60] ATLAS Users Manual. Silvaco International. *Santa Clara, CA*, 95054, 1995.

- [61] D L Dexter. A Theory of Sensitized Luminescence in Solids. *The Journal of Chemical Physics*, 21(5):836, 1953.
- [62] D Dexter. Possibility of Luminescent Quantum Yields Greater than Unity. *Physical Review*, 108(3):630–633, 1957.
- [63] W W Piper, J A DeLuca, and F S Ham. Cascade fluorescent decay in Pr<sup>3+</sup>-doped fluorides: Achievement of a quantum yield greater than unity for emission of visible light. *Journal of Luminescence*, 8(4):344–348, 1974.
- [64] J L Sommerdijk, A Bril, and A W De Jager. Two photon luminescence with ultraviolet excitation of trivalent praseodymium. *Journal of Luminescence*, 8(4):341–343, 1974.
- [65] T Trupke, M A Green, and P Wurfel. Improving solar cell efficiencies by down-conversion of high-energy photons. *Journal of Applied Physics*, 92(3):1668, 2002.
- [66] J Carrillo-López, JA Luna-López, I Vivaldo-De la Cruz, M Aceves-Mijares, A Morales-Sánchez, and G García-Salgado. UV enhancement of silicon solar cells using thin SRO films. *Solar Energy Materials and Solar Cells*, 100:39–42, 2012.
- [67] Hai-Qiao Wang, Mirosław Batentschuk, Andres Osvet, Luigi Pinna, and Christoph J Brabec. Rare-earth ion doped up-conversion materials for photovoltaic applications. *Advanced materials Deerfield Beach Fla*, 23(22-23):2675–2680, 2011.
- [68] Viorel Badescu and Alina Mihaela Badescu. Improved model for solar cells with up-conversion of low-energy photons. *Renewable Energy*, 34(6):1538–1544, 2009.
- [69] T Trupke, M A Green, and P Wurfel. Improving solar cell efficiencies by up-conversion of sub-band-gap light. *Journal of Applied Physics*, 92(7):4117, 2002.
- [70] D. Verma, T.O. Saetre, and O. Midtgaard. Review on up/down conversion materials for solar cell application. In *Photovoltaic Specialists Conference (PVSC), 2012 38th IEEE*, pages 002608 –002613, june 2012.

- [71] A. Meijerink W.G.J.H.M. van Sark and R.E.I. Schropp. Solar Spectrum Conversion for Photovoltaics Using Nanoparticles. *International Journal of Photoenergy*, 2012(3), 2012.
- [72] H J Hovel, R T Hodgson, and J M Woodall. The effect of fluorescent wavelength shifting on solar cell spectral response. *Solar Energy Materials*, 2(1):19–29, 1979.
- [73] W G J H M Van Sark. Enhancement of solar cell performance by employing planar spectral converters. *Applied Physics Letters*, 87(15):151117, 2005.
- [74] Lorenzo Pavesi and David J Lockwood. *Silicon photonics*, volume 1. Springer, 2004.
- [75] C. Canali, C. Jacoboni, F. Nava, G. Ottaviani, and A. Alberigi-Quaranta. Electron drift velocity in silicon. *Phys. Rev. B*, 12:2265–2284, Sep 1975.
- [76] D. Kovalev, H. Heckler, M. Ben-Chorin, G. Polisski, M. Schwartzkopff, and F. Koch. Breakdown of the  $k$ -Conservation Rule in Si Nanocrystals. *Phys. Rev. Lett.*, 81:2803–2806, Sep 1998.
- [77] Georg Pucker, Enrico Serra, and Yoann Jestin. Silicon Quantum Dots for Photovoltaics: A Review. *Quantum Dots- A variety of New Applications*.
- [78] Pavesi Lorenzo, Dal Negro L., C. Mazzoleni, G. Franzo, and F. Priolo. Optical gain in silicon nanocrystals. *Nature*, 408(6811):440–444.
- [79] D Kovalev, H Heckler, G Polisski, and F Koch. Optical properties of Si nanocrystals. *physica status solidi (b)*, 215(2):871–932, 1999.
- [80] Leonid Khriachtchev, Markku Rasanen, Sergei Novikov, Olli Kilpela, and Juha Sinkkonen. Raman scattering from very thin Si layers of Si/SiO<sub>2</sub> superlattices: Experimental evidence of structural modification in the 0.8–3.5 nm thickness region. *Journal of applied physics*, 86(10):5601–5608, 1999.
- [81] M. V. Wolkin, J. Jorne, P. M. Fauchet, G. Allan, and C. Delerue. Electronic States and Luminescence in Porous Silicon Quantum Dots: The Role of Oxygen. *Phys. Rev. Lett.*, 82:197–200, Jan 1999.

- [82] AB Filonov, Stefano Ossicini, F Bassani, and F Arnaud d'Avitaya. Effect of oxygen on the optical properties of small silicon pyramidal clusters. *Physical Review B*, 65(19):195317, 2002.
- [83] S. Godefroo, M. Hayne, M. Jivanescu, A. Stesmans, M. Zacharias, O. I. Lebedev, G. Van Tendeloo, and V. V. Moshchalkov. Classification and control of the origin of photoluminescence from Si nanocrystals. *Nat Nano*, 3:174–178, 2008.
- [84] R. J. Walters, J. Kalkman, A. Polman, H. A. Atwater, and M. J. A. de Dood. Photoluminescence quantum efficiency of dense silicon nanocrystal ensembles in SiO<sub>2</sub>. *Phys. Rev. B*, 73:132302, Apr 2006.
- [85] VA Belyakov, VA Burdov, R Lockwood, and A Meldrum. Silicon nanocrystals: fundamental theory and implications for stimulated emission. *Advances in Optical Technologies*, 2008, 2008.
- [86] Zhizhong Yuan, Georg Pucker, Alessandro Marconi, Fabrizio Sgrignuoli, Aleksei Anopchenko, Yoann Jestin, Lorenza Ferrario, Pierluigi Bellutti, and Lorenzo Pavesi. Silicon nanocrystals as a photoluminescence down shifter for solar cells. *Solar Energy Materials and Solar Cells*, 95(4):1224–1227, 2011.
- [87] F. Sgrignuoli, G. Paternoster, P. Marconi A. and, Ingenhoven, A. Anopchenko, G. Pucker, and L. Pavesi. Modeling of silicon nanocrystals based down-shifter for enhanced silicon solar cell performance. *J. Appl. Phys.*, 111:034303–034310, 2012.
- [88] S Prezioso, A Anopchenko, Z Gaburro, L Pavesi, G Pucker, L Vanzetti, and P Bellutti. Electrical conduction and electroluminescence in nanocrystalline silicon-based light emitting devices. *Journal of applied physics*, 104(6):063103–063103, 2008.
- [89] Domenico Pacifici. *Erbium doped silicon nanoclusters for microphotonics*. PhD thesis, Citeseer, 2003.
- [90] H Angus Macleod. *Thin film optical filters*. Taylor & Francis, 2001.
- [91] Michael Bass and Virendra N Mahajan. *Handbook of optics*, volume 2. McGraw-Hill, 2001.

- 
- [92] M Born and E Wolf. *Principles of Optics*. Cambridge University Press, 7 edition, 1999.
- [93] Lev Davidovich Landau, Evgenij Mihajlovič Lifšic, John Bradbury Sykes, John Stewart Bell, MJ Kearsley, and Lev Petrovich Pitaevskii. *Electrodynamics of continuous media*, volume 364. Pergamon press Oxford, 1960.
- [94] E. Klampaftis, D. Ross, K. R. McIntosh, and B. S. Richards. Enhancing the performance of solar cells via luminescent down-shifting of the incident spectrum: A review. *Sol. Energy Mater. Sol. Cells*, 93:1182–1194, 2009.
- [95] C. Strumpel, M. McCann, G. Beaucarne, V. Arkhipov, A. Slaoui, V. Svrcek, C. del Canizo, and Tobias I. Modifying the solar spectrum to enhance silicon solar cell efficiency-an overview of available materials. *Sol. Energy Mater. Sol. Cells*, 91:238–249, 2007.
- [96] Antonio Luque and Steven Hegedus. *Photovoltaic Science and Engineering*. Wiley Online Library, 2003.
- [97] Stuart R Wenham. *Applied photovoltaics*. Earthscan/James & James, 2007.
- [98] WL Barnes. Fluorescence near interfaces: the role of photonic mode density. *journal of modern optics*, 45(4):661–699, 1998.
- [99] E Snoeks, A Lagendijk, and A Polman. Measuring and modifying the spontaneous emission rate of erbium near an interface. *Physical review letters*, 74(13):2459–2462, 1995.
- [100] M. J. A. de Dood, L. H. Slooff, A. Polman, A. Moroz, and A. van Blaaderen. Local optical density of states in SiO<sub>2</sub> spherical microcavities: Theory and experiment. *Phys. Rev. A*, 64:033807, Aug 2001.
- [101] HP Urbach and GLJA Rikken. Spontaneous emission from a dielectric slab. *Physical Review A*, 57(5):3913, 1998.
- [102] BC Buchler, T Kalkbrenner, C Hettich, and V Sandoghdar. Measuring the quantum efficiency of the optical emission of single radiating dipoles using a scanning mirror. *Physical review letters*, 95(6):63003, 2005.

- [103] GG Ross, D Barba, C Dahmoune, YQ Wang, and F Martin. Effect of implanted Si concentration on the Si nanocrystal size and emitted PL spectrum. *Nuclear Instruments and Methods in Physics Research Section B: Beam Interactions with Materials and Atoms*, 256(1):211–215, 2007.
- [104] SM Orbons, MG Spooner, and RG Elliman. Effect of material structure on photoluminescence spectra from silicon nanocrystals. *Journal of applied physics*, 96(8):4650–4652, 2004.
- [105] RS Anderssen, Saiful A Husain, and RJ Loy. The Kohlrausch function: properties and applications. *Anziam Journal*, 45:C800–C816, 2004.
- [106] Robert Joseph Walters. *Silicon nanocrystals for silicon photonics*. PhD thesis, California Institute of Technology, 2007.
- [107] J Kalkman, H Gersen, L Kuipers, and A Polman. Excitation of surface plasmons at a SiO<sub>2</sub>/Ag interface by silicon quantum dots: Experiment and theory. *Physical Review B*, 73(7):075317, 2006.
- [108] W.Theiss. Scout: Optical spectrum simulator.
- [109] M Zanucoli, PF Bresciani, M Frei, H-W Guo, H Fang, M Agrawal, C Fiegna, and E Sangiorgi. 2-D numerical simulation and modeling of monocrystalline selective emitter solar cells. In *Photovoltaic Specialists Conference (PVSC), 2010 35th IEEE*, pages 002262–002265. IEEE, 2010.
- [110] Andres Cuevas and David A Russell. Co-optimisation of the emitter region and the metal grid of silicon solar cells. *Progress in Photovoltaics: Research and Applications*, 8(6):603–616, 2001.
- [111] Mohamed M Hilali, Ajeet Rohatgi, and Sally Asher. Development of screen-printed silicon solar cells with high fill factors on 100  $\Omega$ /sq emitters. *Electron Devices, IEEE Transactions on*, 51(6):948–955, 2004.
- [112] Yoann Jestin, Georg Pucker, Mher Ghulinyan, Lorenza Ferrario, Pierluigi Bellutti, Antonio Picciotto, Amos Collini, Alessandro Marconi, Aleksei Anopchenko, Zhizhong Yuan, et al. Silicon solar cells with nano-crystalline silicon down shifter: experiment and modeling. In *Proceedings of SPIE- The*

- International Society for Optical Engineering*, volume 7772. SPIE, P. O. BOX 10 Bellingham WA 98227-0010 USA, 2010.
- [113] W.G.J.H.M. v. Sark, A. Meijerink, R. Schropp, J. van Roosmalen, and E. Lyssen. Enhancing solar cell efficiency by using spectral converters. *Sol. Energy Mater. Sol. Cells*, 87:395–409, 2005.
- [114] Gerda C Glaeser and Uwe Rau. Improvement of photon collection in Cu (In, Ga) Se<sub>2</sub> solar cells and modules by fluorescent frequency conversion. *Thin solid films*, 515(15):5964–5967, 2007.
- [115] 27th European Photovoltaic Solar Energy Conference and Exhibition. *Screen Printed IBC Solar Cells with Silicon Quantum Dots Down-Shifted Layer*, Messe Frankfurt, Germany, 24-28 September 2012.
- [116] Shu-Man Liu, Yang, Seiichi Sato, and Keisaku Kimura. Enhanced Photoluminescence from Si Nano-organosols by Functionalization with Alkenes and Their Size Evolution. *Chemistry of Materials*, 18(3):637–642, 2006.
- [117] X. D. Pi, R. W. Liptak, J Deneen Nowak, N. P. Wells, C.B. Carter, S. A. Campbell, and U. Kortshagen. Air-stable full-visible-spectrum emission from silicon nanocrystals synthesized by an all-gas-phase plasma approach. *Nanotechnology*, 19(24):245603, 2008.
- [118] Jing Zou, Philip Sanelle, Katherine A. Pettigrew, and Susan M. Kauzlarich. Size and Spectroscopy of Silicon Nanoparticles Prepared via Reduction of SiCl<sub>4</sub>. *Journal of Cluster Science*, 17:565–578, 2006. 10.1007/s10876-006-0082-9.
- [119] G. Belomoin, J. Therrien, and M. Nayfeh. Oxide and hydrogen capped ultrasmall blue luminescent Si nanoparticles. *Applied Physics Letters*, 77:779, 2000.
- [120] X. Pi, Q. Li, D. Li, and D. Yang. Spin-coating silicon-quantum-dot ink to improve solar cell efficiency. *Solar Energy Materials and Solar Cells*, 95(10):2941 – 2945, 2011.

- [121] Xiaodong Pi, Li Zhang, and Deren Yang. Enhancing the Efficiency of Multicrystalline Silicon Solar Cells by the Inkjet Printing of Silicon-Quantum-Dot Ink. *The Journal of Physical Chemistry C*, 116(40):21240–21243, 2012.
- [122] L Vanzetti, G Pucker, S Milita, M Barozzi, M Ghulinyan, and M Bersani. Structural analyses of thermal annealed SRO/SiO<sub>2</sub> superlattices. *Surface and Interface Analysis*, 42(6-7):842–845, 2010.
- [123] Parameswaran Hariharan. *Basics of interferometry*. Academic Press, 2007.
- [124] url <http://www.cargille.com/index.shtml>.
- [125] N. Prtljaga, E. D’Amato, A. Pitanti, R. Guider, S. Froner, E. and Larcheri, M. Scarpa, and Pavesi L. Photoluminescence of hydrophilic silicon nanocrystals in aqueous solutions. *Nanotechnology*, 22:215704, 2011.
- [126] D. Kovalev, J. Diener, H. Heckler, G. Polisski, N. Künzner, and F. Koch. Optical absorption cross sections of Si nanocrystals. *Phys. Rev. B*, 61:4485–4487, Feb 2000.
- [127] N. Engheta, C. H. Papas, and C. Elachi. Radiation patterns of interfacial dipole antennas. *Radio Science*, 17:1557–1566, 1982.
- [128] L. Novotny and B. Hecht. *Principles of Nano-Optics*. Cambridge University Press, 2006.
- [129] John D. Jackson. *Classical Electrodynamics Third Edition*. Wiley, third edition, 1998.
- [130] Sommerfeld. *Partial Differentiation Equation in Physics*. Academic Press, New York and London, New York, 1949.
- [131] Enrico Fermi. Quantum theory of radiation. *Rev. Mod. Phys.*, 4:87–132, 1932.
- [132] R Loudon. *The Quantum Theory of Light; 3rd ed.* Oxford Univ. Press, Oxford, 2002.
- [133] Chen-To Tai. *Dyadic Green Functions in Electromagnetic Theory (Ieee-Oup Series on Electromagnetic Wave Theory)*. Oxford University Press, USA, 1996.

- 
- [134] E. M. Purcell. Spontaneous emission probabilities at radio frequencies. volume 69, page 681, 1946.
- [135] J. M. Gérard, B. Sermage, B. Gayral, B. Legrand, E. Costard, and V. Thierry-Mieg. Enhanced Spontaneous Emission by Quantum Boxes in a Monolithic Optical Microcavity. *Phys. Rev. Lett.*, 81:1110–1113, Aug 1998.
- [136] Daniel Kleppner. Inhibited Spontaneous Emission. *Phys. Rev. Lett.*, 47:233–236, Jul 1981.
- [137] A. Pitanti, M. Ghulinyan, D. Navarro-Urrios, G. Pucker, and L. Pavesi. Probing the Spontaneous Emission Dynamics in Si-Nanocrystals-Based Microdisk Resonators. *Phys. Rev. Lett.*, 104:103901, Mar 2010.
- [138] Peter Lohdahl, A. Floris Driel van, Ivan S. Nikolaev, Arie Irman, Karin Overgaag, Daniel Vanmaekelbergh, and Willem L. Vos. Controlling the dynamics of spontaneous emission from quantum dots by photonic crystals. *Nature*, 430(7000):654–657, May 2004.
- [139] Eli Yablonovitch. Inhibited Spontaneous Emission in Solid-State Physics and Electronics. *Phys. Rev. Lett.*, 58:2059–2062, May 1987.
- [140] J. N. Farahani, D. W. Pohl, H.-J. Eisler, and B. Hecht. Single Quantum Dot Coupled to a Scanning Optical Antenna: A Tunable Superemitter. *Phys. Rev. Lett.*, 95:017402, Jun 2005.
- [141] O. L. Muskens, V. Giannini, J. A. Sanchez-Gil, and J. Gomez Rivas. Strong Enhancement of the Radiative Decay Rate of Emitters by Single Plasmonic Nanoantennas. *Nano Letters*, 7(9):2871–2875, 2007.
- [142] T.H. Taminiau, F.D. Stefani, F.B. Segerink, and N.F. Hulst van. Optical antennas direct single-molecule emission. *Nature photonics*, 2:234–237, 2008.
- [143] K. H. Drexhage. Interaction of light with monomolecular dye layers. *Progress in Optics*, 12.
- [144] L’uboš Polerecky, Jaroslav Hamrle, and Brian D. MacCraith. Theory of the Radiation of Dipoles Placed Within a Multilayer System. *Appl. Opt.*, 39(22):3968–3977, Aug 2000.

- [145] M Grtzel. Photoelectrochemical cells. *Nature*, 414(6861):338–344, 2001.
- [146] Hong-Gyu Park, Se-Heon Kim, Soon-Hong Kwon, Young-Gu Ju, Jin-Kyu Yang, Jong-Hwa Baek, Sung-Bock Kim, and Yong-Hee Lee. Electrically Driven Single-Cell Photonic Crystal Laser. *Science*, 305(5689):1444–1447, September 2004.
- [147] Charles Santori, David Fattal, Jelena Vuckovic, Glenn S. Solomon, and Yoshihisa Yamamoto. Indistinguishable photons from a single-photon device. *Nature*, 419(6907):594–597, October 2002.
- [148] R. R. Chance, A. Prock, and R. Silbey. *Molecular Fluorescence and Energy Transfer Near Interfaces*, volume 37.
- [149] G. W. Ford and W. H. Weber. Electromagnetic interactions of molecules with metal surfaces. *Physics Reports*, 113(4):195–287, November 1984.
- [150] COMSOL Multiphysics.
- [151] Jacek Kossut. Quantum dots: Squeeze or stretch? *Nature materials*, 8(1):8–9, 2009.
- [152] S. A. Empedocles, D. J. Norris, and M. G. Bawendi. Photoluminescence Spectroscopy of Single CdSe Nanocrystallite Quantum Dots. *Phys. Rev. Lett.*, 77:3873–3876, Oct 1996.
- [153] M.S. Zubary M.O. Scully. *Quantum Optics*. Cambridge University Press, 2001.
- [154] Mads L. Andersen, Soren Stobbe, Anders S. Sorensen, and Peter Lodahl. Strongly modified plasmon-matter interaction with mesoscopic quantum emitters. *Nat Phys*, 7(3):215–218, March 2011.
- [155] Søren Stobbe, Jeppe Johansen, Andreas Löffler, Sven Höfling, Alfred Forchel, Jørn Märcher. Hvam, and Peter Lodahl. Breakdown of the Dipole Approximation for Large Quantum Dot Emitters Coupled to an Interface. In *Conference on Lasers and Electro-Optics/Quantum Electronics and Laser Science Conference and Photonic Applications Systems Technologies*, page QThD4. Optical Society of America, 2008.

- 
- [156] S. Stobbe, P. T. Kristensen, J. E. Mortensen, J. M. Hvam, J. Mørk, and P. Lodahl. Spontaneous emission from large quantum dots in nanostructures: Exciton-photon interaction beyond the dipole approximation. *Phys. Rev. B*, 86:085304, Aug 2012.
- [157] J P Reithmaier, G Sek, A Lffler, C Hofmann, S Kuhn, S Reitzenstein, L V Keldysh, V D Kulakovskii, T L Reinecke, and A Forchel. Strong coupling in a single quantum dot-semiconductor microcavity system. *Nature*, 432(7014):197–200, 2004.
- [158] S. Ossicini, L. Pavesi, and F. Priolo, editors. *The ACS Style Guide*. Light emitting Silicon for Microphotonics, Berlin, 2003.
- [159] Ilya Sychugov, Robert Juhasz, Jan Valenta, and Jan Linnros. Narrow Luminescence Linewidth of a Silicon Quantum Dot. *Phys. Rev. Lett.*, 94:087405, Mar 2005.
- [160] MATLAB. *version 7.10.0 (R2010a)*. The MathWorks Inc., Natick, Massachusetts, 2010.

---

# Acknowledgements

The Ph.D is/was an incredible period of personal growth, not only from a research point of view. At the end of this itinerary, you have a lot of debts towards many people who helped you to understand and to overtake the obstacles. Here, I want to reserve a place to thank all of these fantastic “ladies and gentlemen” that I had the fortune to meet.

My first thought goes to prof. Pavesi. Without his inestimable help, my transition, from “pure” theoretician to “applied” theoretician to conclude, my evolution, in a sort of experimentalist, would not have been possible. His experience has helped me a lot, and he absolutely deserves my first thank. My second “thanks” goes to prof. Soldati: my theoretical “*forma mentis*” was fundamental to deal with the problems found during these three years. I am grateful to everyone who directly or indirectly supported and contributed to the reaching of this goal. To **all** NL group members, current and past, for their help and friendship. In particular, Paolo who help me a lot in my computational problems regarding, mainly, the “electric code” (not presented in this thesis). “*Paolo grazie, e scusami...so che alcune volte sono un chiodo*“. I cannot forget Mattia (*the climber*) for its incredible intuition, as well as Federica who have shared this experience with me. *Zio Tenga, Ferraman*, thanks to you.

Many research groups and EC funding have to be properly addressed. I wish to thank FBK AP&P lab., ISC, NTC-UPVLC, CSIC, ISO, and ISO and all the members of the LIMA project.

Per i non addetti ai lavori, preferisco *to switch* all'italiano. Da dove iniziare se non dalla mia famiglia. A papà Arnaldo, mamma Flora e a mia sorella Nico dedico questa mia ultima tesi. Per non scendere troppo nel banale e nello sdolcinato (sapete che non è da me), penso che a volte la semplicità sia meglio di inutili parole buttate lì a caso. Quindi *grazie di tutto*.

Come non menzionare il gruppo di "Fossacesia" sempre in continua evoluzione ed espansione: nuovi arrivati (oltre a Super Samù adesso anche Fabiano arricchisce la super famiglia Berghella) ed unioni che **finalmente** stanno per essere coronate (Lorenzo-Antonella). Alcune cose cambiano, si evolvono, si trasformano ma non tutte...come l'immensa stima che nutro per voi e che so essere ricambiata in modo incondizionale. Ste, Loré siete molto più che migliori amici, siete fratelli...le mie scelte di vita mi hanno, e forse mi porteranno, sempre lontano dal piccolo paesino ma so che quello che c'è tra noi non si spezzerà e non cambierà mai.

Nella mia "terra" c'è anche un altro gruppo di persone spettacolari, sotto ogni punto di vista, che non posso non menzionare: la "combriccola" lancianese. Che dire di voi... ne abbiamo combinate di ogni colore, troppo da raccontare, troppo di cui ringraziare. La semplicità del ri-incontrarsi e capire che nulla è cambiato: pochi giorni, poche ore...sì...ma indimenticabili.

La mia seconda famiglia "bolognese", come non citarla. Elisa, Daddy, La Sté, Giorgino...la compagnia che non dimenticherò mai. Anche qui quante cose condivise di cui non cambierai mai neanche una virgola. Anche se ormai le nostre vite hanno preso direzioni diverse, vi sento sempre vicini. Grazie di cuore ragà.

Alla fine, solo per ordine cronologico, tutte le persone che ho avuto l'onore di conoscere in questi miei tre anni nell'impero *austro-ungarico*, come da noi amorevolmente ribattezzato. Da chi inizio? Solo per convenienza, dai (Giovanni)<sup>3</sup> o meglio conosciuti come la triade scarlatta. G.Paternoster, se i muri di casa nostra potessero parlare, quante ne racconterebbero?...e qui mi fermo. Sei stata la prima persona che ho conosciuto a Trento, per mia sfortuna, e le nostre serate dalla Lina rimarranno per sempre negli annali. Franzolo e G.Acqua cosa dire di voi due...amici per la vita: mi siete stati davvero vicini nei momenti più difficili di questi tre anni e, non solo per questo, vi ringrazio con questa citazione "*All along the watchtower, princes kept the view...*" che racchiude molto di più del suo significato letterario. Amedé come avrei fatto senza di te? L'allegria allo stato puro: sempre con il sorriso in volto, sempre pronto, sempre disponibile, sempre con la chitarra, o qualsiasi altro strumento mu-

sicale, in mano...un' altra persona di cui fidarsi ciecamente. Così come Giacomino. Il fiorentino d.o.c. che non scorderò mai per la sua spontaneità e sincerità. Pintorè come non posso citare pure tè. Una parola ti calza alla perfezione: mitico. Alla fine, con il significato di *dulcis in fundo*, la mitica ed insostituibile Pam. La mia migliore amica. Senza di te sarei sicuramnete ricoverato in quella *clinica da cui fuggivo la sera* per venire al Simposio: sei la migliore!

In questo mio lavoro c'è una piccola parte di ognuno di voi, **nessun escluso**.

